High Frequency Acoustic Wave Scattering From Turbulent Premixed Flames

A Dissertation

Presented to

The Academic Faculty

By

Venkateswarlu Narra

In Partial Fulfillment
of the Requirements for the Degree of
Doctor of Philosophy in
Aerospace Engineering

Georgia Institute of Technology
May 2008

High Frequency Acoustic Wave Scattering From Turbulent Premixed Flames

Approved By

Dr. Timothy C. Lieuwen, Advisor
Associate Professor
School of Aerospace Engineering
Georgia Institute of Technology

Dr. Jerry M. Seitzman
Associate Professor
School of Aerospace Engineering
Georgia Institute of Technology

Dr. Massimo Ruzzene
Associate Professor
School of Aerospace Engineering
Georgia Institute of Technology

Dr. Richard Gaeta
Senior Research Engineer
Georgia Tech Research Institute
Georgia Institute of Technology

Dr. Shivakumar Srinivasan
Advanced Technology Organization
Combustion Group
GE Gas Turbines

Date Approved: 12/12/2007

To my parents

Acknowledgements

I would like to thank my advisor, Dr. Tim Lieuwen for his guidance and support during this research.

I would also like to express my deep appreciation for Dr. Jerry Seitzman, Dr. Massimo Ruzzene, Dr. Richard Gaeta and Dr. Shiva Srinivasan for serving on my thesis and a great deal of advice and assistance.

I would like to thank my colleagues at Aerospace Combustion Lab: Suraj, Rajesh, Muruganandam, Ben, Antonio, Adam, Rob, Qingguo, Bobba, Santosh S, Nori, Preetham, Prakash, Bobby, Priya, Santosh H, Sai and Thao.

I would further like to thank Dr. Jeff Jagoda for his considerate attitude and support during my doctoral program.

I would also like to thank National Science Foundation for their interest and support in this research.

Table of Contents

List of Tables

List of Figures

Summary

This thesis describes an experimental investigation of high frequency acoustic wave scattering from turbulent premixed flames. The objective of this work was to characterize the scattered incoherent acoustic field and determine its parametric dependence on frequency, flame brush thickness, incident and measurement angles, mean velocity and flame speed.

The experimental facility consists of a slot burner with a flat flame sheet that is approximately 15 cm wide and 12 cm tall. The baseline cold flow characteristics and flame sheet statistics were extensively characterized.

Studies were performed over a wide range of frequencies (1-24 kHz) in order to characterize the role of the incident acoustic wave length. The spectrum of the scattered acoustic field showed distinct incoherent spectral sidebands on either side of the driving frequency. The scattered incoherent field was characterized in terms of the incoherent field strength and spectral bandwidth and related to the theoretical predictions.

The role of the flame front wrinkling scale, i.e., flame brush thickness, was also studied. Flame brush thickness was varied independent of the mean velocity and flame speed by using a variable turbulence generator. Results are reported for five flame brush thickness cases, ranging from 1.2 mm to 5.2 mm. Some dependence of scattered field characteristics on flame brush thickness was observed, but the magnitude of the effect was much smaller than expected from theoretical considerations.

The spatial dependence of the scattered field was investigated by measuring the scattered field at four measurement angles and exciting the flame at four incident angles.

Theory predicts that these variations influence the spatial scale of the acoustic wave normal to the flame, a result confirmed by the measurements.

Measurements were performed for multiple combinations of mean velocities and flame speeds. The scattered field was observed to depend strongly on the flame speed. Further analysis suggested that the change in orientation angle distribution with flame speed had a large influence on the scattered field. The scattered field characteristics did not show any appreciable change with mean velocity. This result was expected since flame brush thickness characteristics themselves exhibit a weak velocity dependence.

Chapter 1

Introduction

This thesis describes an experimental investigation of high frequency acoustic wave scattering from turbulent premixed flames. In this chapter, first, motivation for such a study is presented. Relevant subject background and literature review is presented in the second section. Then, an overview of the thesis is detailed in the third section.

1.1 Motivation

Recent regulations, such as The Clean Air Act in the US, have imposed stringent restrictions on emission and control of nitrogen oxides (NO_x) from stationary sources, such as industrial gas turbines. These regulations have driven the power generation industry towards lean premixed-combustion[1] in order to minimize combustion temperatures and, therefore, NO_x.

However, one of the problems of premixed operation is that the combustors are susceptible to instabilities. Combustion instabilities occur when the unsteady heat release process couples with acoustics modes of the combustor (Rayleigh criterion[2]). In such cases, these self-excited oscillations produce large amplitude acoustic oscillations that are destructive to hardware life and performance. A land based gas turbine combustion chamber liner damaged by such combustion instabilities is shown in Figure 1.

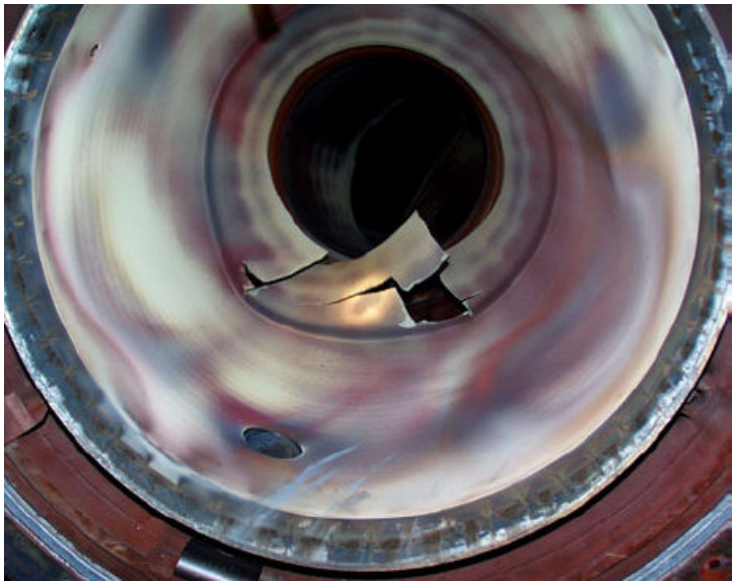

Figure 1. A damaged combustor liner due to combustion instabilities.[3]

Coupling of heat release oscillations with longitudinal oscillations lead to instabilities at low frequencies, typically at tens or low hundreds of Hz. However, if the heat release oscillations couple with transverse acoustic modes, then the instabilities occur at high frequencies, typically at thousands of Hz. These instabilities are sometimes referred to as "screech".

Because of the high frequency nature of the screech, they are unacceptable during combustor operation. For example, compared to pressure oscillations at 100 Hz, a screech instability at 2500 Hz will drastically reduce the life of the hardware, because of the 25 times higher loading and unloading events per second on the hardware. For this reason, the allowed amplitude for such screech frequencies is typically few tenths of a psi as opposed to a few psi for the low frequency oscillations.[3]

To prevent such combustion instabilities, it is essential to understand the flame acoustic wave interactions, such as the driving and the damping processes involved. Flame acoustic wave interactions has been the focus of many detailed studies.[4-9]

This thesis is particularly motivated by recent analyses reported by Lieuwen[10] regarding the nature of high frequency acoustic wave interactions with turbulent premixed flames. His analysis suggested that the flame front movement of the turbulent flame could act as a source of damping in flame acoustic wave interactions. It was suggested that, because of the flame front movement, the energy of incident acoustic wave is transferred into frequencies that are different from that of the incident wave and thus acts as an energy damping mechanism at the incident acoustic wave frequency. The above mentioned analysis predicts that this mechanism is particularly important at high frequencies.

This thesis is aimed at experimentally understanding such high frequency acoustic wave and flame interactions.

1.2 Background and Literature Review

The basic problem of acoustic wave interactions with a turbulent premixed flame is depicted in Figure 2. Upon reaching the flame front, the waves are scattered and potentially amplified because of the significant change in sound speed and density at the flame front, the response of the flame front position and mass burning rate due to the perturbations and interactions with intrinsic flame and flow instabilities.[11] Flame and acoustic wave interactions have been the focus of many theoretical and experimental studies. These studies are briefly described here.

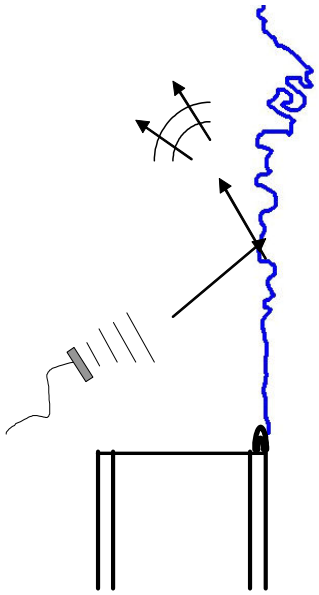

Figure 2. Schematic of acoustic wave scattering problem.

1.2.1 Laminar Flame - Acoustic Wave Interactions

The first theoretical treatment of acoustic wave-flame interactions was performed by Chu[12], who regarded the flame front as a temperature discontinuity (infinitely thin flame) that separates the unburned reactants from the burned products. He considered the case where an acoustic wave is normally incident upon an infinitely long planar flame. He derived expressions for boundary conditions needed to be satisfied at the flame front. The study showed that any changes in flame speed, heat of reaction of the reactive mixture, entropy of the incoming mixture or specific heats ratio resulted in the generation or amplification of the acoustic waves.

Markstein[13] analyzed the effect of unsteady small perturbations upon a steady state laminar flame. He considered a parametric equation for the description of the flame front. From this, he derived kinematic equations that relate the flame front position to the

local flow and flame burning velocities. The mass, momentum and energy conservation equations couple the flow and thermodynamic variables upstream and downstream of the flame front.

These works have been extended in several recent analysis, e.g., McIntosh and co-workers[14,15], Peters and Ludford[16], Van Harten et al.[17], Ledder and Kapila[18], which included the effects of pressure perturbations on the flame structure. They analyzed the flame front structure perturbed by an acoustic wave using high energy asymptotics and single step kinetics. These studies quantified the response of the flame's burning velocity to the unsteady pressure and temperature variations in the incident acoustic wave. These studies emphasized the role of length and time scales of the acoustic wave and flame preheat and reaction zones in these interactions.

The coupling effects between acoustic wave and burning rate fluctuations have been reported by Lieuwen[19], Clavin *et al*.[20], Poinsot and Candel[21] and others. In the study performed by Lieuwen[19], he considered the case where an acoustic wave is incident upon the flame front at an oblique angle. He calculated the net acoustic energy out of the flame front and from this he calculated the damping or amplification of the acoustic field. Results suggested that energy is added to the acoustic field by the unsteady flux of the unburned reactants while acoustic energy is dissipated by the production of vorticity fluctuations that are generated at the flame front by baroclinic vorticity production mechanism.

The interactions between the inherent flame instabilities and acoustically induced flow oscillations have been discussed by Markstein[3], Searby and Rochwerger[22] and others. Experiments in a Taylor-Couette combustor by Vaezi and Aldredge[23] showed that

the flame develops cellular structures due to the Darrieus-Landau instability as it propagates down the tube. For lean mixtures, the study reports, the flame propagates down the tube with out generating sound. Measurements by Searby[24] suggested distinct stages of flame propagation: primary instability generated by the natural acoustic mode of the duct that modulates the cellular structure, followed by a re-stabilized flame front due to the stabilization of the Darrieus-Landau instability by the oscillatory acceleration imposed by the acoustic field. For flames with higher burning velocities, this primary instability is followed by a secondary instability leading to small, pulsating cellular structures which break down into highly distorted turbulent front at higher amplitudes. Searby and Rochwerger[22] have experimentally determined the threshold of parametric instability for different frequencies. Their results indicated that the acoustic amplitudes are comparable to that of the flame speed for such parametric instabilities. For example, the acoustic amplitude threshold for parametric instability, expressed as ratio of acoustic velocity to that of laminar flame speed, was found to be 7 at 500 Hz.

1.2.2 Turbulent Flame - Acoustic Wave Interactions

Recent studies have applied ideas based on the laminar flame to the problem of acoustic wave interactions with turbulent flames, e.g., Lieuwen and coworkers[10,25,11,26]. The problem addressed in Refs [10, 25, 11 and 26] is that of the scattering of high frequency acoustic waves from single-connected, wrinkled flame fronts by considering the flame as a dynamically evolving, corrugated temperature discontinuity. Results suggest that the characteristics of scattered acoustic waves from turbulent flames are qualitatively different from that of laminar flames. The key results of the study are listed below:

(i) Because of the random movement of the turbulent flame front, a coherent, harmonically oscillating acoustic wave, incident upon a turbulent flame generates both coherent, and incoherent scattered waves.

(ii) Because of the Doppler shift induced by the flame front movement, the frequency of the scattered wave need not be the same as the frequency of the incident wave. In essence, the energy in the coherent field is transferred into the incoherent field because of the flame front movement; i.e., flame front movement acts as an energy transform mechanism.

(iii) The phase of the scattered acoustic wave differs from point to point along the flame front because of differences in distance the wave travels before impinging on the flame front and reflecting.[27] Interference between out of phase waves leads to reduction in coherent power and increase in incoherent power. For a given scale of flame front wrinkling, characterized as flame brush thickness (σ), as the frequency (wavelength, λ) increases (decreases), the surface appears progressively rougher, leading to more and more of the power in the coherent field being transferred into the incoherent field. This coherent energy damping is particularly significant for disturbances whose wavelengths are smaller than the characteristic scales of flame wrinkling; i.e., $\sigma/\lambda > 1$. This process leads to saturation of the incoherent field power once all the available power in the coherent field is transferred to the incoherent field. Conversely, for a given frequency, increases in flame front wrinkling will have the same effect as increases in frequency at a fixed scale of flame front wrinkling. That is, coherent to incoherent field energy transfer is enhanced by the increased scale of flame front wrinkling.

(iv) The reflection coefficient of a nominal flat flame front*, R, when the acoustic wave is incident from the reactants side, is given by[28]:

$$R = \frac{\frac{\rho_p c_p}{\rho_r c_r}\cos\theta_i - \sqrt{1-\left(\frac{c_p}{c_r}\sin\theta_i\right)^2}}{\frac{\rho_p c_p}{\rho_r c_r}\cos\theta_i + \sqrt{1-\left(\frac{c_p}{c_r}\sin\theta_i\right)^2}} \quad (1)$$

where ρ, c, and θ_i are the density, speed of sound and incident angle, respectively. The subscripts p and r refer to products and reactants, respectively. From equation (1), for a nominal flat flame front, the reflection coefficient is a function of:

a. Temperature ratio across the flame front (through density and speed of sound, assuming the properties such as the specific heat ratio remain the same across the flame front)
b. Incident angle, θ_i

For a flat flame, for small angles of incidence, an increase in temperature leads to increase in reflection coefficient. In other words, the amplitude of the scattered wave increases with increase in temperature ratio.

For a turbulent premixed flame, the temperature ratio across the flame front is the same as that of a steady laminar flame, if preferential diffusion and curvature effects are neglected. However, along with incident angle, for a turbulent premixed flame, the reflection coefficient is strongly dependent on the flame front orientation angle relative to that of the acoustic wave. In the case of a turbulent flame, the wrinkling and the unsteady nature of the flame front gives rise to a wide range of local flame front orientation

* In this discussion, "nominally" flat flame is essentially a flat (unperturbed) flame that has the same temperature jump as the turbulent flame in consideration.

angles.[29,30,31] This means that the turbulent flame sees a wide range of local incident angles that are quite different from the nominal incident angle, depending on the orientation angle distribution of the flame front. For a given temperature ratio, the critical angle, the largest incident angle beyond which no transmission of acoustic waves is possible, is fixed, assuming no change in gas properties such as specific heats and molecular weights across the flame front. Even for a nominal incident angle that is less than the critical angle for that temperature ratio, some parts of the flame front see angles that are greater than the critical angle and thus have an influence on the average reflection coefficient of the turbulent flame front. This point is illustrated in Figure 3.

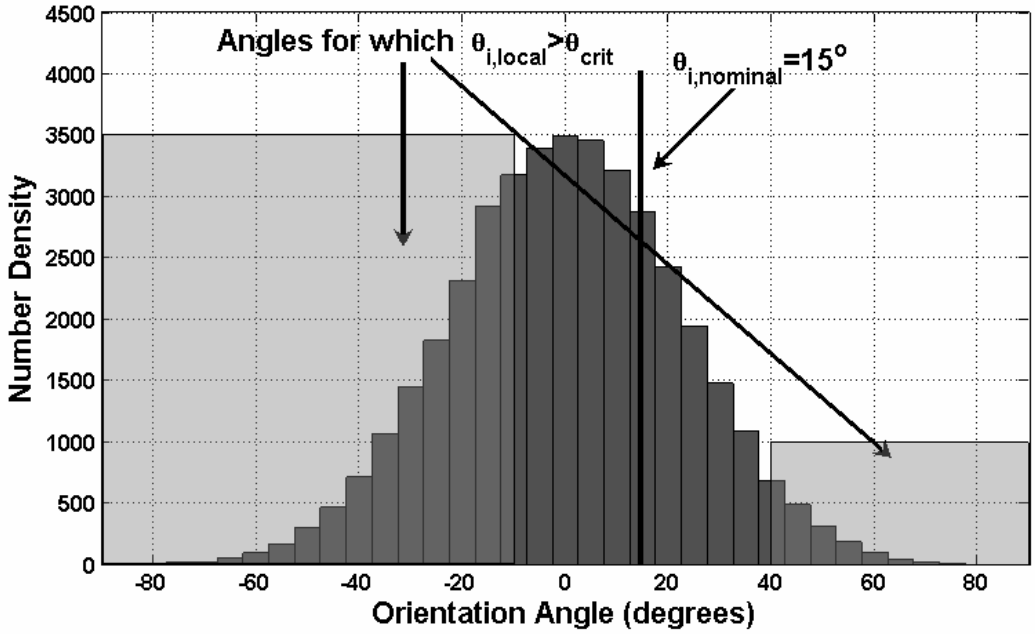

Figure 3. Cartoon illustrating incident angle (15^o), critical angle (25^o) and a Gaussian (hypothetical turbulent flame orientation angle) distribution. The shaded areas represent the flame orientation angles that see local incident angles greater than the critical angle.

Figure 3 plots a hypothetical flame front orientation angle distribution along with the incident angle (15^o) for a case corresponding to a critical angle of 25^o. Notice that

there are two ranges of flame orientation angles, as indicated by the shaded areas, from -90^o to -10^o and 40^o to 90^o, that see local incident angles greater than the critical angle. Acoustic waves incident at these instants/locations on the flame front will see a reflection coefficient of unity. These ranges of angles, which correspond to a reflection coefficient of unity, change with incident angle, critical angle and the orientation angle distribution.

In addition, if the temperature ratio across the flame front is changed by changing the equivalence ratio and thus flame speed, this will also affect the flame front orientation angle distribution.[30, 31]

From this discussion, we can summarize the parameters that affect the reflection coefficient of the turbulent flame as:

(a) Temperature ratio across the flame front

(b) Incident angle

(c) Orientation angle distribution of the flame front

While the analytical expressions derived in the above mentioned works are complicated, the basic physics of the scattered wave characteristics in the $\sigma/\lambda << 1$ case can be understood from straightforward Doppler shift considerations. If a harmonically oscillating acoustic wave, with frequency f_d, from a stationary source is incident upon a surface (flame front) moving with velocity u, then the reflected wave measured by a stationary observer (microphone) is given by:

$$f = f_d\left(\frac{a + u\cos\theta_i}{a - u\cos\theta_r}\right) \tag{2}$$

Where θ_i, θ_r, u and a are the incident angle, measurement angle, surface velocity of the scatterer (positive when moving towards the source and receiver), and sound

speed, respectively. For the physically interesting case of $u << a$, this equation can be simplified to:

$$f \approx f_d\left(1+\left(\frac{u}{a}\right)\left(\cos\theta_i+\cos\theta_r\right)\right) \tag{3}$$

This leads to an expression for spectral bandwidth:

$$\left\langle \left(f-f_d\right)^2 \right\rangle^{\frac{1}{2}} \approx f_d\left(\cos\theta_i+\cos\theta_r\right)\left(\frac{\left\langle u^2\right\rangle^{\frac{1}{2}}}{a}\right) \tag{4}$$

Similar expression for bandwidth can be arrived at using the analysis performed in Ref [10]. This formulation predicts a linear variation for bandwidth with driving frequency, the RMS velocity of the scattering surface and dependence on the incident and the measurement angles.

Laverdant and Thevenin[32] reported a DNS study, in which a Gaussian acoustic wave interacts with a turbulent premixed flame. In this study, the acoustic wave is incident from the products side. This study reported that the acoustic wave is modified and is wrinkled in a way similar to the flame front during its interaction with the reaction zone. It also reported that the heat release perturbations induced by the acoustic wave are negligible for acoustic wave amplitudes (~10 Pa) considered. Similar DNS study for the case where a Gaussian acoustic wave interacts with a non-premixed flame was performed by Laverdant *et. al.*.[33] In this study, the acoustic field was calculated for two cases: in the presence of (a) laminar flame and (b) turbulent flame. The existence of the incoherent acoustic field in the presence of the turbulent flame is confirmed by subtracting acoustic field of case (a) from (b). While the earlier study[32] did not include the calculation of the

incoherent component for premixed flame case, the results do suggest the existence of the incoherent field.

Scattering experiments by Lieuwen *et. al.*[34], performed on an axi-symmetric pilot stabilized premixed flame, confirmed the existence of the incoherent acoustic field. However interpretation of results is complicated by the choice of burner geometry. This issue will be discussed in detail in the next chapter.

There are a number of other ultrasonic scattering studies, primarily from heated jets and thermal plumes, that have reported features such as spectral broadening and Doppler shift of the incident acoustic wave. In those experiments, ultrasonic wave scattering was used as a diagnostic technique. The scattered field is expected to contain information regarding the scattering jet or thermal plume used in the study. They are discussed below.

Lund and coworkers[35,36] analytically studied the nature of the scattered field in low Mach number flows with temperature and vorticity inhomogeneities. They reported that in the forward scattering mode, $\theta < 90$, see Figure 4, the scattered field is influenced by vorticity and temperature fluctuations while in the back scattering mode, $\theta > 90$, the scattered field is mainly influenced by temperature fluctuations.

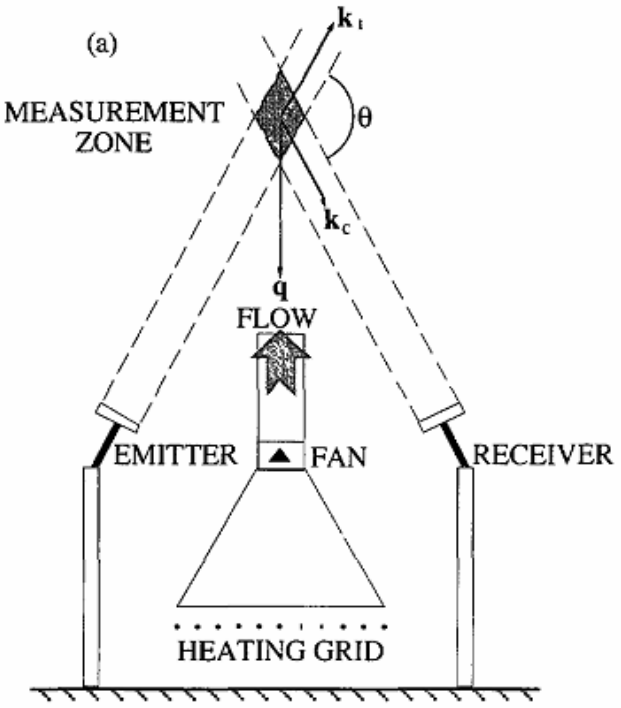

Figure 4. Typical Experimental set-up used in the ultrasonic scattering experiments from heated jets and thermal plumes. $\theta < 90^o$ corresponds to forward scattering mode and $\theta > 90^o$ corresponds to the back scattering mode. Schematic is reproduced from a publication by Petrossian and Pinton[38].

Pinton *et al*.[37] have reported acoustic wave scattering measurements off a thermal plume in back scattering mode. The scattered field spectrum showed a distinct band of frequencies in the presence of heated jet. They were able to relate the frequency with maximum power to the mean advection velocity of the jet. They suggested that the band of frequencies near the incident wave frequency are generated by phase modulation processes induced by the temperature fluctuations. They further reported scattered field spectrum for the case where the jet was externally forced at 3 Hz. For this case, the scattered filed spectrum showed discrete peaks at 3 Hz intervals near the incident wave frequency.

In experiments similar to that of Pinton *et al*.[37], Petrossian and Pinton[38] measured acoustic waves scattered off a heated jet in back scattering mode. They too were able to relate the scattered field spectrum to the advection velocity. In addition, they reported that the bandwidth of the scattered field increased with incident frequency.

Similar experiments on thermal plumes were reported by Elicer-Cortes and coworkers.[39,40,41,42] These studies reported on different characteristics of the thermal plume such as turbulence intensity, transition to turbulence, temperature spectra, etc. By measuring the scattered field in forward scattering mode ($\theta = 50^o$), they were able to estimate the size of the vorticity patterns induced by externally forced disturbances.

While many other experimental studies (e.g., Samaniego et al.[43], Broda et al.[44]) have been carried out to quantify the flame acoustic wave interactions, these measurements are heavily influenced by the overall combustor system and thus are more properly characterized as combustor system-acoustic wave interaction measurements. No fundamental experimental studies seem to have been performed to understand the dependence of the scattered acoustic field on the flame characteristics such as flame brush thickness, flame front orientation angle distribution etc. The objective of this study is to experimentally examine the statistical characteristics of scattered acoustic field by the turbulent flame and determine the dependence of the scattered field on flame characteristics.

1.3 Overview of the Present Study

The objective of this thesis is to characterize the scattered acoustic field from turbulent premixed flames. A number of parameters such as the wavelength of the acoustic wave, scale of flame front wrinkling (flame brush thickness), incident and

measurement angles (θ_i, θ_r), mean velocity and flame speed (u'/S_L), are expected to play a role in these interactions. This thesis addresses the role of these parameters in the scattering process.

The outline of this thesis is as follows:

Chapter 2 describes the experimental facility and the instrumentation for (i) Cold flow characterization (ii) Flame front characterization and (iii) Scattered field measurements.

Chapter 3 describes the cold flow characteristics of the burner. Mean flow profiles, turbulent velocity profiles and the range of turbulence intensities available for this study are detailed in this chapter.

Chapter 4 describes the flame front statistics determined from flame cross-section images. First, it describes the steps involved in estimating the flame front statistics from the images. Then, it describes the dependence of flame front statistics on parameters such as turbulence intensity, flame speed and mean velocity.

Chapter 5 describes the nature of the measured scattered field and its dependence on parameters discussed in this chapter.

Chapter 6 presents the conclusions of this research and recommendations for future work.

Chapter 2
Experimental Facility and Instrumentation

This chapter describes the experimental facilities, instrumentation and measurement techniques that were employed in this study. The first section explains the details of the slot burner facility that was used to generate the turbulent flame. Cold flow characterization of this facility is described in section 2. Then, Acoustic instrumentation is described in section 3, flame front imaging setup in section 4, and data acquisition components in section 5.

2.1 Slot Burner Facility

An axi-symmetric burner was used at the beginning of the study. In this configuration, the incident wave must propagate through the hot product/ambient air interface before reaching the flame, as illustrated in Figure 5. Because of the temperature variation, this interface scatters the incident acoustic waves, which adds complexity to the problem. In order to isolate the interactions between the flame and the acoustic waves, a slot burner with pilot flame on only one side of the burner was fabricated. In this configuration, the acoustic waves are generated on the reactant side of the flame.

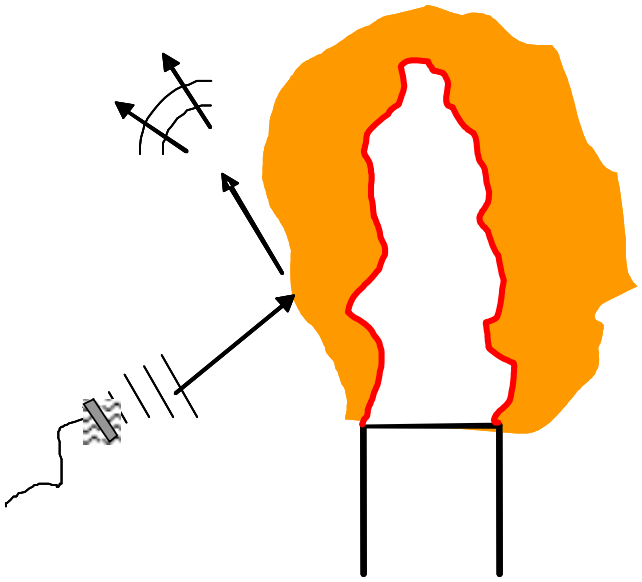

Figure 5. Scattering from an axi-symmetric turbulent flame.

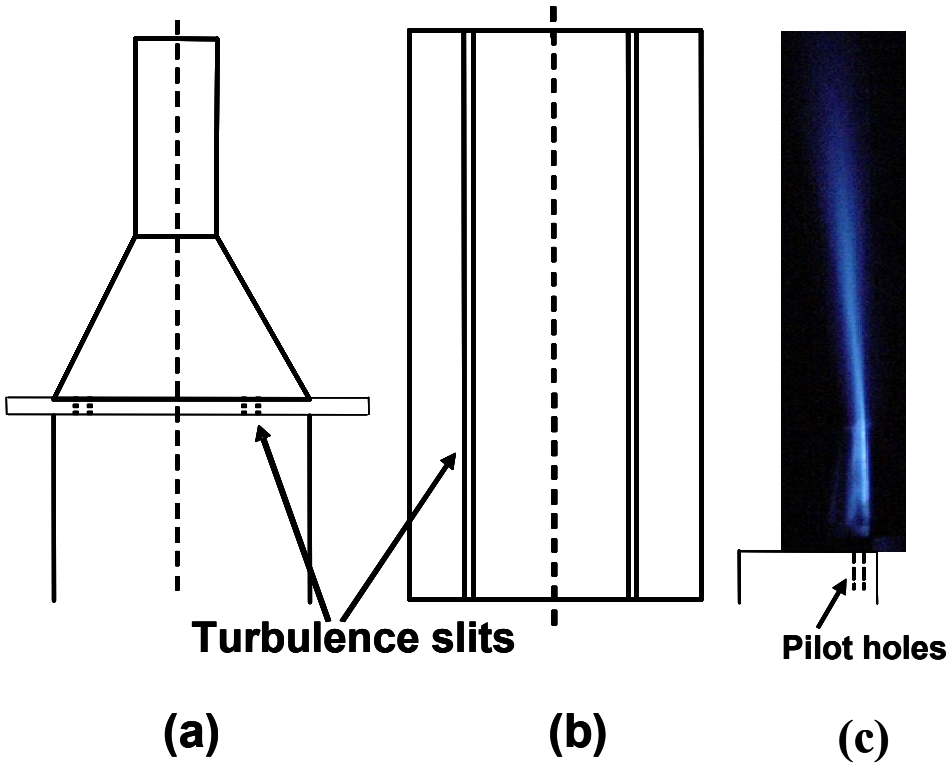

Figure 6. (a) Schematic of the slot burner: constant area section followed by slit arrangement, converging area section and the burner (b) Top view of the slits used for turbulence generation (c) Side view of the typical flame generated by the slot burner.

A schematic of the slot burner is shown in Figure 6. The burner consists of a constant area section followed by turbulence generating slits and a converging area section. The exit of the burner is 15 cm long and 1.5 cm wide. There are 42 pilot holes, each of 2.1 mm diameter on one side of the burner. Because of this configuration of pilot holes, the flame is anchored on only one side of the slot burner. A premixed turbulent reactive mixture exits from the slot burner at atmospheric pressure. The flame is stabilized at the burner exit by the pilot flame. Notice that the flame front width remains unchanged in the case of slot burner as opposed to axi-symmetric burner. A side view of a typical flame generated by such a configuration is shown in Figure 6(c).

From the introduction chapter, the scale of flame front wrinkling (flame brush thickness, σ) is expected to play an important role in these interactions. In this study, this parameter is varied by changing the turbulence intensity, independent of other flow variables such as mean velocity and fuel to air ratio. Turbulence intensity is varied using a symmetric slit arrangement, as suggested by Videto and Santavicca.[45] As the flow goes through the slits, as shown in Figure 6, symmetric vortices are generated, convected downstream, and impinge upon the converging section where they break down. The energy in these vortices is converted to fine scale turbulent fluctuations, thus enhancing the turbulence intensity. The turbulence intensity is controlled by varying the width of the slits. Four slits with different widths, along with a no slit configuration give rise to five different turbulence intensities. The setup for cold flow characterization is discussed in the following section.

2.2 Hotwire Measurements

The burner characteristics such as the velocity and the turbulence intensity profiles for different slits are measured using a hot wire probe. A DANTEC 55P11 constant temperature hotwire anemometer (CTA) was used for this purpose. The hotwire probe, with a wire diameter of 5 μm, is held using a straight probe holder. The hotwire probe is traversed across the burner. Velocities are measured at 11 locations along the width of the burner, three locations across the breadth (3, 7, and 11 mm from the pilot side) for two heights (4 cm and 6.5 cm from the burner exit). The measurement locations are illustrated in Figure 7.

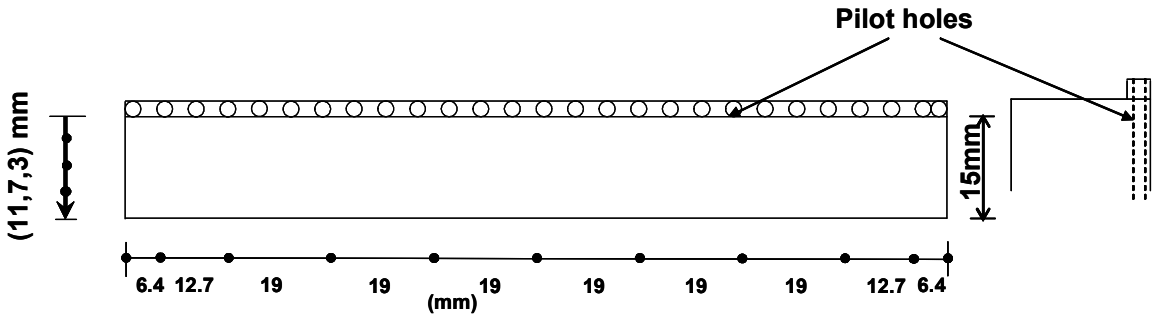

Figure 7. Hotwire measurement locations, 11 locations along the width and 3 locations along the breadth, indicated by dots. Measurements were performed at two heights: 4 cm and 6.5 cm from the burner exit.

2.3 Acoustic Instrumentation

Acoustic disturbances are generated using a 25.4 mm Vifa speaker (Model #D27TG4506) that is located approximately at 93 cm from the mean flame. The source was located approximately at height of 50 mm from the lip of the burner. The scattered acoustic field was measured using Bruel and Kjaer 6.5 mm microphones, which were located at 100 cm and inclined at angles of 0^o, 10^o, 25^o and 35^o, respectively, with the

mean flame front as shown in Figure 8. The majority of the experiments were performed for 1-24 kHz driving frequencies. The details of the acoustic transducer and the microphones are described below.

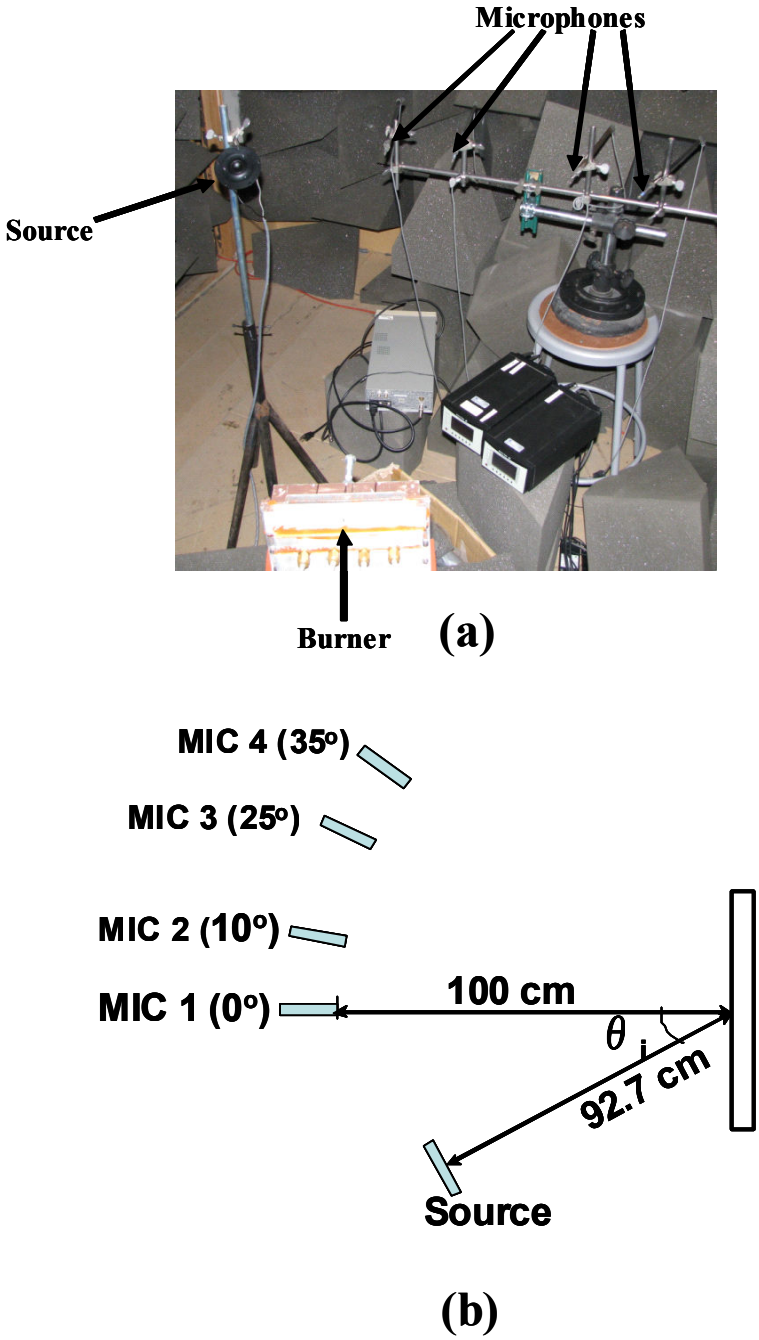

Figure 8. (a) Picture of the experimental setup. (b) Top view of the experimental setup: Arrangement of the acoustic source, burner and the microphones. The incident angle, θ_i, is varied from 10^o-45^o. The acoustic instrumentation is on the side of the reactants.

2.3.1 Acoustic Source

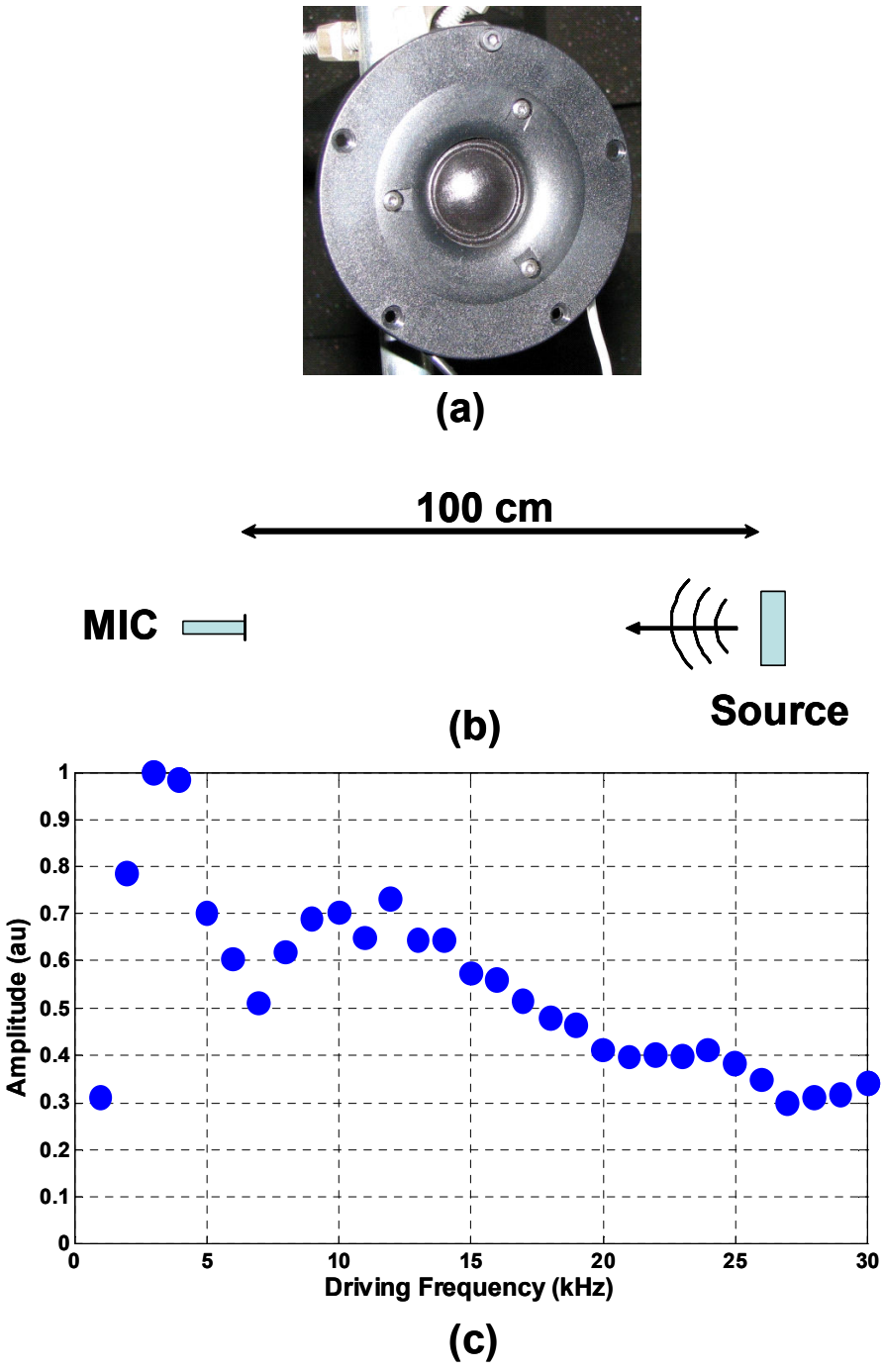

Figure 9. (a) Source used in the study (b) Setup to measure the response of the source (c) Amplitude response of the source with frequency.

A 1" VIFA transducer (model # D27TG4506), shown in Figure 9(a), was used to generate the acoustic perturbations. The response of the source with frequency was determined using the setup shown in Figure 9(b). The source was driven at a constant voltage and the corresponding acoustic amplitude was measured with a microphone that was positioned facing the source (0^o), for 1-30 kHz frequencies. The measured response of the source with frequency is shown in Figure 9(c). These measurements were used to correct the scattered acoustic field at different frequencies.

Figure 10 shows the experimental setup used to evaluate the directivity patterns of the source. The source was rotated through 360^o in steps of 5^o, with the microphone fixed at 30 cm from the source. Such directivity patterns were obtained for multiple frequencies. Figure 11 plots the directivity measurements for two sources: (a) 100 mm speaker and (b) 38 mm transducer. The measured directivity patterns were compared with theoretical expressions for an infinite, baffled piston[46] for two frequencies. Notice that the sources are enclosed on one side, while the analytical expressions are derived for a non-enclosed case. For this reason comparisons can only be made in the forward direction. First, directivity pattern of the source changes with frequency. Second, good agreement (within 3% between -5^o to 5^o and 2% between -10^o to 10^o) is seen between the measurements and baffled piston theory. With this knowledge of good agreement, theoretical directivity patterns are generated for the whole frequency range for the source (VIFA 25.4 mm speaker) used in this study. Such calculated directivity patterns are used to make corrections for the scattered field at different frequencies.

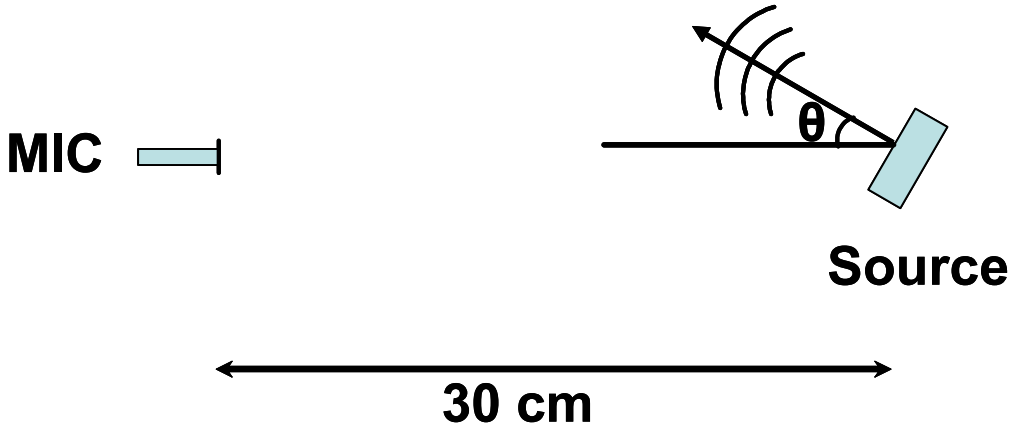

Figure 10. Set up to measure the directivity pattern of the source. Source is rotated though 360^{o} in steps of 5^{o}, with the fixed microphone measuring the amplitude at each angle.

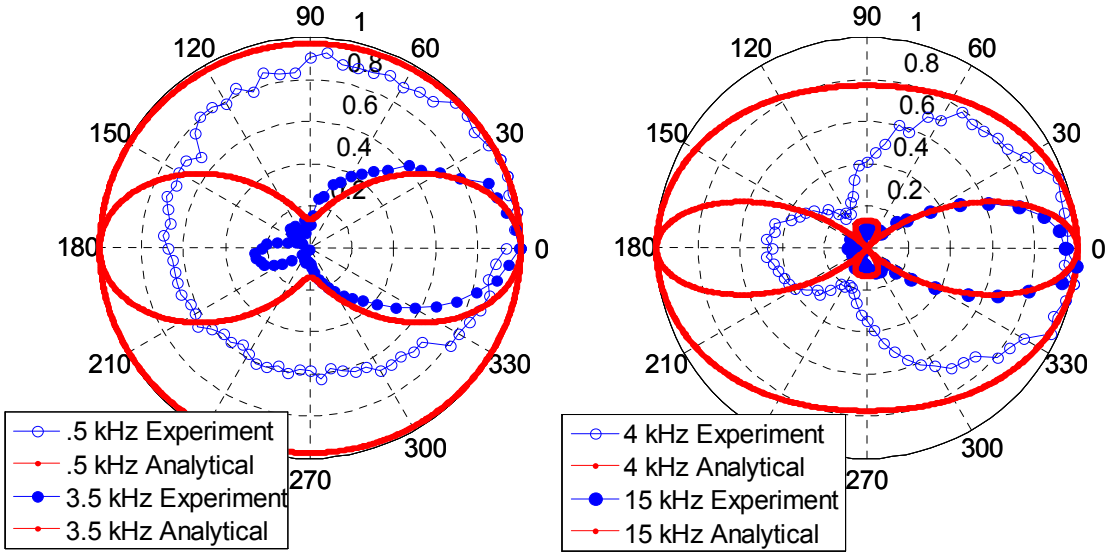

(a) 100 mm Source (b) 38 mm Source

Figure 11. Directivity patterns for (a) 100 mm source for 500 Hz and 3500 Hz and (b) 38 mm source for 4 kHz and 15 kHz, compared with theoretical predictions. Comparisons can only be made in forward direction because of the enclosed source in the experiment.

2.3.2 Microphones for Scattered Field Measurement

Four Bruel & Kajer 6.5 mm microphones were used to measure the scattered field from the flame (3 type 4939, 1 type 4135). The sensitivity of each microphone is listed in Table 1. These microphones have flat response up to 100 kHz. Directivity corrections similar to that of the acoustic source are performed on the measured scattered acoustic field. The signal from the microphone is conditioned and amplified by the signal conditioner. This signal is then filtered and acquired by the DAQ computer.

Table 1. Sensitivities of the microphones used in this study.

MIC #	Model #	Sensitivity (mV/Pa)
1	4939	3.96
2	4939	4.18
3	4939	4.36
4	4135	3.55

2.4 Setup for Flame Front Imaging

Both vertical and horizontal cross-sectional images of the flame front were obtained in this study. The set ups for flame front imaging (a) Vertical and (b) Horizontal cross sections are illustrated in Figure 12. The air/fuel mixture is seeded with olive oil particles (median size of 4 microns, obtained from PDPA measurements). The olive oil particles are generated using a Laskin nozzle design, with the nozzle immersed in the oil. These particles evaporate at the flame and thus leave bright and dark regions of reactants and products, respectively, demarcated by the flame edge. A laser beam from an 8W

Coherent Innova 90 continuous Argon-ion laser (λ=514.3 nm), circular in cross-section, was converted into a sheet using a cylindrical lens. A plano-convex lens was used to reduce the thickness in the direction perpendicular to the laser sheet to approximately 1 mm. 2000 images were obtained at 500 frames/second with an exposure time of 25 μs.

For vertical cross-sectional images, an area of 150 mm x 35 mm was captured at 512 x 128 camera resolution giving approximately 0.3 mm/pixel resolution. Vertical flame images were obtained at three locations across the width of the burner. Horizontal cross-sectional images were obtained at 512 x 512 camera resolution, at approximately 0.46 mm/pixel resolution. Such images were obtained at two or three heights for each flame, depending on the flame height. These images were captured with a high speed, intensified camera (Videoscope International Ultracam3). The image processing techniques and the statistics of the flame front are described in detail in chapter 4.

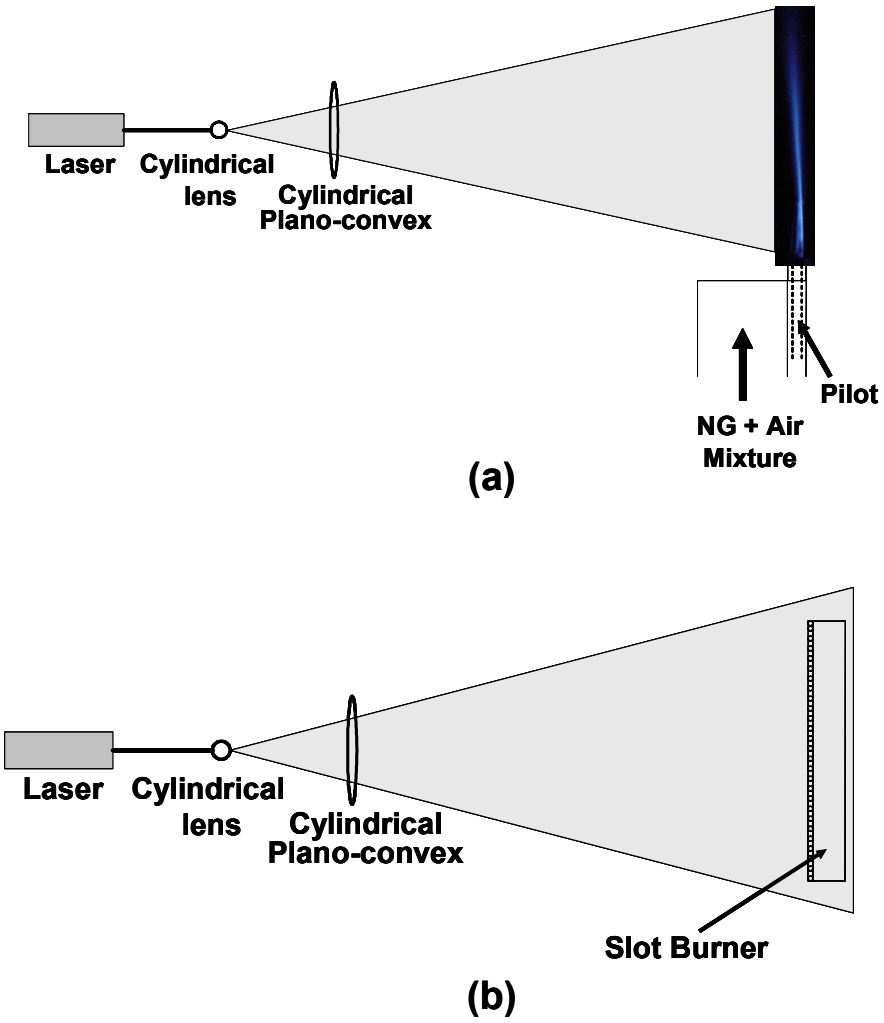

Figure 12. Set up for flame front imaging: (a) Vertical cross-sectional images (b) Top view of the experimental setup used to capture Horizontal images. Cylindrical lens is used to convert the circular laser beam into a sheet. The Plano-convex lens is used to reduce the laser sheet thickness in the direction normal to the laser sheet.

2.5 Components of Data Acquisition

Different elements of the data acquisition set up are shown in Figure 13. A harmonic signal at the desired frequency is generated with a function generator. This signal is amplified using an amplifier, which is then used to drive the acoustic source. The scattered field is measured using a microphone, which is connected to the signal

conditioner. The signal is sent through a band pass filter, which is then acquired by the data acquisition computer.

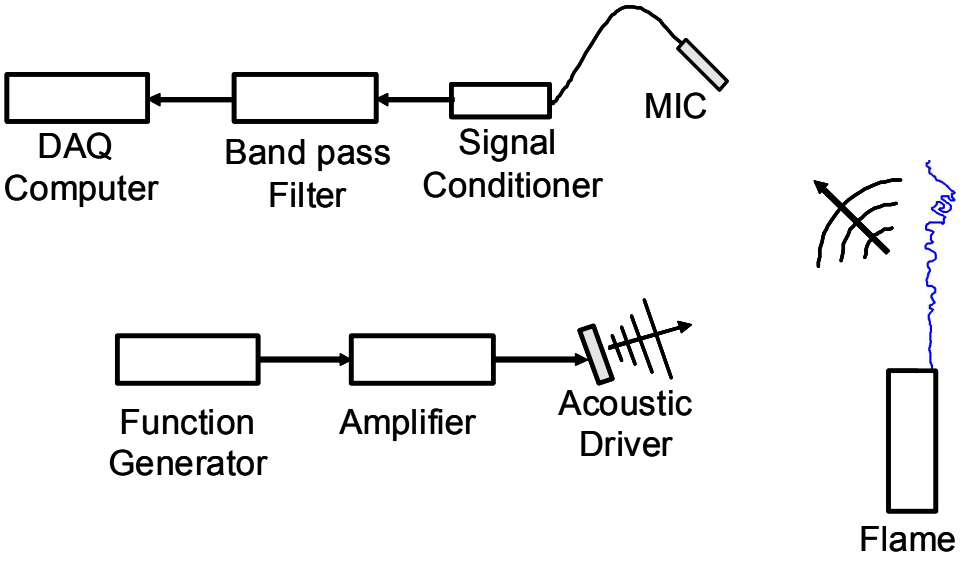

Figure 13. Components of the Data acquisition setup.

The signal to the acoustic driver is derived from a HP 33120A precision function generator. Figure 14 shows the power spectrum for a case where the signal from the function generator is acquired through the DAQ board for a driving frequency of 20000 Hz and 20000.5 Hz. The spectrum has 1 Hz resolution. Notice that there is significant amount of leakage in the case of 20000.5 Hz. It illustrates the necessity for an accurate signal from the function generator.

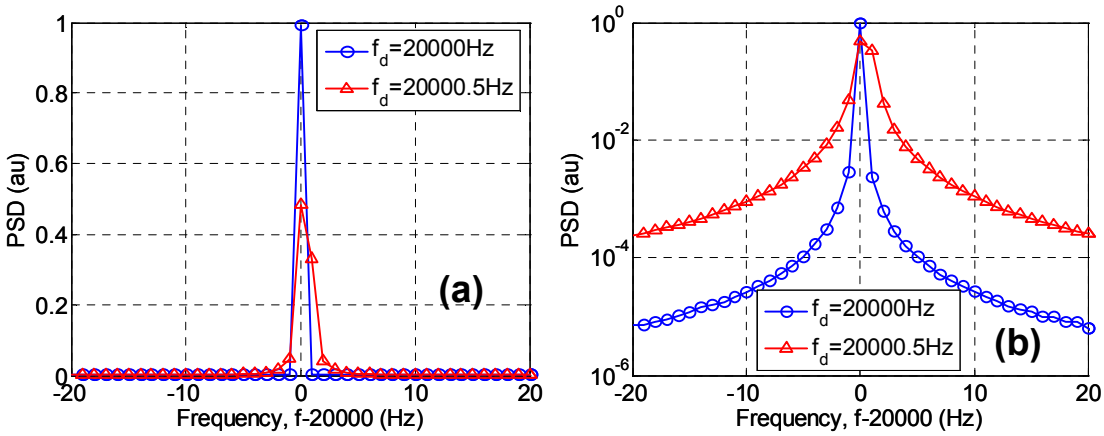

Figure 14. Spectra to illustrate the leakage phenomenon because of inaccuracy in the driving frequency. Frequency, f_d = 20000 Hz and 20000.5 Hz, resolution = 1 Hz. X-axis is translated to zero for clarity (a) Linear scale (b) Log scale.

The frequency stability of the function generator is quantified in Figure 15. The signal from the function generator is acquired at 1 kHz steps from 1 kHz to 25 kHz for 10 seconds each. Power spectrum is calculated at 1 Hz resolution for each frequency. The ratio of the power at driving frequency to frequency immediate on either side is calculated (e.g.: for 1 kHz, ratio of powers at 1000 Hz to 1001 Hz and 1000 Hz to 999 Hz are calculated). This ratio is plotted against driving frequency in Figure 15. It shows that the signal generated by the function generator is very narrowband (~40 dB or 4 orders of magnitude drop within 1 Hz).

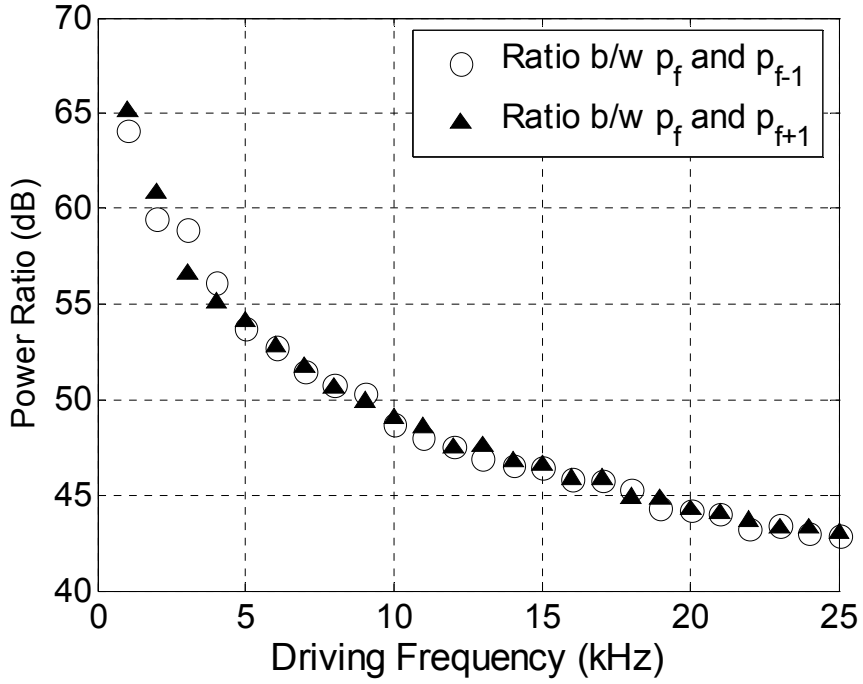

Figure 15. Ratio of power at the driving frequency to its immediate frequencies in the spectrum.

The signal from the function generator is amplified using a RadioShack amplifier (MPA-101). This amplified signal is used to drive the acoustic source. The response is measured using a microphone. The spectrum for the case where driving frequency is 20 kHz is plotted in Figure 16. Notice that the spectrum is extremely narrow and the power drops approximately 40 dB within 1 Hz suggesting that the distortion from the different components is negligible.

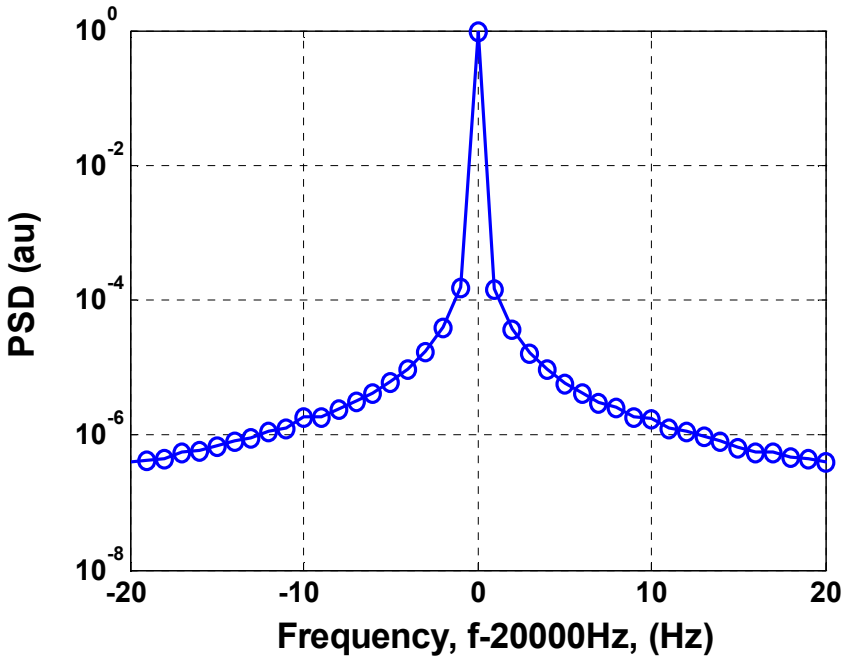

Figure 16. Power spectrum for 20 kHz driving frequency, after the signal has passed through different data acquisition components, as shown in Figure 13, except the flame.

The scattered acoustic field from the flame was measured using microphones, fed to a signal conditioner which amplified the signal and sent through a low pass filter to reduce high frequency electrical noise. Then the signal is high pass filtered to enhance the dynamic range of the DAQ card. This filtered signal is acquired using a LABVIEW interface through a 12 bit NI DAQ card. The dynamic range is varied for each case to maximize the resolution of the A/D card and minimize the digitization error. Data is acquired for 1-24 kHz driving frequencies at a sampling frequency of 50 kHz. 5 Million points (100 seconds at 50 kHz sampling frequency) are acquired at each driving frequency, which gives 200 ensembles at 2 Hz resolution in the frequency spectrum. The details of the data reduction are described in the Appendix A.

Chapter 3

Cold Flow Characterization

This chapter describes the cold flow characteristics of the slot burner in detail. Hot wire measurements were performed on the slot burner for different turbulence generators. Measurements were performed for two velocities, 4.4 m/s and 3.1 m/s, based on the volume flow rates and the burner exit area. Measurements were performed at two heights (4 cm and 6.5 cm measured from the burner exit), and at 3 locations (3, 7 and 11 mm) across the breadth of the slot. Details of the setup are discussed in chapter 2. The mean velocity, turbulence intensity profiles and turbulent kinetic energy (TKE) spectra presented here correspond to the height of 4 cm. In the discussion below two definitions of mean velocities are used:

(i) U_m, nominal mean velocity based on the volume flow rate and the burner exit area

(ii) $\overline{U}$, local mean velocity, as measured by the hot wire probe

Details of the mean velocity, RMS velocity profiles and TKE spectra are described below.

3.1 Mean Velocity

Figure 17(a) plots the mean velocity for two flow velocities along the width of the burner for the 4.5 mm slit case. Measurements were performed near the center line (7 mm

from the pilot side). The mean velocity profile is not symmetric about the center (7.5 cm on x-axis), as can be seen as a sharp drop at 0 cm. The reason for this is that the nominal 0 cm location of the probe is placed in the shear layer outside the burner slot. Figure 17(b) plots the mean velocity profile normalized by the nominal velocity, U_m. Mean velocity profiles are observed to scale well with the nominal velocity.

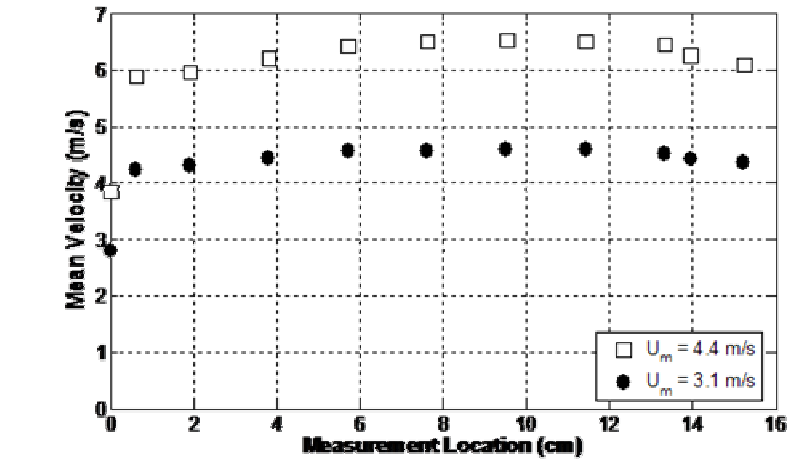

(a)

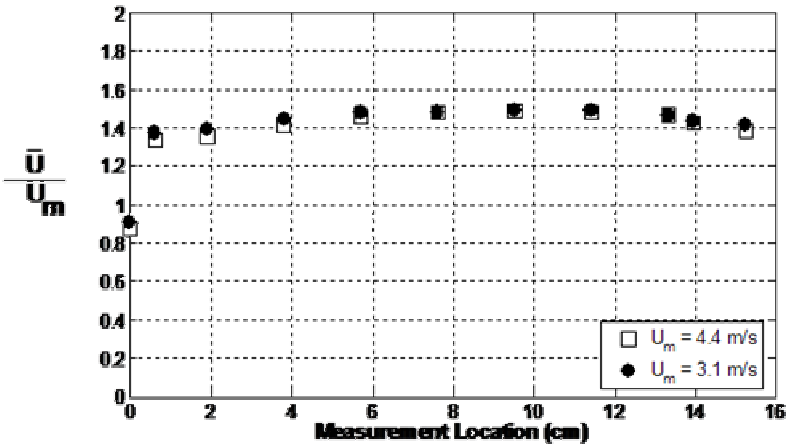

(b)

Figure 17. Mean velocity profiles measured near the center line at 4 cm height for 4.5 mm slit for two flow rates. (a) Mean velocity plotted along the width of the burner (b) Measured mean velocities divided by the corresponding nominal velocity, U_m.

Figure 18 plots the mean velocity profile at three locations, 3 mm, 7 mm and 11 mm from the pilot side, for 4.5 mm slit configuration for U_m=4.4 m/s. Notice that the mean velocity closest to the pilot side (3 mm) has higher velocity compared to the 11 mm side. This is because of the pilot lip that extends beyond the burner exit by 9 mm and, thus, delays the velocity decay.

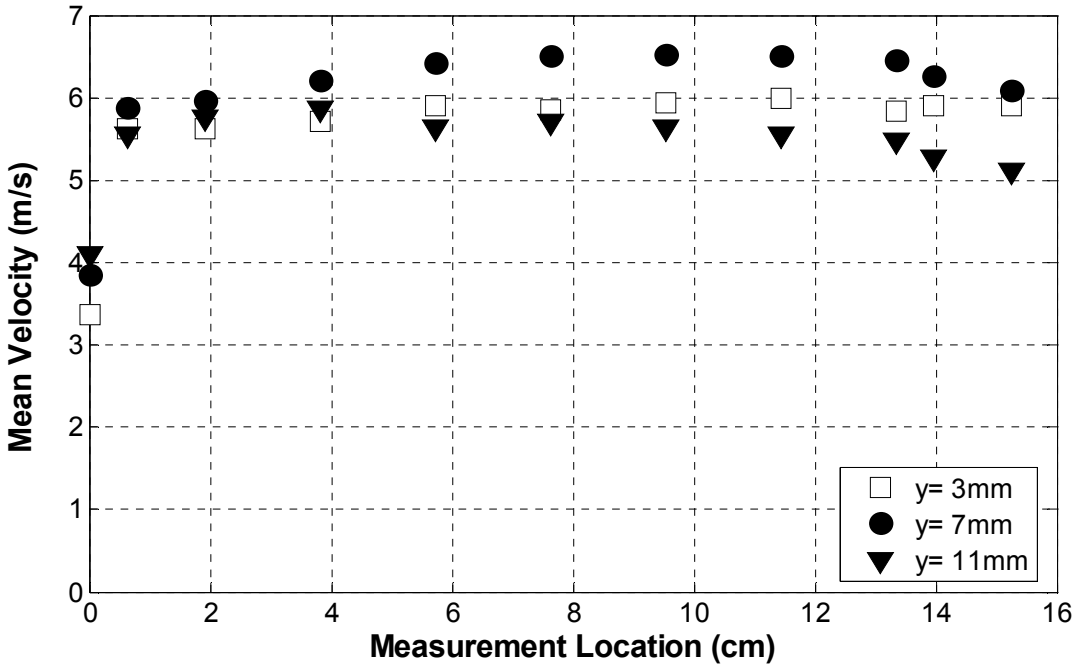

Figure 18. Measured velocity at three locations along the breadth of the burner slot for 4.5 mm slit configuration for U_m = 4.4 m/s.

Figure 19 plots the mean velocity along the width of the burner for U_m = 4.4 m/s for the five turbulence generators, measured near the center line. Notice that the mean velocity decreases as the slit width decreases. Similar plots at 3 mm and 11 mm from pilot side (not shown here) show similar trends suggesting that the jet expands faster as the slit width is decreased.

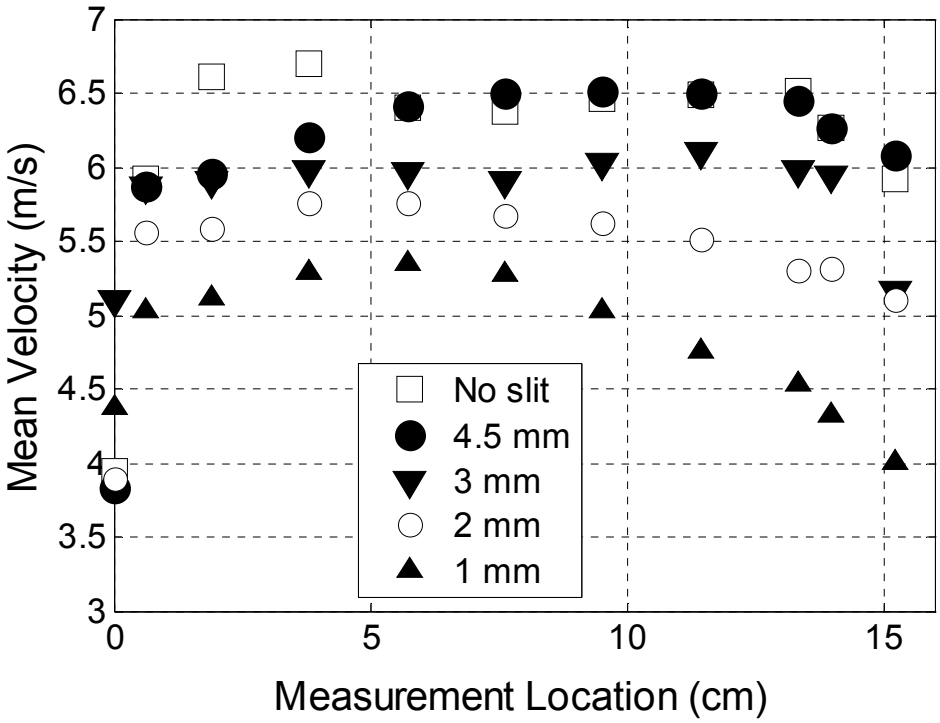

Figure 19. Mean velocity profiles measured near the center line along the burner width plotted for different turbulence generators for $U_m = 4.4$ m/s.

3.2 RMS Velocity

Figure 20(a) plots the RMS velocity profile along the width of the burner for two velocities near the center line (7 mm from the pilot side) for 4.5 mm slit case. As expected, increasing the mean velocity increases the RMS velocity. Also, the velocity fluctuations are large at 0 cm compared to the other locations, which is consistent with the observation that the hot wire probe location is located outside the burner, as pointed out earlier. Figure 20(b) plots the turbulence intensity based on the nominal mean velocity, U_m. Notice that the turbulence intensity varies in a similar manner for both the

flow rates, suggesting that the turbulent velocities fluctuations scale with the mean velocity.

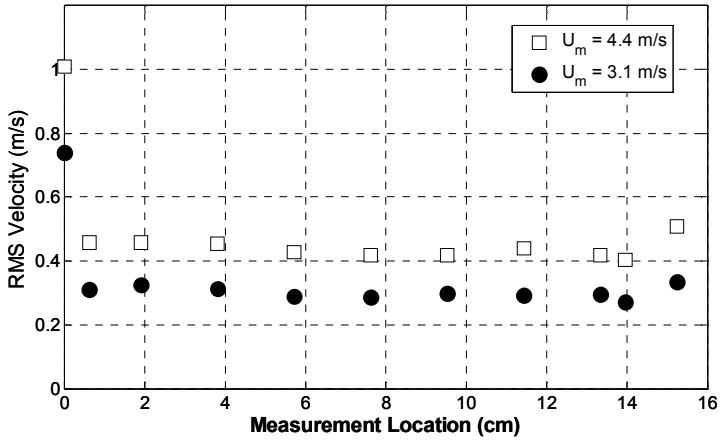

(a)

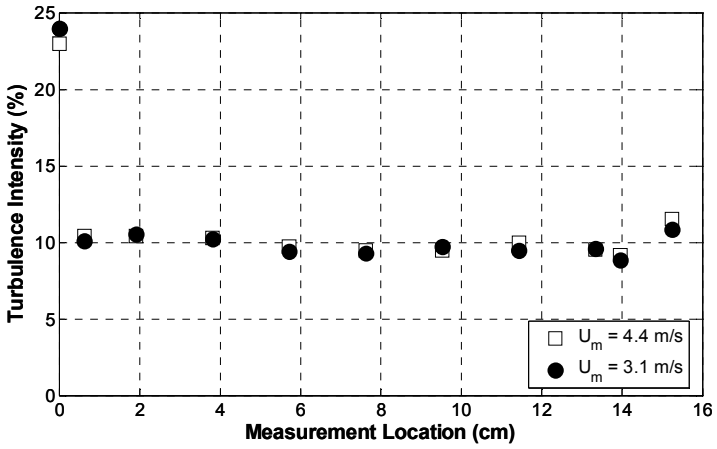

(b)

Figure 20. (a) RMS velocity, measured near the center line, along the width of the burner for 4.5 mm turbulence generator for two mean velocities (b) Turbulence intensity based on nominal mean velocity, U_m.

RMS velocity, measured near the center line, is plotted along the width of the burner for all 5 slits in Figure 21 for U_m = 4.4 m/s. Notice that the fluctuations change by a factor of 3, from 20 cm/s to 60 cm/s for no slit configuration to the smallest (1 mm) slit.

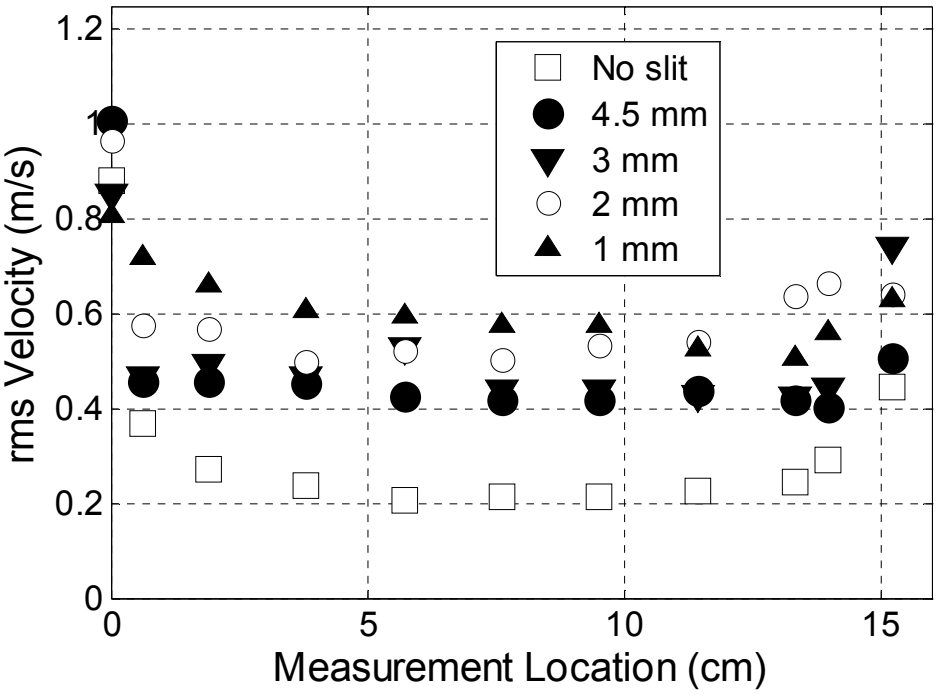

Figure 21. RMS velocity fluctuations near the center line plotted against the width of the burner for different turbulence generators for Um = 4.4 m/s.

Turbulence intensity is calculated from RMS fluctuations using two velocity definitions: based on the nominal mean velocity, U_m, plotted for different slits in Figure 22(a), and the local mean velocity, $\overline{U}$, plotted in Figure 22(b). Turbulence intensity varies from 5-14% based on the nominal mean velocity and 4-12% based on local mean velocity.

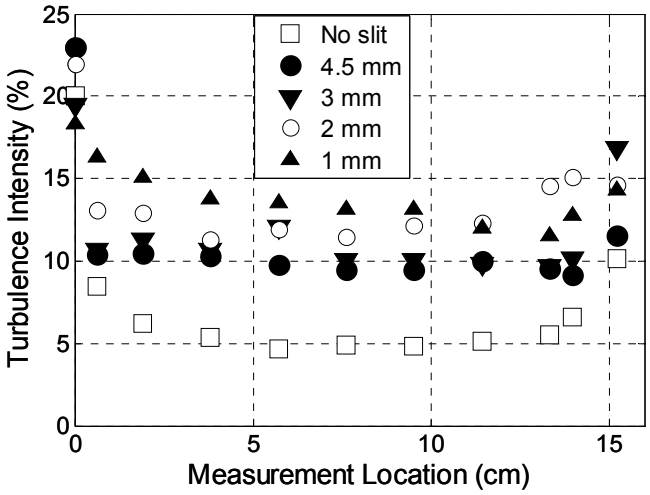

(a)

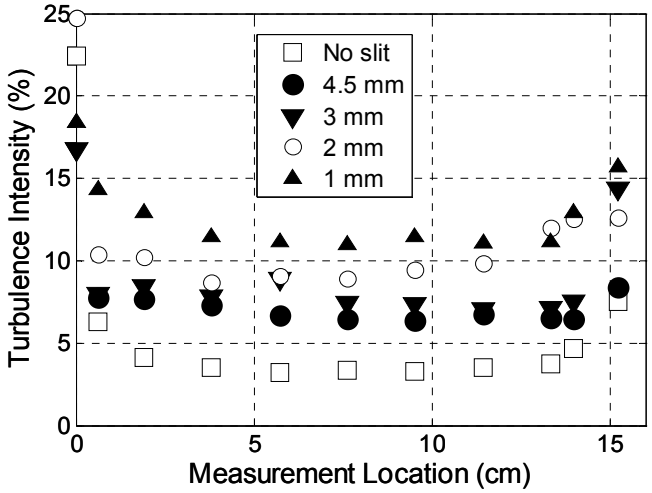

(b)

Figure 22. Turbulence intensity calculated using two definitions of mean velocity: (a) Nominal mean velocity, U_m (b) Local mean velocity, $\overline{U}$.

The effects of mean velocity and turbulence intensity on the flame front characteristics are described in chapter 4.

3.3 Velocity Spectra

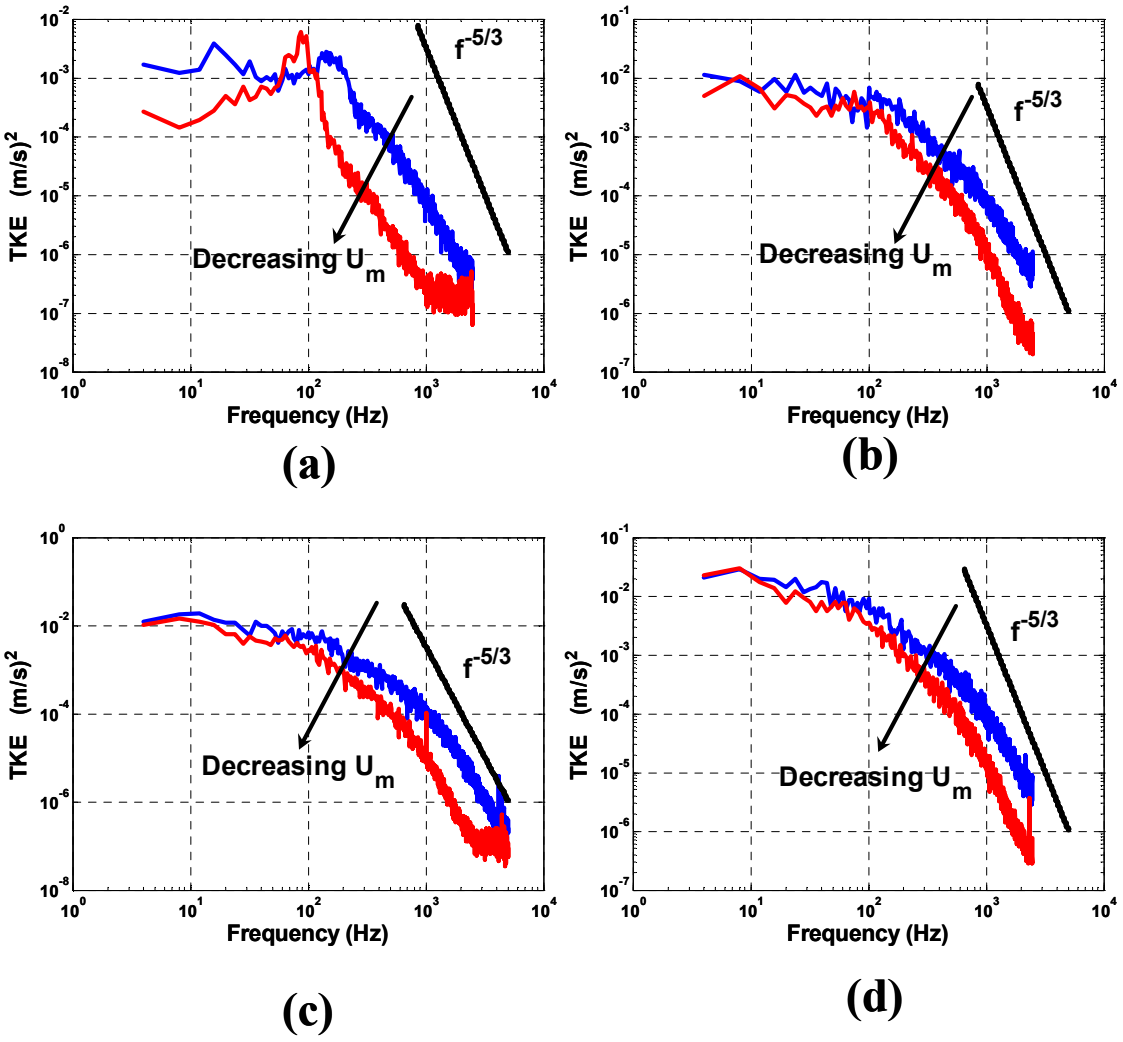

Figure 23. 1-D Turbulent Kinetic Energy spectra measured near the center line for four turbulence generator cases for two mean velocities, 4.4 m/s and 3.1 m/s. (a) No slit configuration (b) 4.5 mm slit (c) 3 mm slit and (d) 2 mm slit.

Figure 23 plots the 1-D turbulent kinetic energy spectra for four turbulence generators. We see that the frequency at which the roll-off occurs changes with the mean velocity. Also, for the no slit configuration, Figure 23(a), inertial sub-range is seen to extend over a decade of range of scales. For 4.5 mm slit, Figure 23(b), we see that the

inertial sub-range begins at higher frequency compared to No slit configuration. However, further decrease in slit width does not show any significant change in the inertial sub-range, see Figure 24.

Notice that for the 3 mm slit case, Figure 23(c), spectra shows a distinct peak at 1000 Hz for the lower velocity (3.1 m/s). No such peak is observed for the 4.4 m/s case. At large amplitudes, such periodic acceleration and deceleration could have an influence on the flame front.[22] However, at the amplitudes seen in Figure 23(a), the effect on flame front is expected to be negligible. Indeed, the flame front characteristics, as will be discussed in chapter 4, do not show any dependence on mean velocity, despite the tone being preset for the lower velocity and absent for the higher velocity. This observation is further discussed in chapter 4.

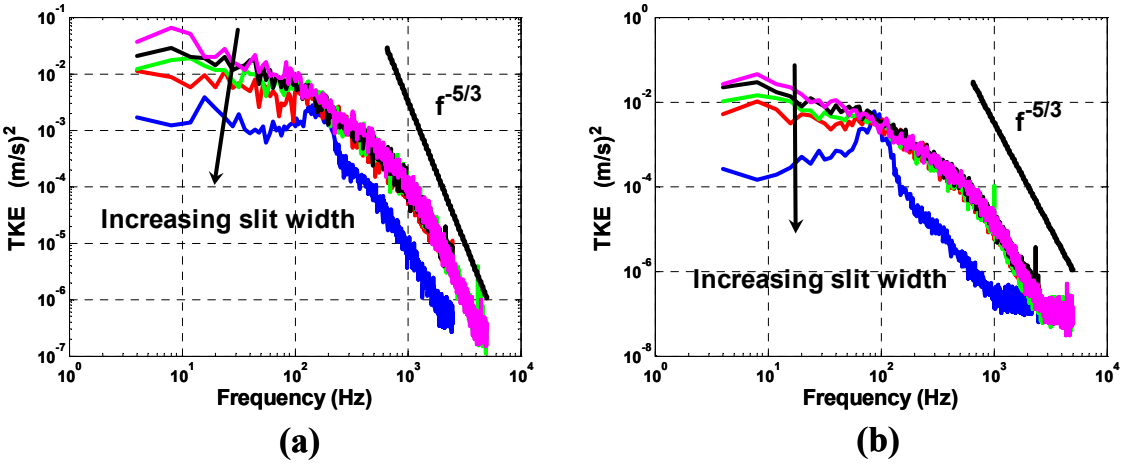

Figure 24. 1-D Turbulent Kinetic Energy spectra plotted for multiple slit configurations (a) 4.4 m/s and (b) 3.1 m/s.

Chapter 4

Flame Front Statistics

This chapter describes an analysis of turbulent flame front statistics, such as the flame front location and orientation angle. The objectives for this study are two fold:

(i) To provide detailed experimental characterization of the flame front

(ii) To provide data for correlating the measured acoustic field to the flame front

Both vertical and horizontal cross-sectional images of the flame front were obtained at flow conditions listed in Table 2. Commercially available natural gas (97% Methane) was used as fuel. The setups for image acquisition are detailed in chapter 2. Recalling the discussion in chapter 1, the following characteristics of the flame front were obtained for both vertical and horizontal cross-sectional images:

(i) Flame brush thickness: The scale of turbulent flame front wrinkling, flame brush thickness (σ), from theoretical considerations presented in chapter 1, is expected to play an important role in the coherent to incoherent energy transfer process.

(ii) Orientation angle distribution: The average reflection coefficient of the turbulent flame is dependent on the orientation angle distribution. In addition, orientation angle distribution also plays a role in the spatial distribution of the scattered field. The orientation angle distributions in the vertical plane, θ_V, and the horizontal plane, θ_H, influence the spatial distribution of the scattered field in different ways. For this reason, both

vertical and horizontal cross-sectional images of the flame front were obtained.

(iii) Curvature: From a geometrical viewpoint, prescription of flame surface area, orientation and curvature represents a complete set of data required to describe a convoluted surface because these quantities are related to the zeroth, first and second derivatives of the flame front coordinates.[47] For completeness, curvature statistics are evaluated.

In addition, vertical flame front images were obtained with acoustic forcing to determine if flame front characteristics were altered with acoustic forcing at typical acoustic amplitudes used in this study.

This chapter is organized as follows. First, the edge detection methodology from the Mie scattered images is described. Next, the steps involved in estimating the flame front characteristics from the edges are detailed. The third section describes the above mentioned flame front characteristics and their dependence on the flow variables, such as turbulence intensity and mean velocity. The last section describes the effect of acoustic forcing on the flame front characteristics.

Table 2. Experimental conditions corresponding to the acquired vertical and horizontal images. Turbulence intensity is measured near the centerline at a height of 4 cm from the burner exit.

Slit	Turbulence intensity (%)	u'/S_L			
		$U_m = 3.7$ m/s $S_L = 0.17$ m/s	$U_m = 3.7$ m/s $S_L = 0.23$ m/s	$U_m = 4.7$ m/s $S_L = 0.17$ m/s	$U_m = 4.7$ m/s $S_L = 0.23$ m/s
No Slit (S1)	5.6	1.22	0.90	1.55	1.14
4.5 mm (S2)	9.8	2.13	1.58	2.70	2.00
3.0 mm (S3)	10.3	2.24	1.66	2.85	2.10
2.0 mm (S4)	12.7	2.77	2.04	3.51	2.60
1.0 mm (S5)	13.4	2.92	2.16	3.70	2.74

4.1 Edge Detection

In this section, the details of edge detection are described for vertical cross-sectional images. The same scheme is applied to extract edges from the horizontal images.

Cross sectional images of the flame front are captured using a high speed, intensified camera. Typical images obtained from the slot burner flame, after correcting for laser sheet intensity variation with height, are shown Figure 25. Notice that the left edge is sharp compared to the right side. This is due to the fact that the flame front exists only on the left side of the burner.

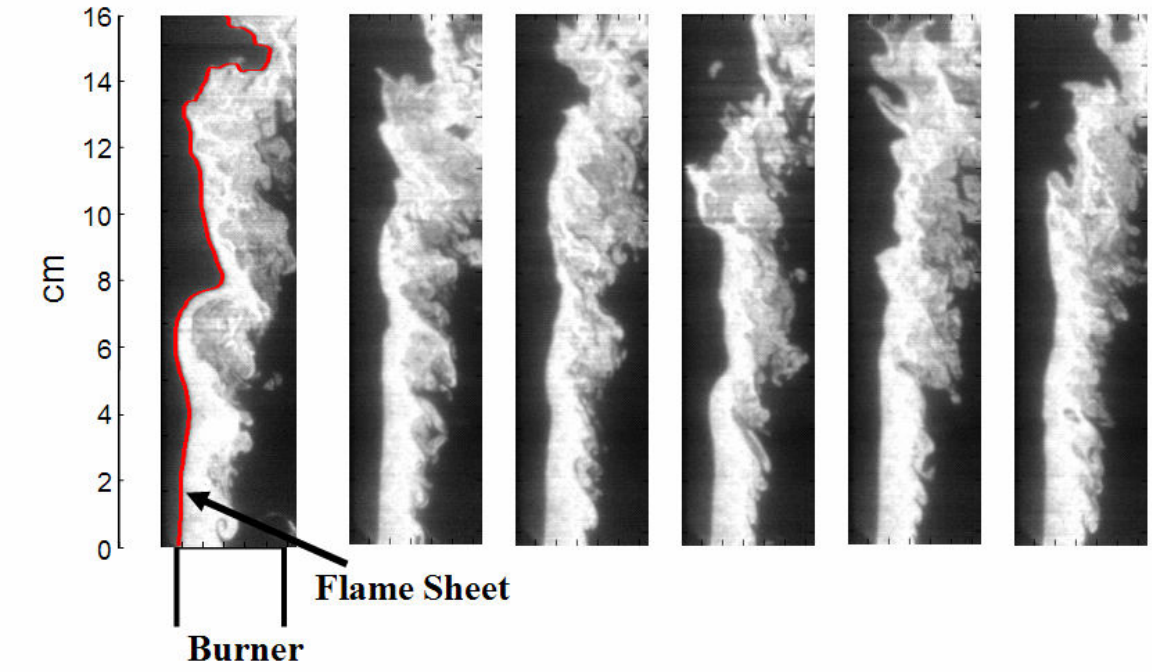

Figure 25. Typical vertical images of the slot burner flame, obtained using laser sheet illumination.

The intensity images are first converted into binary images based on an intensity threshold. Edges are tracked from the binary image and then processed for flame statistics. A histogram of the intensity of the image for a closed flame, such as shown in Figure 26(a) from an axi-symmetric flame, shows a bimodal distribution, Figure 26(b). A value close to the dip between the bright pixels (reactants) and dark pixels (products) is picked as the threshold.

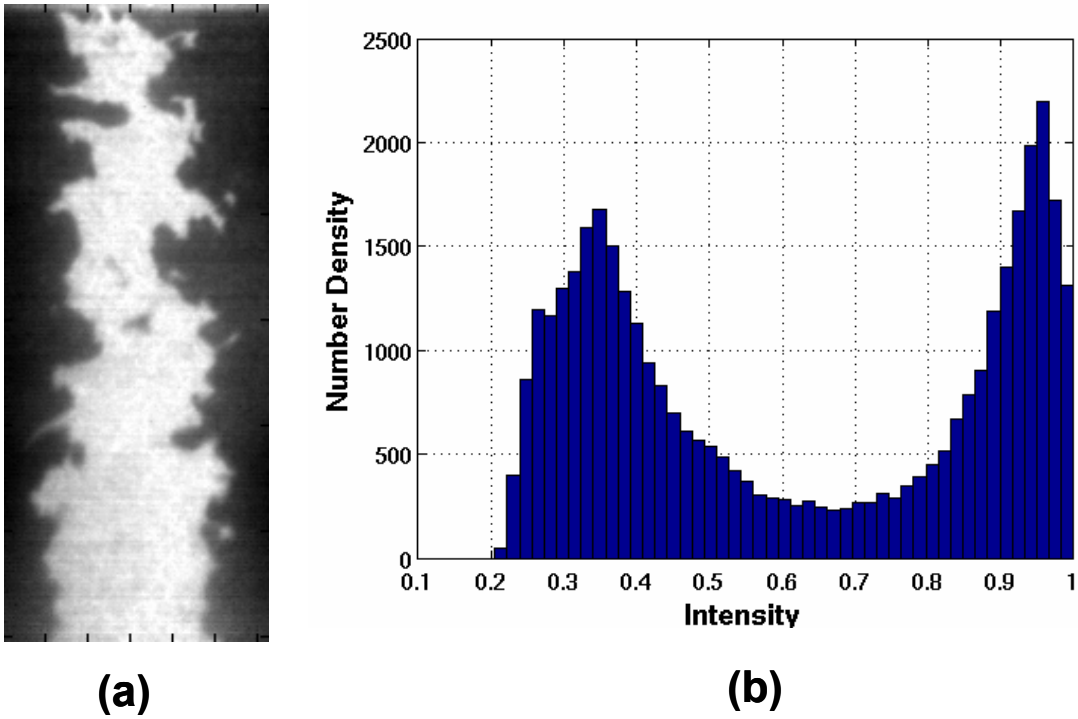

Figure 26.(a) Typical intensity image of an axi-symmetric flame cross-section (b) Histogram of the intensity distribution of the image.

Figure 27(a) shows typical intensity image of the flame from the slot burner used in this study. Figure 27(b) shows the histogram of the intensity distribution. Notice that the histogram does not have as pronounced a bimodal distribution as the axi-symmetric flame case. This is due to the fact that the intensity drops gradually on the right side where the flame is absent in the case of slot burner.

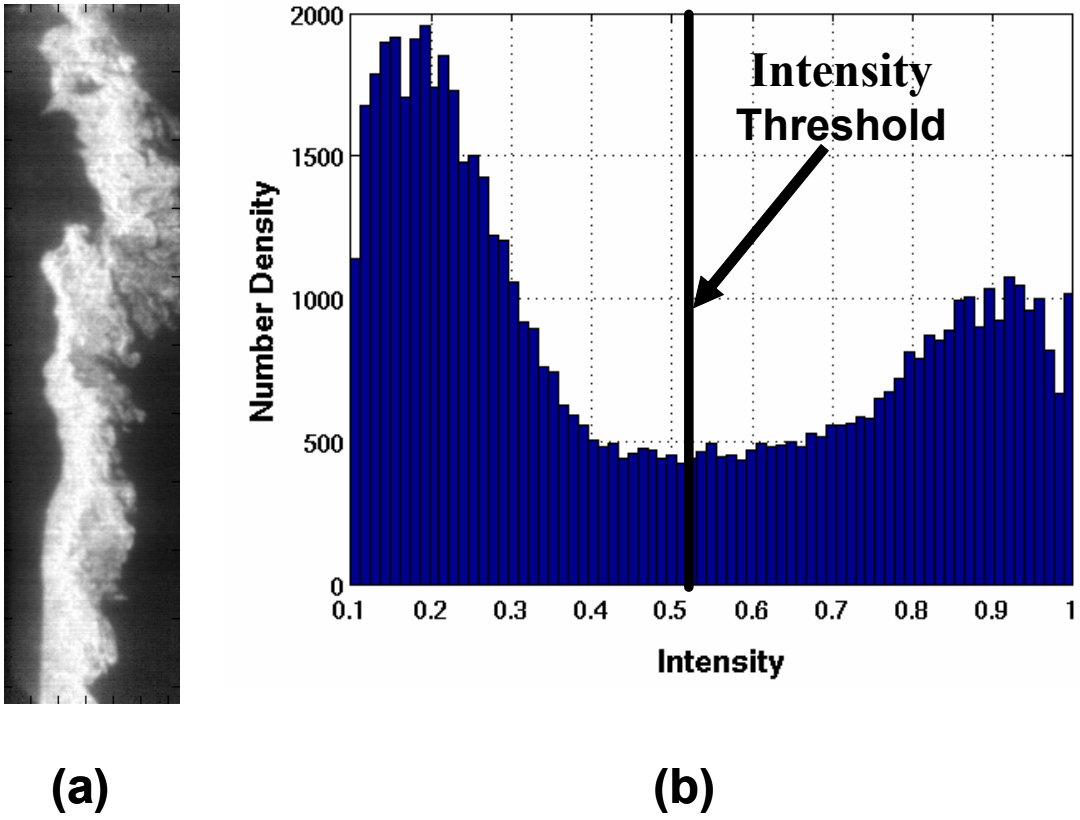

Figure 27.(a) Typical slot burner vertical flame cross-sectional image (b) Intensity distribution of the image. Intensity threshold used to convert the intensity image into binary image is also shown here.

Based on a threshold value, the intensity image, Figure 28(a), is converted to a binary image, Figure 28(b), where "1s" are the reactants and "0s" are the burnt products. Edges were tracked from the binary images. Since the flame exists only on one side of the jet, the edge was tracked from the bottom left side of the "island of 1s" and to the highest pixel belonging to this island. The edge thus determined is plotted on the original intensity image for visual comparison in Figure 28(c).

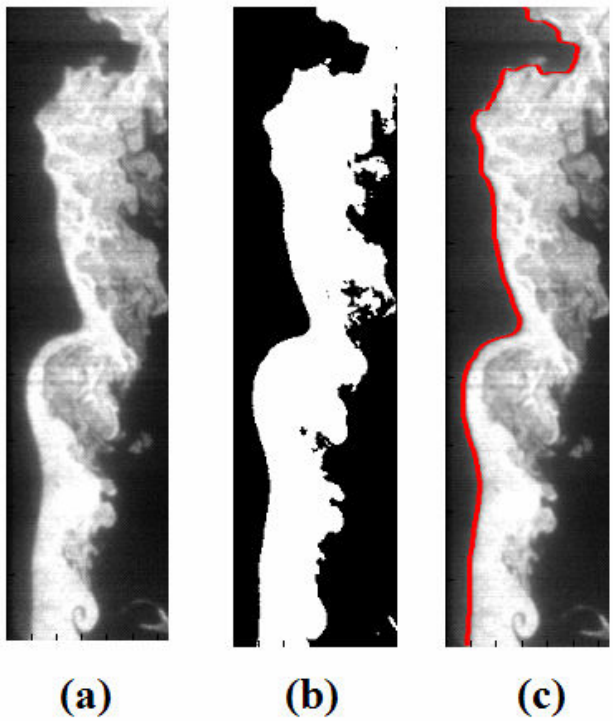

Figure 28. (a) Typical image of the vertical flame cross-section (b) Corresponding binary image (c) Edge plotted on the intensity image for comparison. Mean velocity, flame speed and turbulence intensity are 3.7 m/s, 0.17 m/s and 5.6 %, respectively.

4.2 Statistics Estimation

Once the flame edges were determined, various characteristics of the flame front were determined, as described below.

4.2.1 Flame Brush Thickness

Different definitions, based on the density gradient[48], temperature gradient, standard deviation of PDF of flame front locations[49] and progress variable[50] have been used to define flame brush thickness.

In this study, turbulent flame brush thickness is defined based on flame front location distribution. A histogram of all realizations of the axial flame front locations at each height, *y*, is compiled and the standard deviation of the distribution is defined as the flame brush thickness. This definition is further discussed in the next section.

4.2.2 Flame Orientation Angle and Curvature

Because angle and curvature statistics require differentiating the flame position, edges are first smoothed to remove high frequency digitization noise induced during the edge detection step. The edge coordinates are parameterized as $x = x(s)$ and $y = y(s)$. Then, cubic splines are fit through the edge and the corresponding first and second derivatives ($\frac{dx}{ds}, \frac{d^2x}{ds^2}$, etc) are calculated. The advantage of expressing edge coordinates parametrically is that the co-ordinates are not multi-valued and, thus, it is easy to fit a spline. If the x-axis is considered to be along the breadth of the slot and y–axis along the height of the flame, then the slope and curvature are calculated in terms of the parameter, *s*, using the following expressions:

$$\text{Slope,} \qquad \frac{dy}{dx} = \frac{\frac{dy}{ds}}{\frac{dx}{ds}} \tag{5}$$

The calculated slope at each point is then related to the flame orientation angle at that point. The sign convention for flame orientation angle, for vertical images, is shown in Figure 29. According to the sign convention, orientation angles lie between -180 to 180 degrees. For horizontal images, the methodology and the sign convention is similar,

except for the direction of flow, which will be coming out of the plane as opposed to bottom to top in the vertical images.

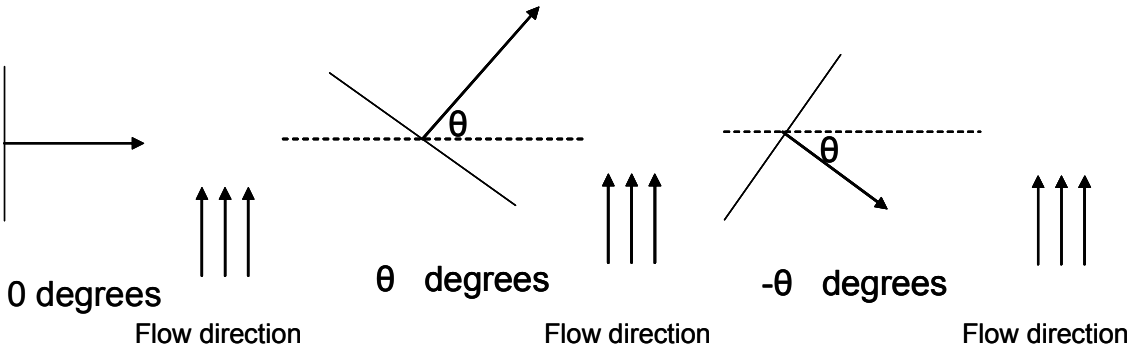

Figure 29. Sign convention for flame orientation angle for vertical images.

Similarly, curvature is calculated using the following equations:

Curvature,
$$\kappa = \frac{\frac{d^2y}{dx^2}}{\left[1+\left(\frac{dy}{dx}\right)^2\right]^{\frac{3}{2}}} \tag{6}$$

In parametric form,
$$\kappa = \frac{\frac{dx}{ds}\frac{d^2y}{ds^2} - \frac{dy}{ds}\frac{d^2x}{ds^2}}{\left[\left(\frac{dx}{ds}\right)^2+\left(\frac{dy}{ds}\right)^2\right]^{\frac{3}{2}}} \tag{7}$$

Concave flame (from reactants point of view) is assigned a negative curvature. Detailed variation of these characteristics of the flame front with height and flow variables are described in the following section.

4.3 Flame Front Characteristics Description

Before we discuss the flame front characteristics, it is useful to consider flame front characterization as it applies to the scattering problem. As explained earlier, increased flame front wrinkling (flame brush thickness) is expected to enhance the coherent to incoherent field transfer process because, the acoustic waves scattered from different parts of the flame will be further out of phase. With this point in mind, we look at a typical flame edge, shown in Figure 30.

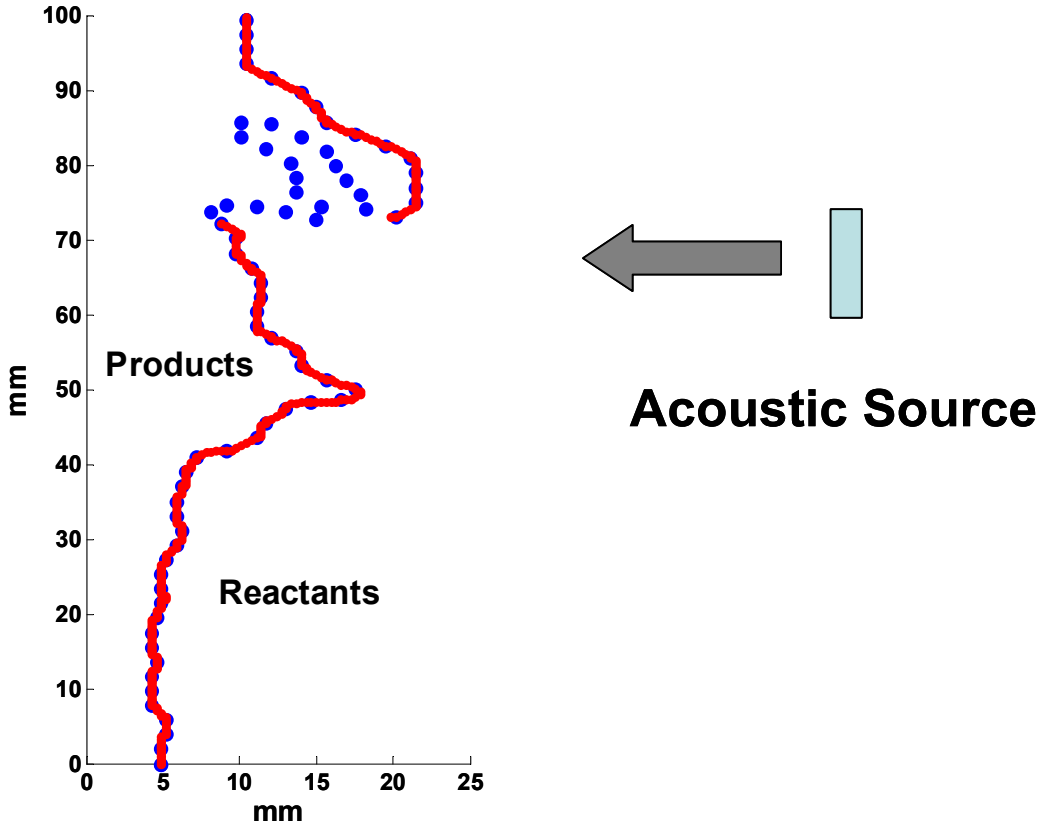

Figure 30. Schematic illustrating the multi-valued nature of the flame edge. The dotted line is the true edge. The solid line overlaid on it is the single valued edge, arrived at by excluding the parts of the flame that are not visible looking from the right side, in the direction of the arrow.

Figure 30 plots two edges: the dotted line, which is the flame edge obtained from image analysis and the overlaid solid line, which is the edge obtained by excluding the parts of the flame that are not visible looking from right side, in the direction of the arrow. The flame edge depicted in Figure 30 as dotted line is multi-valued between 70 mm – 85 mm; i.e., if a horizontal line is drawn, it will intersect the flame at more than one point between 70 mm - 85 mm. For the scattering experiments reported in this thesis, the acoustic source is positioned to the right of the flame, on the side of the reactants. Notice that from acoustic scattering point of view, the part of the convoluted flame between 70 mm - 85 mm, indicated by the dotted line, does not contribute as much to scattering of the incident acoustic wave compared to the solid line. Presumably, these parts of the flame will play an affect on the transmitted (refracted) waves. For this reason, statistics are evaluated excluding the contribution of the flame front that is shadowed, the dotted line in Figure 30. Complete flame edge (true edge) is considered during the evaluation of orientation angle and curvature along the flame front. While compiling the results from the 2000 available images to evaluate the statistics, only the contributions indicated by the solid line in Figure 30, referred to as the single valued edge, are considered. Wherever meaningful, statistics corresponding to true flame edges and the single valued edges are compared and contrasted.

Flame front images, both vertical and horizontal, are obtained for the conditions listed in Table 2. Statistics corresponding to the following conditions, which are only a cross-section of the test matrix, are analyzed to determine the effects of turbulence intensity and flow conditions (U_m and S_L):

1. U_m = 3.7 m/s and S_L = 0.23 m/s (ϕ=0.72) using multiple slits to capture the effect of turbulent velocity fluctuations, u'
2. Slit 3 (10.3% turbulence intensity) at four flow conditions

For completeness and reference, statistics are included in Appendix F for all the conditions listed in Table 2.

First, we discuss the statistics of the flame front in the vertical plane.

4.3.1 Flame Front Characterization in the Vertical Plane

The evolution of flame front statistics in the axial direction (with height) is discussed in this section. We start with flame brush thickness.

4.3.1.1 Flame Brush Thickness

Typical edges obtained from the flame images, along with PDFs of the flame front positions at three heights, 30 mm, 60 mm and 90 mm, are shown in Figure 31. Notice that the flame front takes a wider range of positions with increase in height. Flame front positions at 3 heights are quantified as PDFs for both true flame edges and single valued edges. First, with increase in height, PDFs corresponding to the "true edge" grow broader. Second, the center of the peak moves towards right, indicating that the mean flame location is inclined farther into the reactants. Comparing the true edge and the single edge cases, we see that the PDFs are identical for the height corresponding to 30 mm. The Flame front is weakly wrinkled near the burner exit and has not developed into multi-valued flame front. However, for heights corresponding to 60 and 90 mm, we see that the PDF for the single valued edge case is relatively narrow compared to the true edge.

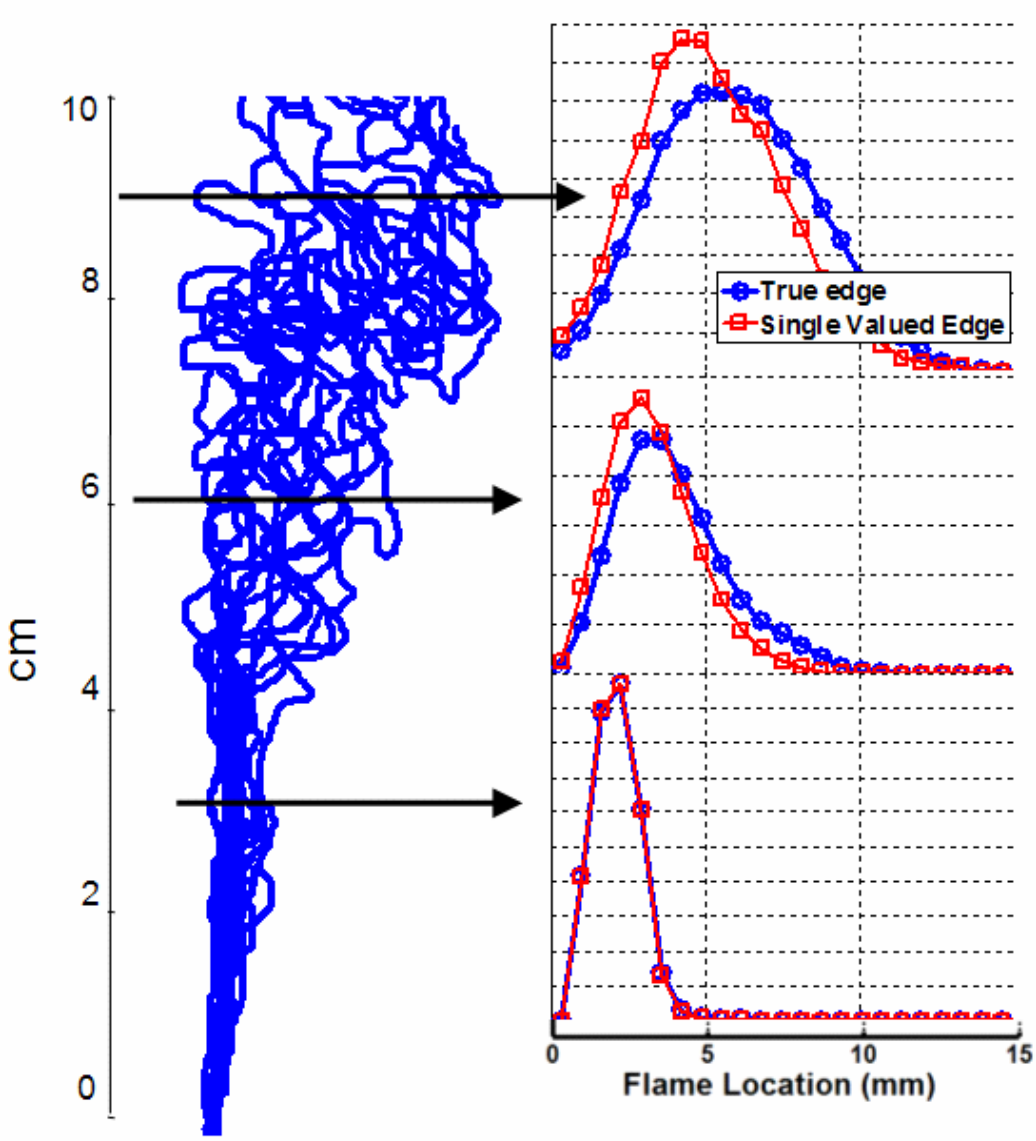

Figure 31. Several examples of flame edges obtained from image analysis along with PDFs of flame position at 3 heights: 30, 60 and 90 mm. The mean velocity, flame speed and turbulence intensity are 3.7 m/s, 0.23 m/s and 9.8%, respectively.

Flame brush thickness (σ), defined as the standard deviation of PDF illustrated in Figure 31, is plotted against height in Figure 32 for true edge case and single valued edge case. First, flame brush thickness is seen to increase with height for both cases. This observation is further discussed below. Second, at small heights, both the cases show

similar behavior. However, the difference between two cases is evident for heights greater than 40 mm.

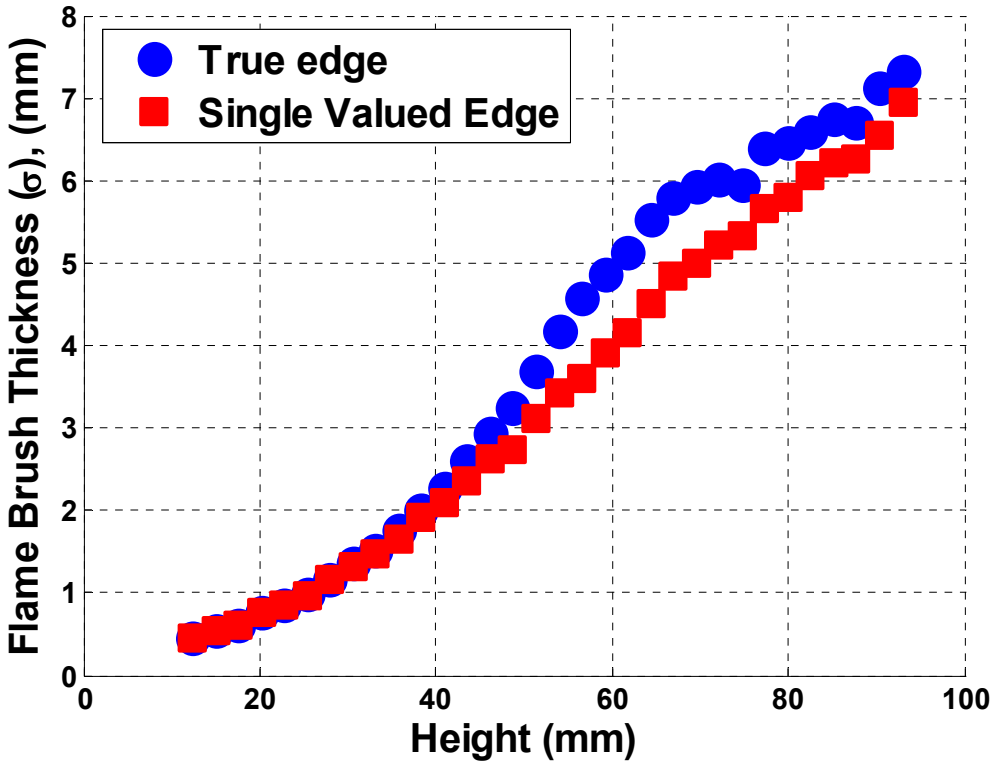

Figure 32. Flame brush thickness plotted against height for true edge and single valued edge cases. The mean velocity, flame speed and turbulence intensity are 3.7 m/s, 0.23 m/s and 9.8%, respectively.

In stationary flows, where the statistics are independent of time, the dependence of flame brush thickness with height, *y*, can be transformed to dependence on time based on Taylor's hypothesis[51]:

$$t = \frac{y}{U_m} \tag{8}$$

where U_m is the mean velocity. Thus, increase in height (time) leads to development of wrinkles, leading to increase in flame brush thickness.

Evolution of turbulent flame brush thickness based on turbulent diffusion[52,53,54,49] suggests the following dependence with time (height):

$$\sigma = \begin{cases} u't & t << \tau_L \\ \sqrt{2L_L u't} & t >> \tau_L \end{cases} \quad (9)$$

where σ, u', t, L_L and τ_L are the flame brush thickness, RMS velocity, time, integral length and integral time scales, respectively. This formulation suggest that the flame brush thickness has a linear dependence on time for small times compared to integral time scale and a square root dependence for large times compared to integral length scale. Next, the measured flame brush thickness variation with height is qualitatively compared to this formulation.

Figure 33 plots the measured flame brush thickness, based on true edges, against height for 5.6% turbulence intensity. The x-axis set to linear scale in (a) and to log scale in (b). From Figure 33(a), we see that the flame brush thickness grows in a linear fashion until approximately 60 mm from the burner exit. From Figure 33(b), where x-axis is set to log scale, we do not see any change in the slope corresponding to the expected square root dependence at large heights.

Figure 34 plots the measured flame brush thickness, based on true edges, against height for 10.4% turbulence intensity. The flame brush thickness is seen to grow linearly with height until approximately 40 mm from the burner exit. For this turbulence intensity, however, we see a distinct change in the slope, which is further illustrated in Figure 34(b), where x-axis is set to log scale. We see a distinct decrease in slope from 80 mm onwards.

This evolution behavior of flame brush thickness with height has been reported in a wide range of studies; eg, Goix *et. al.*[49] and Namazian *et. al.*[48] and reviewed in detail by Lipatnikov and Chomiak.[55]

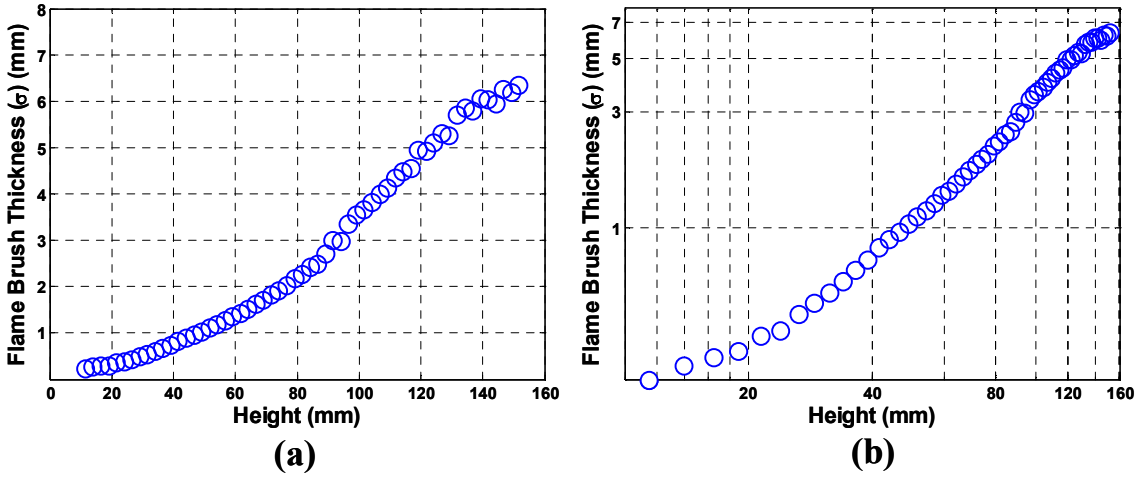

Figure 33. Flame brush thickness plotted against height for no slit configuration, 5.6 % turbulence intensity, with x-axis set to (a) Linear scale (b) Log scale. Mean velocity and flame speed are 3.7 m/s and 0.17 m/s, respectively.

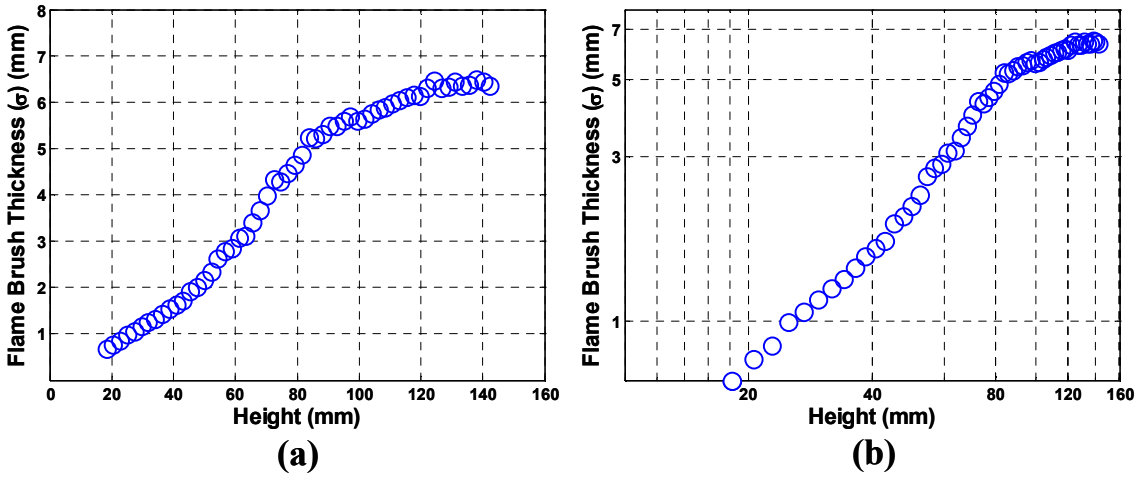

Figure 34 Flame brush thickness plotted against height for 3 mm slit configuration, 10.4% turbulence intensity, with x-axis set to (a) Linear scale (b) Log scale. Mean velocity and flame speed are 3.7 m/s and 0.17 m/s, respectively.

Figure 35 plots the flame brush thickness (σ), based on single valued edges, against height for multiple turbulence intensities for 3.7 m/s mean velocity and 0.23 m/s flame speed. It can be seen that increases in turbulence intensity leads to increases in the flame brush thickness. This is expected because the larger velocity fluctuations lead to higher degree of flame front wrinkling which results in increased flame brush thickness. Increase in flame brush thickness has been observed, among other studies, in the aforementioned study by Namazian *et. al.*[48].

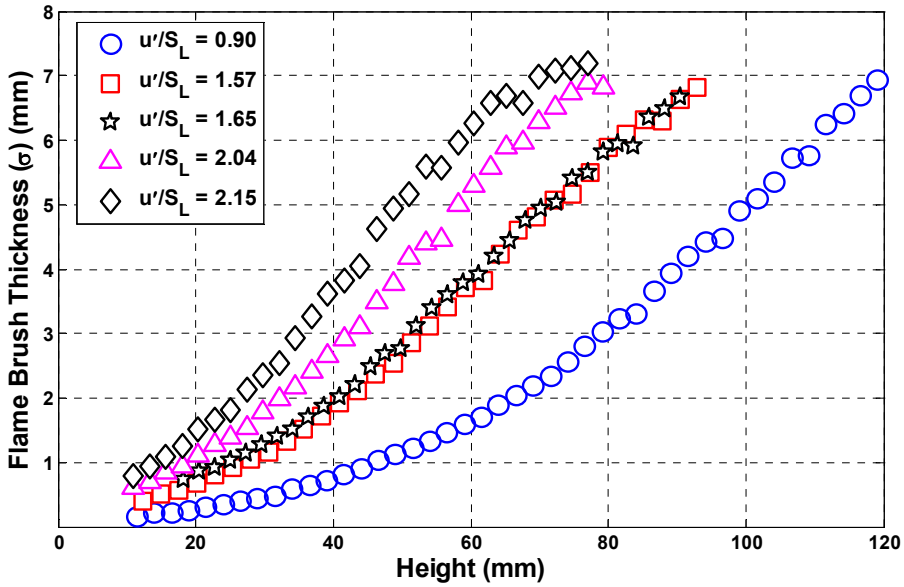

Figure 35. Flame brush thickness, based on single valued edges, plotted against height for multiple turbulence intensities for U_m=3.7 m/s and S_L = 0.23 m/s.

Figure 36 plots the flame brush thickness, based on single valued edges, against height for multiple flow conditions for the 10.3% turbulence intensity case. It can be seen that the flame brush thickness increases with flame speed. From the same figure, also notice that for a given flame speed, the mean velocity has a negligible effect on the flame brush thickness. This is apparently because of two opposing effects: increase in velocity fluctuations with increase in mean velocity,

$$u' \propto U_m \tag{10}$$

and decrease in time available for flame evolution at a given height,

$$t \propto \frac{1}{U_m} \tag{11}$$

Flame brush thickness, (σ), which is mainly controlled by the turbulent diffusion law[52,53,54,49], as discussed above, can be expressed as[55],

$$\sigma \propto (u't)^n \propto \left(U_m . \frac{1}{U_m} \right)^n \propto const \tag{12}$$

which is independent of the mean velocity.

Independence of flame brush thickness with mean velocity was reported by Namazian et. al.[48].

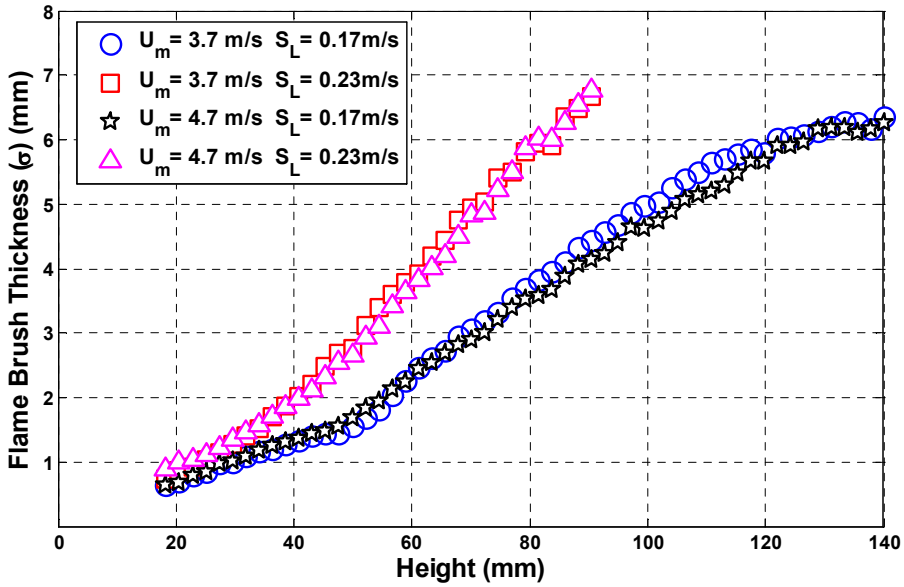

Figure 36. Flame brush thickness, based on single valued edges, plotted against height for four flow conditions for the 10.3% turbulence intensity case.

4.3.1.2 Orientation Angle

Figure 37 plots the PDFs of flame front orientation angle in the vertical plane (θ_v) at 3 heights, 30, 60 and 90 mm from burner exit, compiled for both true edge and single valued edge cases. The mean velocity, flame speed and turbulence intensity are 3.7 m/s, 0.23 m/s and 9.8%, respectively. It is seen that the PDFs of flame orientation angle in the vertical plane broaden with height, as there is only weak fluctuation of the flame front near the burner exit. For the true edge case, at 60 and 90 mm, the flame orientation angles extend from -180^o to 180^o. This trend of broadening in PDFs of orientation angle with height has been reported in previous studies.[47,30,31] From the same figure, for the single valued edge case, we see that the range of orientation angles increase with height. However, angles are limited to -90^o to 90^o for this case. From the orientation angle sign convention, see Figure 29, we see that the parts of the flame that are excluded have orientation angles between -90^o to -180^o and 90^o to 180^o. This difference between the true and single value edges cases is further quantified in Figure 38, where the standard deviation of the flame orientation angles is plotted against height for the two cases. It can be seen that the standard deviation increases with height and that the single edge case deviates from the true edge case from 30 mm height.

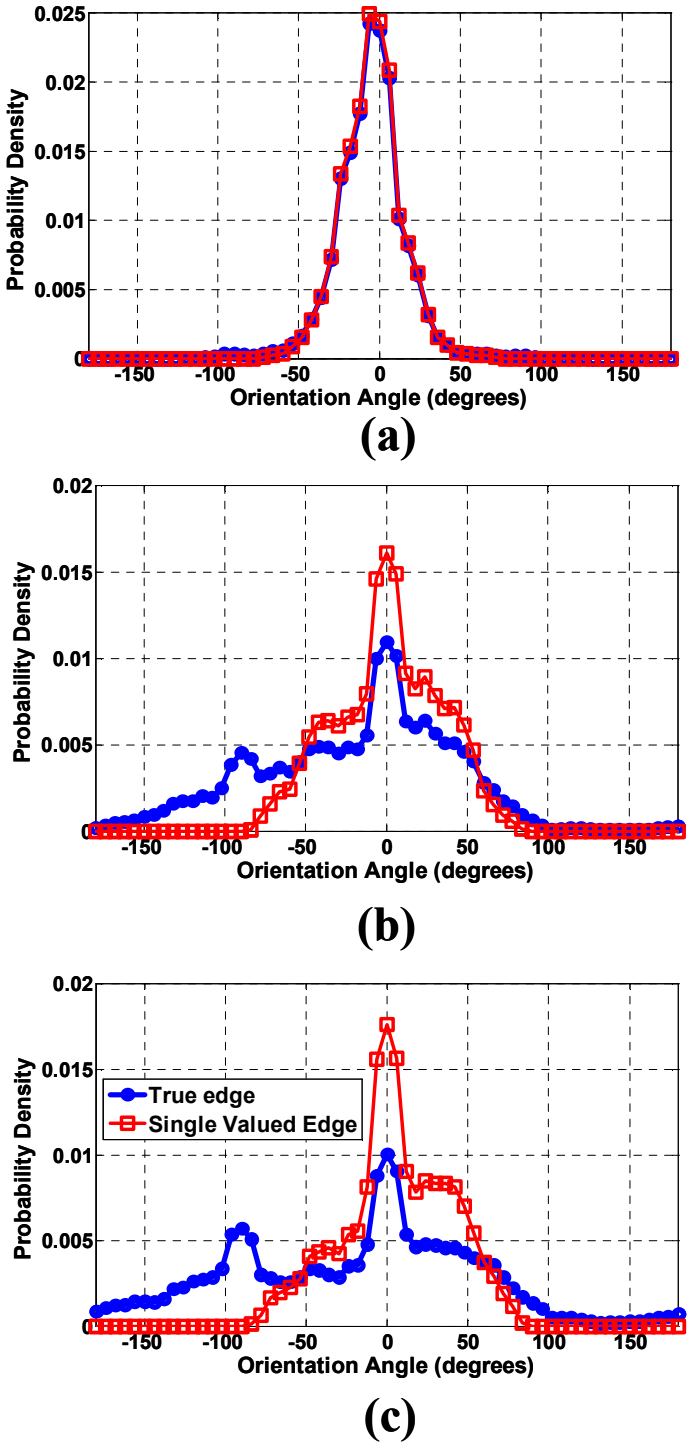

Figure 37. Probability distribution of θ_v at 3 heights (a) 30 mm (b) 60 mm and (c) 90 mm from the burner exit. Circles and squares correspond to the true edge and single valued edge cases, respectively. The mean velocity, flame speed and turbulence intensity are 3.7 m/s, 0.23 m/s and 9.8%, respectively.

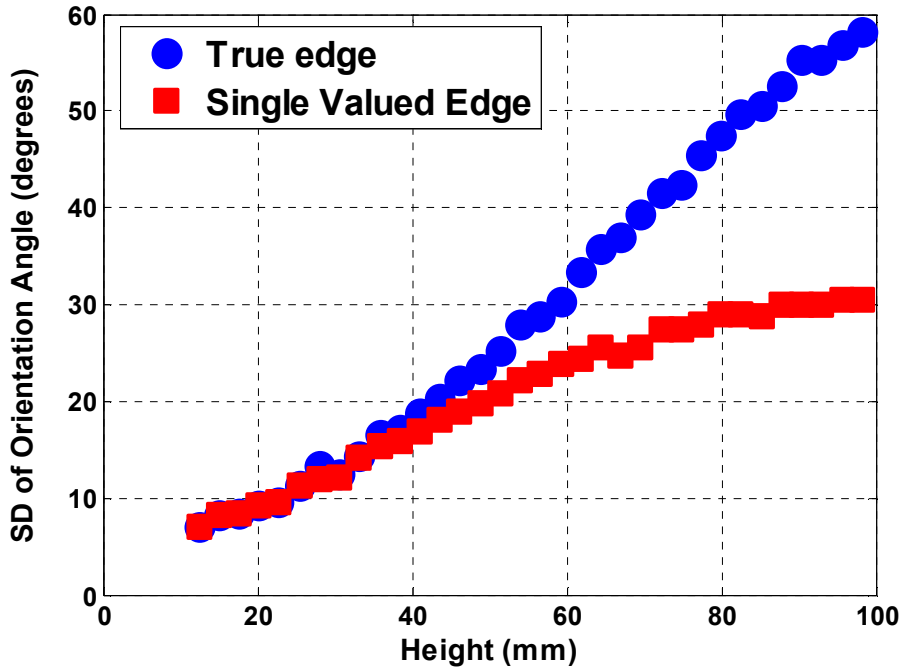

Figure 38. Standard deviation of θ_v plotted against height for the true edge and single valued edge cases. The mean velocity, flame speed and turbulence intensity are 3.7 m/s, 0.23 m/s and 9.8%, respectively.

Next, the dependence of orientation angle (θ_v) distribution on flow variables is discussed.

Two mean angles are defined to describe the flame orientation angle distribution: mean of all positive angles and mean of all negative angles. Figure 39(a) plots such angles against height for the 10.3% turbulence intensity condition for the single valued edges case. Both means of positive and negative angles increase with height. As pointed out above, the flame wrinkle structures evolve spatially and this leads to a wider range of orientation angles. This is quantified further in Figure 39(b) as standard deviation of all angles.

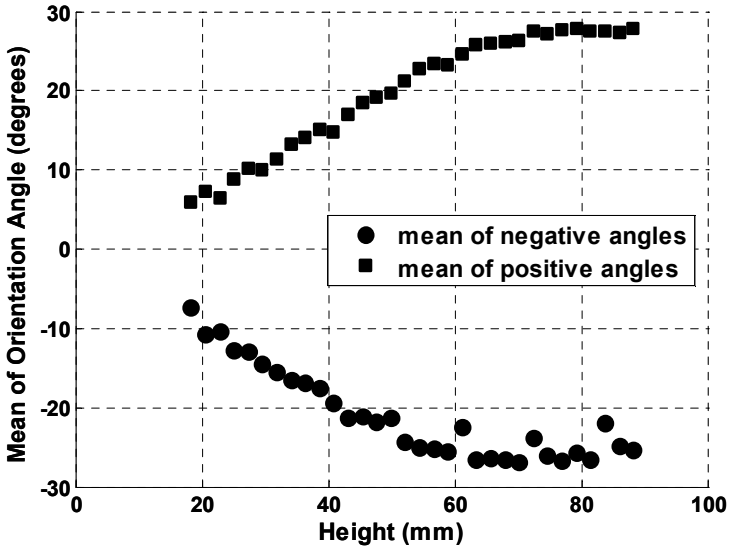

(a)

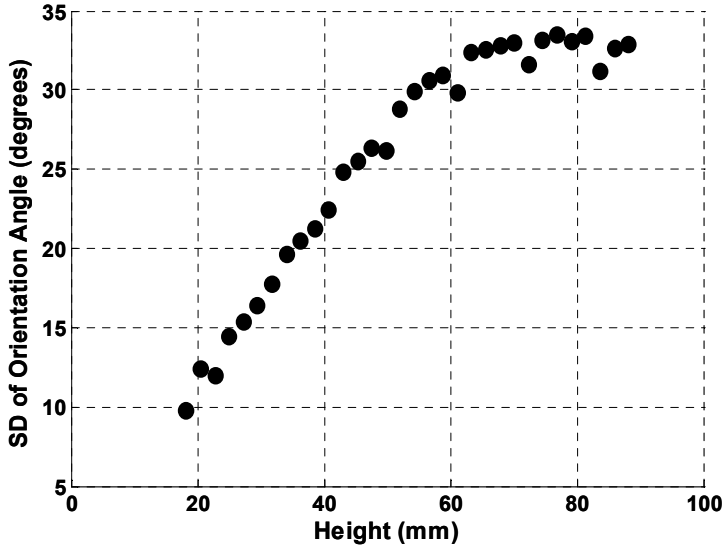

(b)

Figure 39. (a) Mean of positive and negative orientation angles, measured in the vertical plane, plotted against height (b) Standard deviation of all orientation angles plotted against height for the same case. The mean velocity, flame speed and turbulence intensity are 3.7 m/s, 0.23 m/s and 10.3%, respectively.

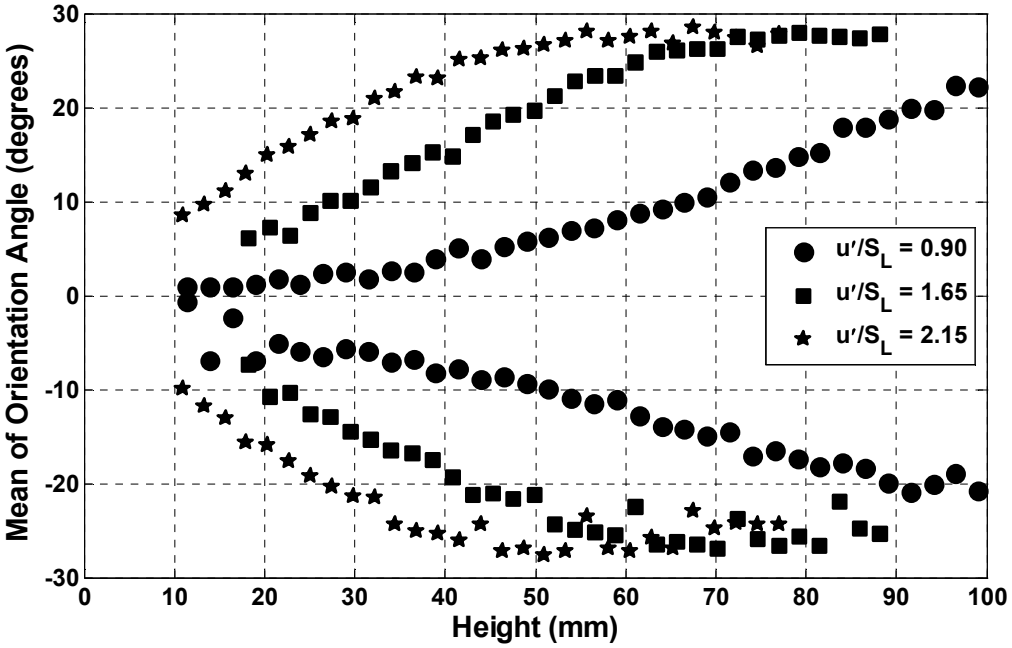

Figure 40. Mean of positive and negative orientation angles, measured in the vertical plane, plotted against height for three turbulence intensities (5.6%, 10.3% and 13.4%) for $U_m = 3.7$ m/s and $S_L = 0.23$ m/s.

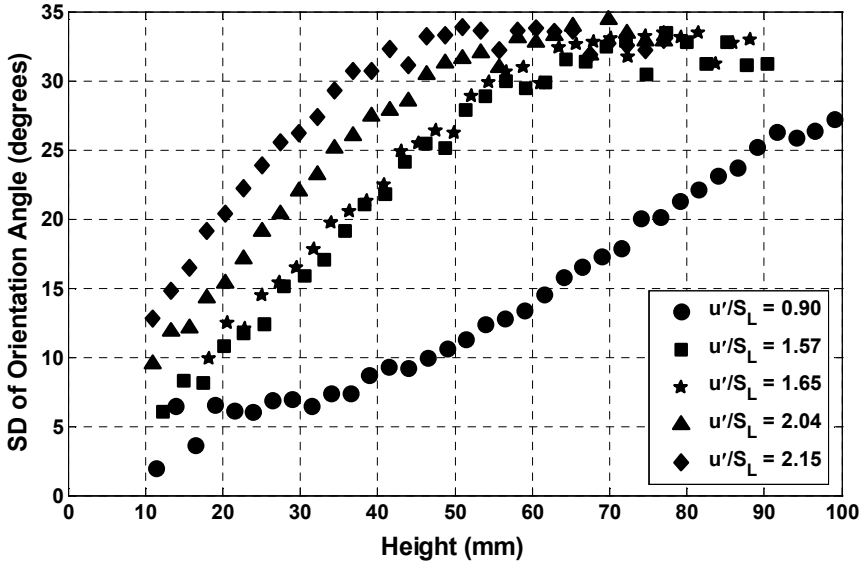

Figure 41. Standard deviation of orientation angle distribution, measured in the vertical plane, plotted against height for five turbulence intensities for $U_m = 3.7$ m/s and $S_L = 0.23$ m/s.

Figure 40 plots the means of angles for three different turbulence intensities. With increase in turbulence intensity, the mean of angles increases because of the expected increase in randomness of the orientation angles. This variation is further quantified in the form of standard deviation for all five turbulence intensities in Figure 41. Similar observations, increase in standard deviation of orientation angle distribution with u'/S_L, have been reported by Lee *et. al.*[30], where experiments were performed on a turbulent premixed Propane/air flames.

The dependence of orientation angle distribution, based on single valued edges, on mean velocity and flame speed is illustrated in Figure 42, where standard deviation of all angles is plotted against height for four flow conditions for the 10.3% turbulence intensity case. The standard deviation increases with flame speed for a fixed mean velocity and is independent of mean velocity for a fixed flame speed. The observed independence with mean velocity is expected because of the competing effects of the increase in turbulent velocity fluctuations and time available for flame evolution. These two effects were discussed in detail in the context of flame brush thickness.

In chapter 3, where the measured 1-D turbulent kinetic energy spectra were presented, a sharp peak was reported in the spectra at approximately 1000 Hz for the 10.3% turbulence intensity case. It was pointed out that the peak was dependent on the mean velocity: it was present for the 3.1 m/s mean velocity and was absent for the 4.4 m/s. Acoustic measurements performed simultaneously with the velocity measurements showed a tone at 1000 Hz for the 3.1 m/s case. No discernable peak could be observed for the 4.4 m/s case.

A tone similar to the 3.1 m/s case was observed for 3.7 m/s case during the image acquisition. No such tone was observed for the 4.7 m/s case. The flame statistics for both the velocities are presented in Figure 42. Notice that the flame front statistics, both the orientation angle and the flame brush thickness (from previous section), are seen to be independent of mean velocity. This suggests that the influence of the velocity oscillations corresponding to the tone is negligible on the flame front statistics.

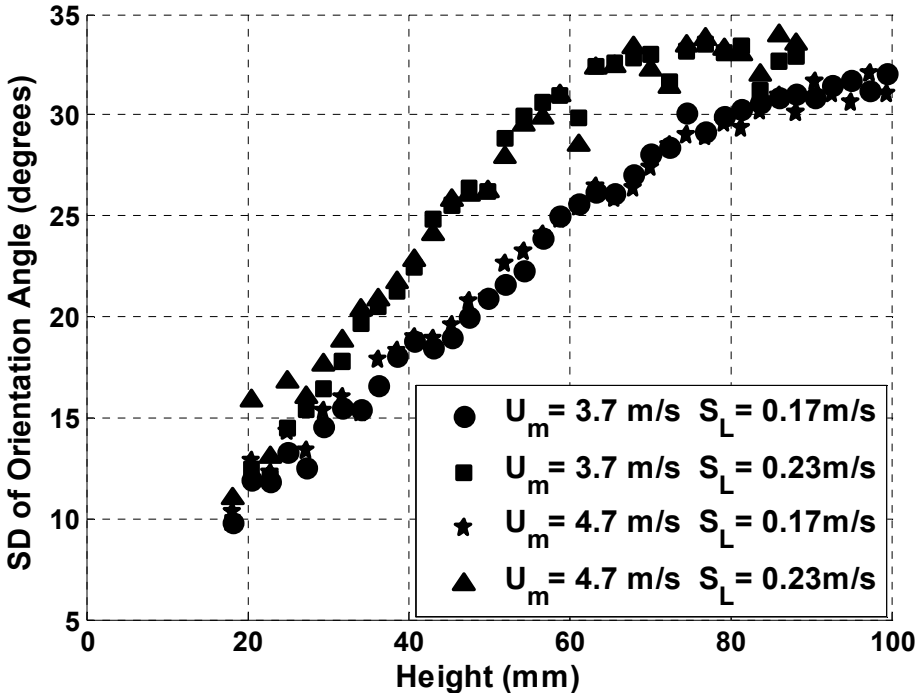

Figure 42. Standard deviation of all orientation angles, measured in the vertical plane, plotted against height for 4 flow conditions for 10.3% turbulence intensity case.

4.3.1.3 Curvature

Figure 43 plots the PDFs of flame front curvature at 3 heights, 30, 60 and 90 mm from burner exit, compiled for both true edge and single valued edge cases. The mean velocity, flame speed and turbulence intensity are 3.7 m/s, 0.23 m/s and 9.8%,

respectively. PDFs of the flame front curvature grow marginally broader with increase in height. This is expected because of the increased flame front wrinkling with height. Notice that there is no significant difference observed in PDFs of the true edge case and the single valued edge case. Curvature calculation involves second derivative of the flame edge and, thus, one would not expect the flame location itself to have major influence on the curvature distribution. Also, the PDFs of curvature distribution are nearly symmetric about zero mean, with a small decaying tail towards the negative curvatures at 60 and 90 mm. This observation is different to the study reported on axi-symmetric turbulent flames by Lee *et. al.*[47], where a systematic shift in the PDF shape with height was observed. They reported that the PDFs of curvature shifted to right (positive curvatures), with a long tail to the left. They suggested that the cusp formation towards the tip, along with the mean flame orientation with mean flow as reasons for the asymmetry. In the current study, the flame produced by the slot burner is not a closed flame and thus would result in reduced cusp formation near the tip. Essentially, in this configuration, the slot burner produces only "half" the flame. Symmetric PDFs of curvature have been reported for the case of premixed turbulent flames propagating into a nearly isotropic turbulent flow field by Lee *et. al.*[31].

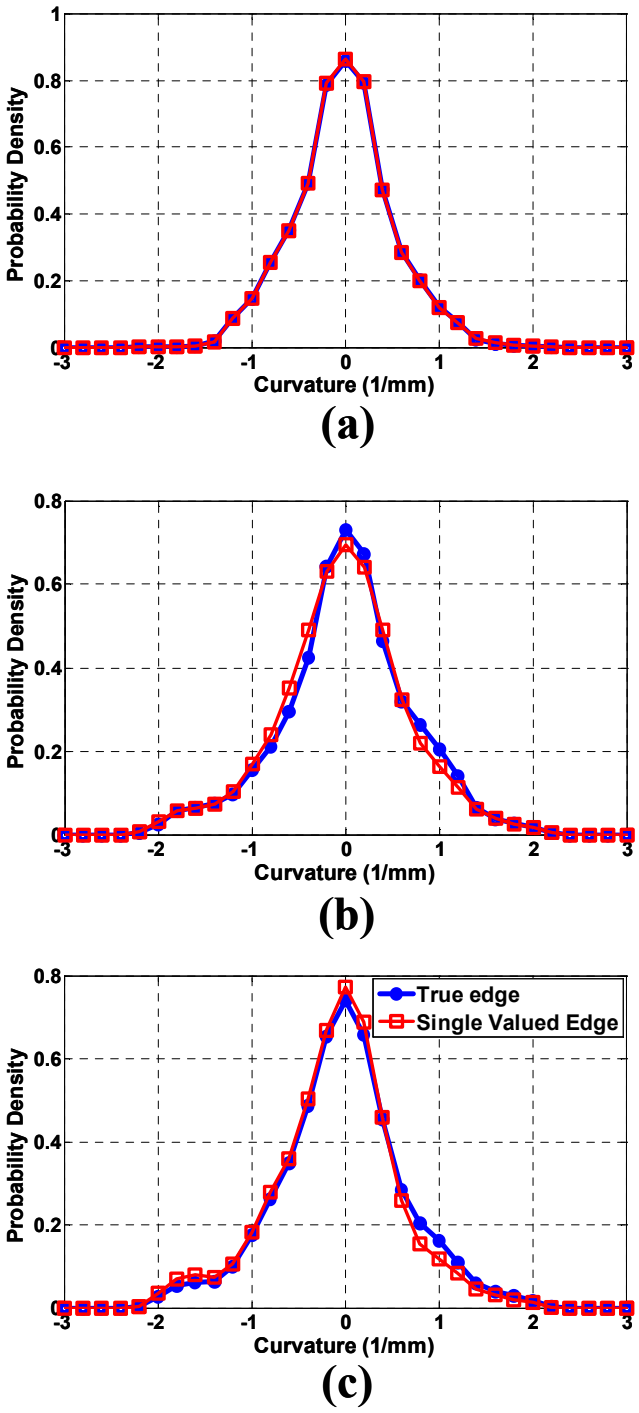

Figure 43. PDFs of flame front curvature measured in the vertical plane at 3 heights (a) 30 mm (b) 60 mm and (c) 90 mm from the burner exit. Circles and squares correspond to the true edge and single valued edge cases, respectively. The mean velocity, flame speed and turbulence intensity are 3.7 m/s, 0.23 m/s and 9.8%, respectively.

Figure 44(a) plots mean of positive and negative curvatures against height for the 10.3% turbulence intensity case. It can be seen that the mean of the curvatures increases with height. Figure 44(b) plots the standard deviation of all curvatures against height for the same case. As expected, standard deviation increases with height.

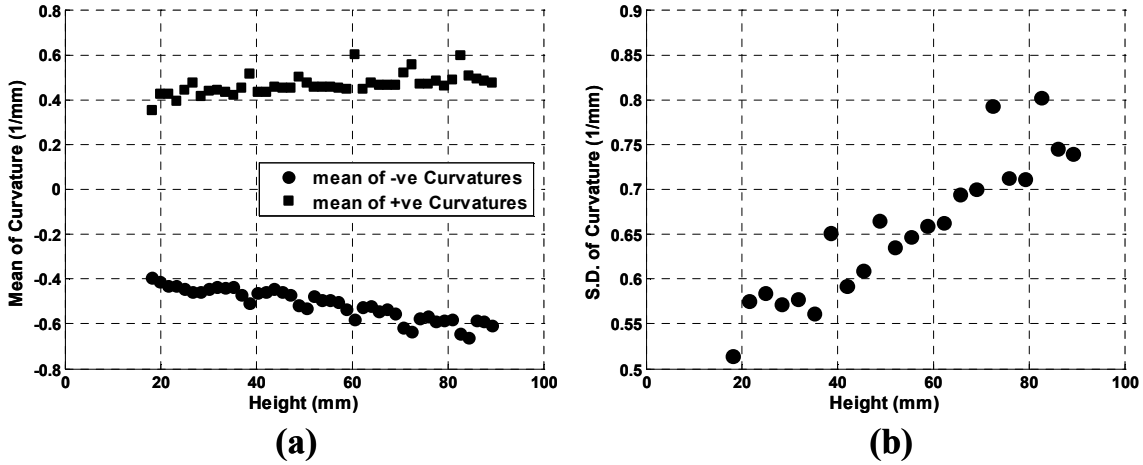

Figure 44.(a) Mean of curvatures, measured in the vertical plane, plotted against height (b) Standard deviation of all curvatures plotted against height for the same case. Mean velocity, flame speed and turbulence intensity are 3.7 m/s, 0.23 m/s and 10.3%, respectively.

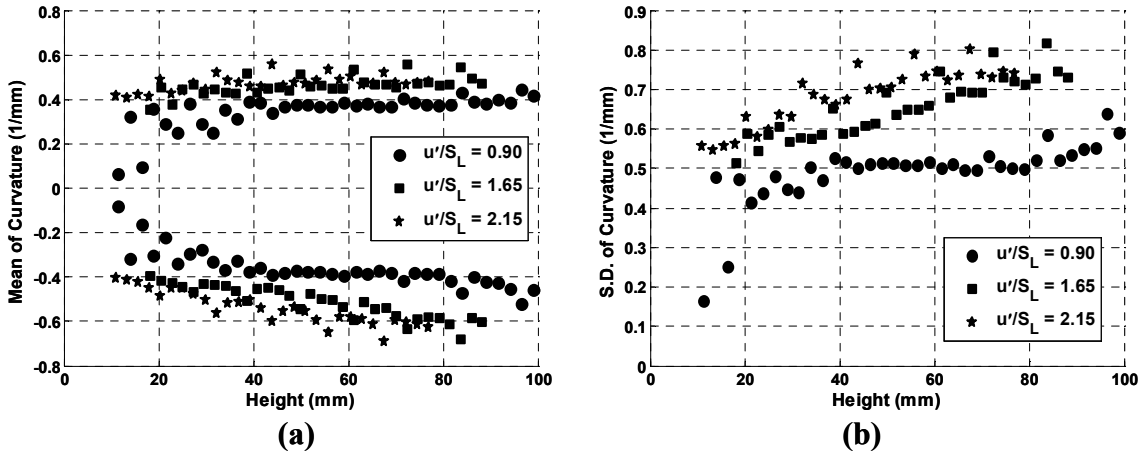

Figure 45. (a) Mean of curvatures, measured in the vertical plane, plotted against height for three turbulence intensities (5.6%, 10.3% and 13.4%) (b) Standard deviation of all curvatures plotted against height for the same conditions. Mean velocity and flame speed are 3.7 m/s and 0.23 m/s, respectively.

Figure 45(a) plots the mean of curvatures for three turbulence intensities (5.6%, 10.3% and 13.4%) based on single valued edges. Figure 45(b) plots the standard deviation with height for the same three cases. As expected, the plots show that the mean and standard deviation of curvature increase with turbulence intensity. Notice in Figure 45(a) that for the lowest turbulence case, both the means of curvature are close to zero while the higher turbulence intensity cases show significant curvature even at small heights. This is because of the enhanced flame wrinkling caused by higher turbulence even close to the burner exit. Increase in mean and standard deviation of curvatures with turbulence intensity, have been reported by Lee and coworkers[30,31] and Haq *et. al.*[56].

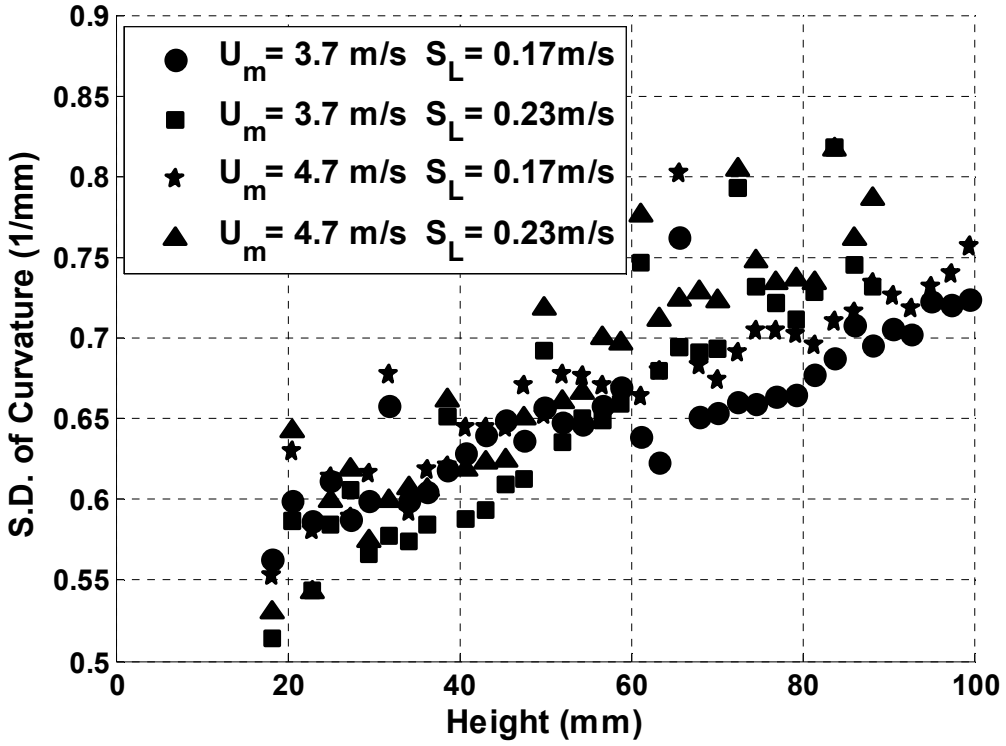

Figure 46. Standard deviation of all curvatures, measured in the vertical plane, plotted against height for 4 flow conditions for the 10.3% turbulence intensity case.

Figure 46 plots the standard deviation of all curvatures plotted against height for four flow conditions for the 10.3% turbulence intensity. There is significant scatter in the data. Despite this, we can see that the squares and the triangles (same flame speed) have similar values compared to the squares and the circles (same mean velocity), particularly for heights greater than 60 mm.

4.3.2 Flame Front Characterization in the Horizontal Plane

Statistics in the horizontal plane were estimated using the same schemes as that of the vertical plane. Distinction is made between true flame edges and the single valued edge. First, comparisons, similar to vertical cross-sectional images, are made between the true edges and single valued edges. Then statistics are presented for the single valued edges. Where ever possible, the trends are compared to statistics in the vertical plane. We start with the flame brush thickness.

4.3.2.1 Flame Brush Thickness

Figure 47 plots the flame brush thickness along the width of the burner for two heights: 51 mm and 102 mm for true edge and single valued edge cases. First, we see that the flame brush thickness varies along the width of the burner, particularly towards the ends. This behavior is expected because of the increased velocity fluctuations towards either end of the burner; see Figure 21 where RMS velocity is plotted along the burner width. In addition, similar to vertical images, we see an increase in flame brush thickness with height. Comparing the true edge cases and single valued edge cases at 51 mm

height, we do not see any difference between the two cases. At 102 mm, we see that the flame brush thickness is lower for the single edge case.

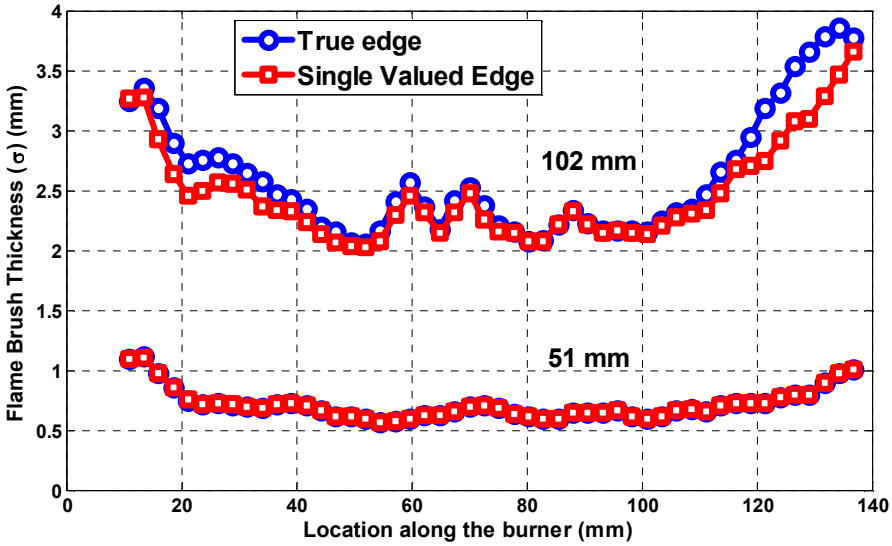

Figure 47. Flame brush thickness, obtained from horizontal images, plotted along the burner width for two heights: 51 mm and 102 mm for true edges and single valued edges. The mean velocity, flame speed and turbulence intensity are 3.7 m/s, 0.17 m/s and 5.6%, respectively.

Figure 48 plots the measured flame brush thickness, based on single valued edges, along the width of the burner for multiple heights. Flame brush thickness is seen to increase with height. At a fixed height, we expect the flame brush thickness measured in the horizontal plane to be the same as that from the vertical plane. For that reason, flame brush thickness results from both vertical and horizontal images are compared in Figure 49.

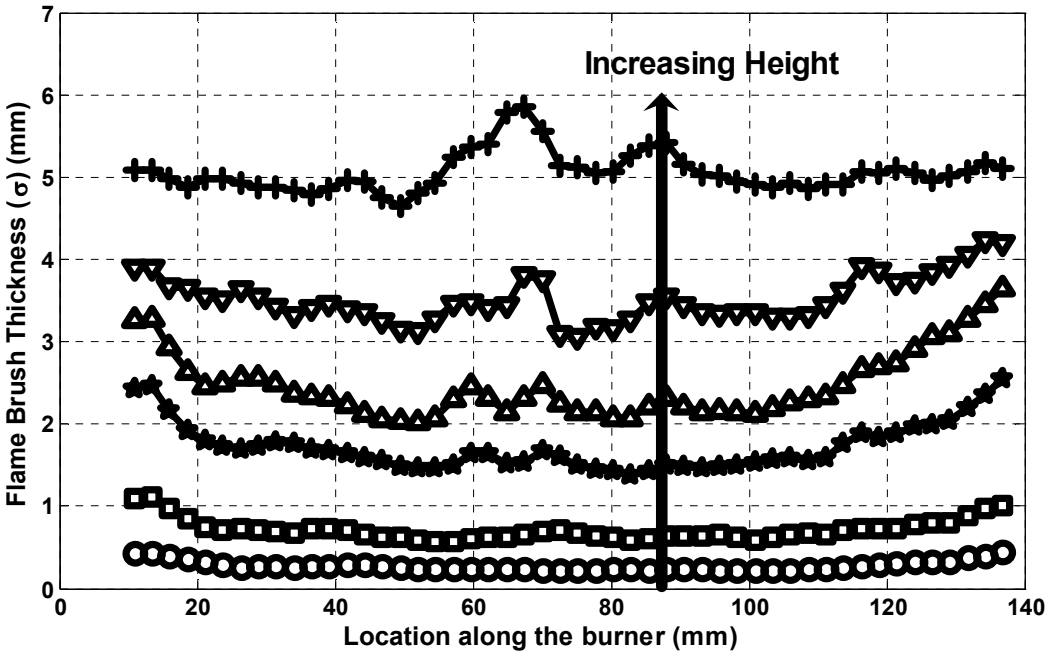

Figure 48. Flame brush thickness, obtained from horizontal images, plotted along the burner width for multiple heights varying from 25 mm to 150 mm insteps of 25 mm. The mean velocity, flame speed and turbulence intensity are 3.7 m/s, 0.17 m/s and 5.6%, respectively.

Figure 49 plots the flame brush thickness against height for both horizontal and vertical images. The mean velocity, flame speed and turbulence intensity are 3.7 m/s, 0.17 m/s and 5.6%, respectively. We see a good agreement, within 6%, between the estimates from the horizontal and vertical images.

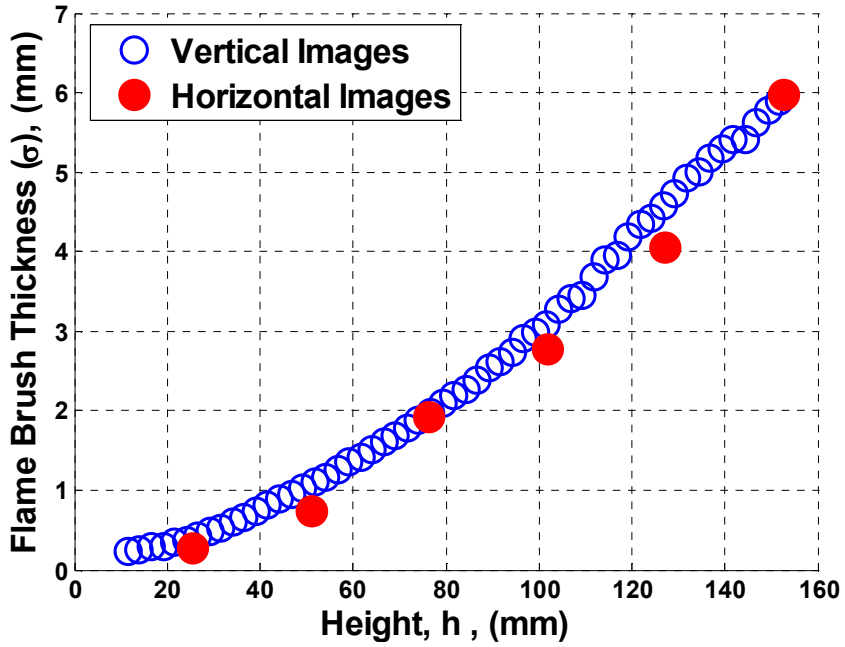

Figure 49. Measured flame brush thickness plotted against height for comparison between vertical and horizontal cross-sectional images. The mean velocity, flame speed and turbulence intensity are 3.7 m/s, 0.17 m/s and 5.6%, respectively.

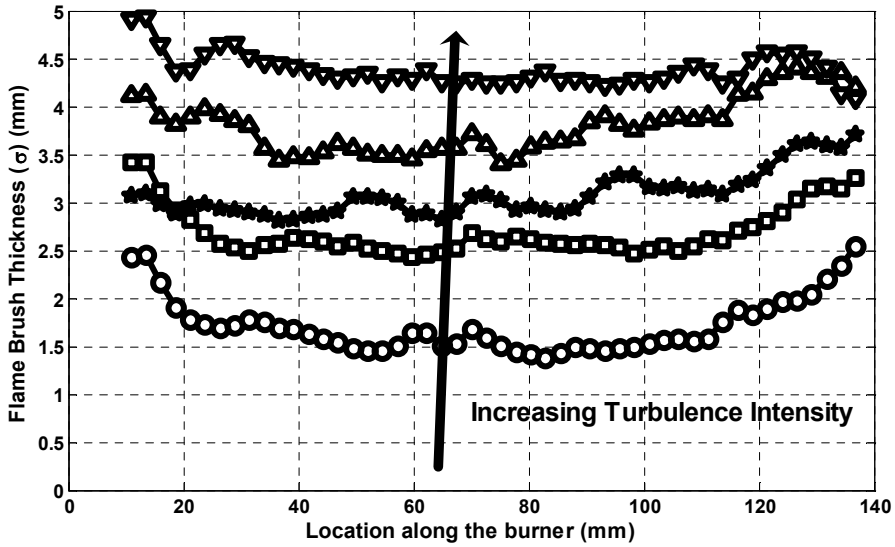

Figure 50. Flame brush thickness, obtained from horizontal images, measured at 51 mm from the burner exit, plotted along the burner width for 5 turbulence intensities. The mean velocity and flame speed are 3.7 m/s and 0.17 m/s, respectively.

Figure 50 plots the flame brush thickness along the burner width for multiple turbulence intensities at a height corresponding to 51 mm from the burner exit. Mean velocity and flame speed are 3.7 m/s and 0.17 m/s, respectively. As expected, the flame brush thickness increases with turbulence intensity.

4.3.2.2 Flame Orientation Angle

Flame orientation angle in the horizontal plane (θ_H) distribution is determined from the horizontal cross-sectional images.

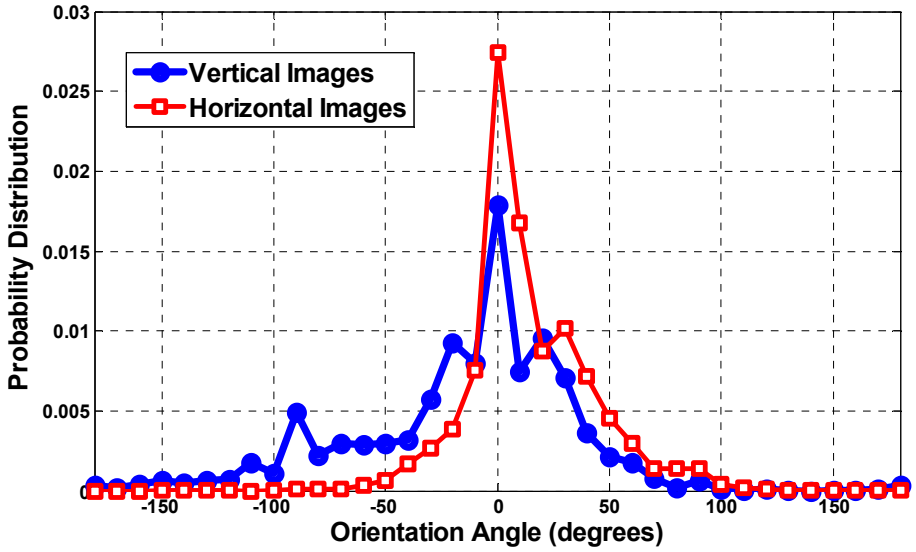

Figure 51. PDFs of orientation angle in the vertical plane and the horizontal plane, measured at 76 mm from the burner exit. Mean velocity, flame speed, turbulence intensity and u'/S_L are 3.7 m/s, 0.23 m/s, 5.6 % and 0.9, respectively.

Figure 51 plots the PDF of orientation angle for true edge case for both vertical plane, θ_v, and horizontal plane, θ_H, measured at 76 mm from the burner exit. The θ_v distribution is seen to be different from the θ_H distribution. Bingham *et. al.*[57] reported orientation angle measurements in both the vertical plane (measured with respect to the

mean flame normal) and horizontal planes for V-shaped turbulent flames (u'/S_L varying from 0.6-1.8). They reported that the θ_V distribution is quite different from the θ_H distribution. A highly peaked distribution was observed for θ_V, while a uniform distribution was seen for θ_H. Lee *et. al.*[47] reported differences between θ_V and θ_H distributions for an axi-symmetric premixed turbulent flame.

Figure 52 plots the standard deviation of θ_H distribution for single valued edges case for multiple heights. The standard deviation is seen to increase with height, as expected.

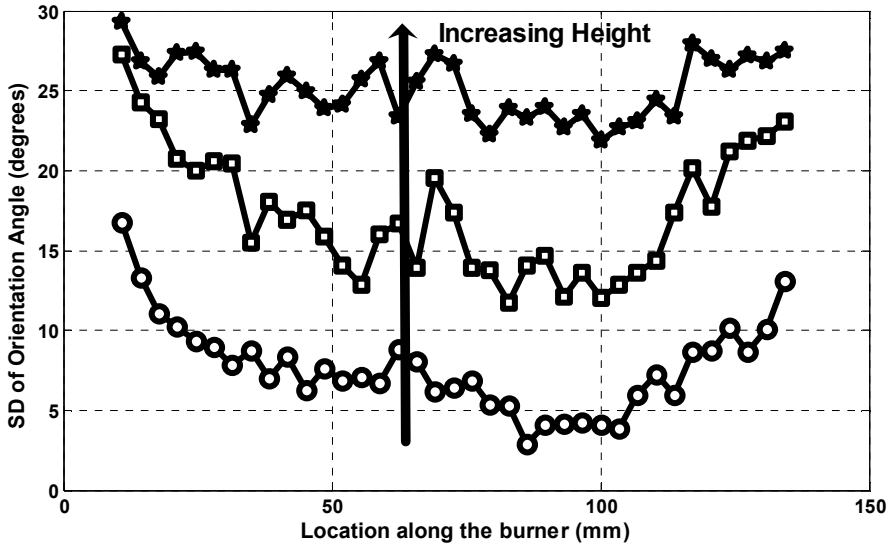

Figure 52 Standard deviation of θ_H distribution plotted along the burner width for three heights: 25 mm, 76 mm and 127 mm. The mean velocity, flame speed and turbulence intensity are 3.7 m/s, 0.17 m/s and 5.6%, respectively.

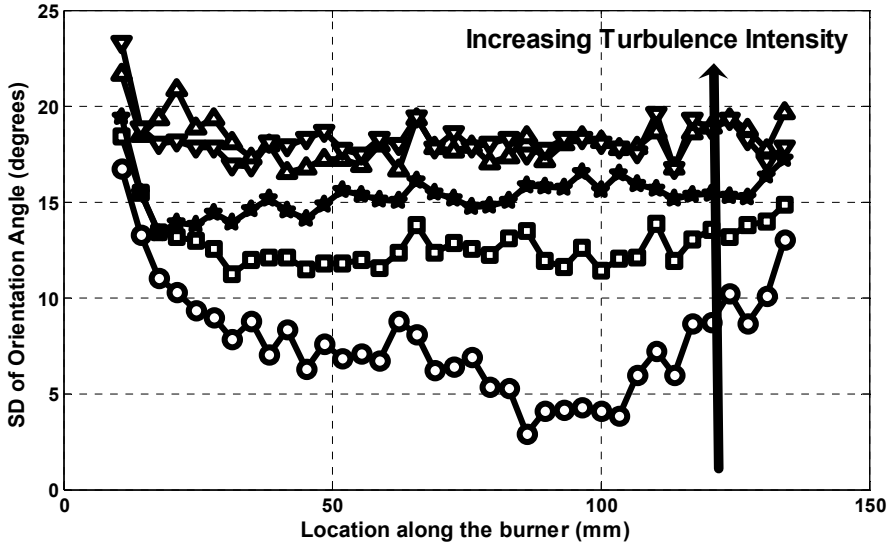

Figure 53. Standard deviation of θ_H distribution, measured at 25 mm height, plotted along the burner width for multiple turbulence intensities: 5.6-13.4%. The mean velocity and flame speed are 3.7 m/s and 0.17 m/s, respectively.

Figure 53 plots the standard deviation of θ_H distributions along the burner width for single valued edges for multiple turbulence intensities, measured at a height of 25 mm from the burner exit. The standard deviation of θ_H distribution is seen to increase with turbulence intensity.

4.3.2.3 Curvature

Standard deviation of curvature is plotted along the burner width for multiple heights in Figure 54. The mean velocity, flame speed and turbulence intensity are 3.7 m/s, 0.17 m/s and 5.6%, respectively. Despite the variation along the width of the burner, the standard deviation of curvature is seen to increase with height.

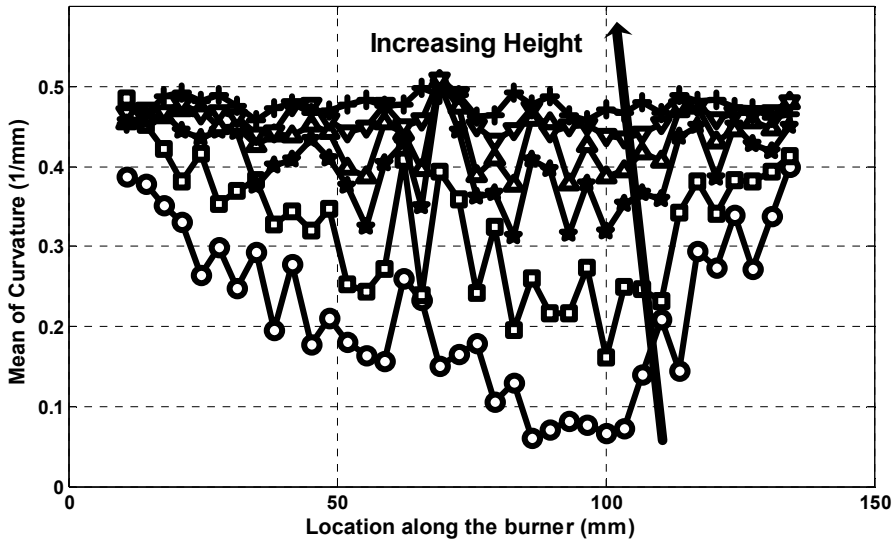

Figure 54. Standard deviation of curvature distribution, measured in the horizontal plane, plotted along the burner width for multiple heights varying from 25 to 127 mm, approximately insteps of 25 mm. The mean velocity, flame speed and turbulence intensity are 3.7 m/s, 0.17 m/s and 5.6%, respectively.

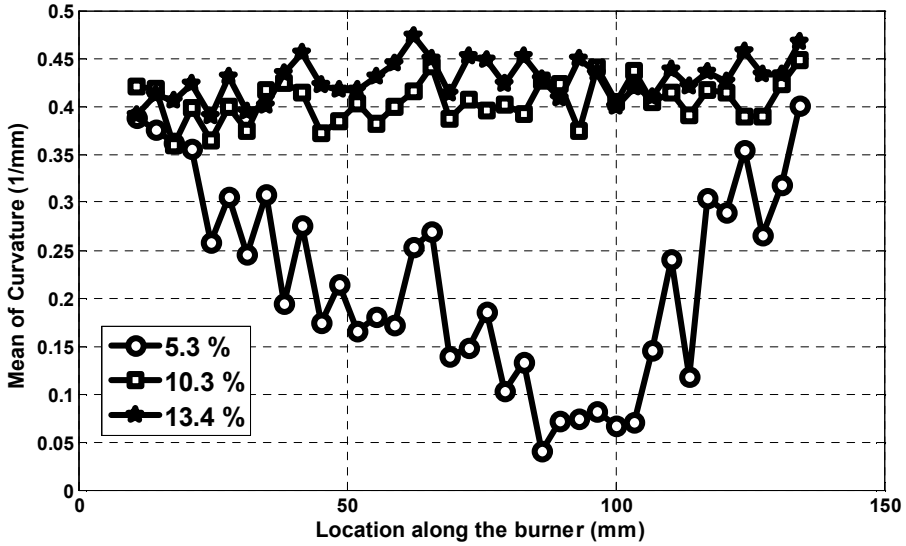

Figure 55. Standard deviation of curvature distribution, measured in the horizontal plane at 25 mm from the burner exit, plotted along the burner width for three turbulence intensities. The mean velocity and flame speed are 3.7 m/s and 0.17 m/s, respectively.

Figure 55 plots the standard deviation of curvature measured at 25 mm for three turbulence intensities: 5.6%, 10.3% and 13.4%. The mean velocity and flame speed are 3.7 m/s and 0.17 m/s, respectively. Standard deviation is seen to marginally increase with height. Comparing Figure 46, curvatures measured in the vertical plane for the 10.3 % turbulence intensity, and Figure 55, we notice that the values are similar in both vertical and horizontal planes.

Le *et. al.*[47] reported curvature measurements performed on an axi-symmetric premixed flame in the horizontal plane. They observed that the PDFs of curvature grew broader with height. In addition, their results suggested that the mean of curvatures in the horizontal plane were close to two times as high as those measured in the vertical flame; i.e., the mean radius of curvature in the horizontal plane was two times smaller compared to the vertical plane measurements. They suggested that the decreasing diameter of the flame with height as the reason for the large difference observed between the vertical plane and the horizontal plane curvatures. In addition, they observed that the mean of the PDFs of curvature in the horizontal plane were strongly influenced by the diameter of the burner.

Notice that the slot burner configuration used in this study does not have any inherent curvature associated with it.

4.4 Flame Front Statistics with Acoustic Forcing

Flame front statistics evaluated with acoustic forcing are presented in this section. The purpose of these experiments was to determine if the acoustic forcing at amplitudes used in this study modifies the flame front characteristics.

Experiments were performed at multiple acoustic amplitudes, varying from 0.17 Pa to 1.02 Pa, measured at the center of the burner. Acoustic forcing was performed at two vertical locations: 51 mm and 81 mm from the burner lip. The mean velocity, flame speed, turbulence intensity and the driving frequency are 4.1 m/s, 0.16 m/s, 5.6% and 500 Hz, respectively. The acoustic velocity calculated using plane wave approximation is 2.5 mm/s for the 1.02 Pa driving amplitude case The ratio of acoustic velocity perturbations to flame speed, u_a/S_L, is 0.01 for the largest driving amplitude. The ratio of turbulent velocity fluctuations to flame speed, u'/S_L, is 1.4.

Figure 56(a) plots the flame brush thickness against height for two driving amplitudes (with driving source at approximately 51 mm above the burner lip) along with the no driving case. Notice that the flame brush thickness is invariant with amplitude. Figure 56(b) plots the flame brush thickness against flame height for two driving locations (51 mm and 81 mm from the burner exit) at a driving amplitude of 1.02 Pa. Again, no change is observed in flame brush thickness for driving at different heights.

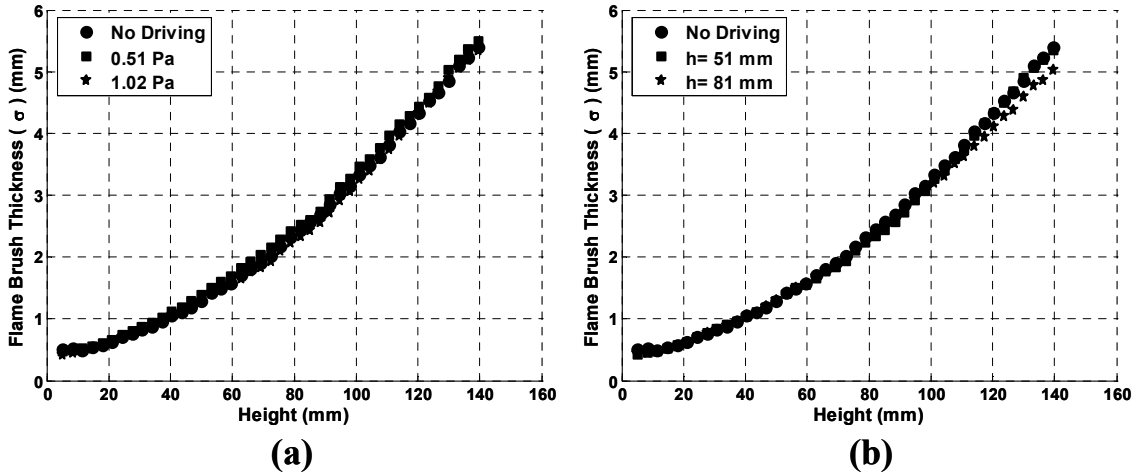

Figure 56.(a) Flame brush thickness plotted against height for 2 driving amplitudes along with no driving case (b) Flame brush thickness plotted against flame height for driving amplitude of 1.02 Pa for two vertical locations of the driving source.

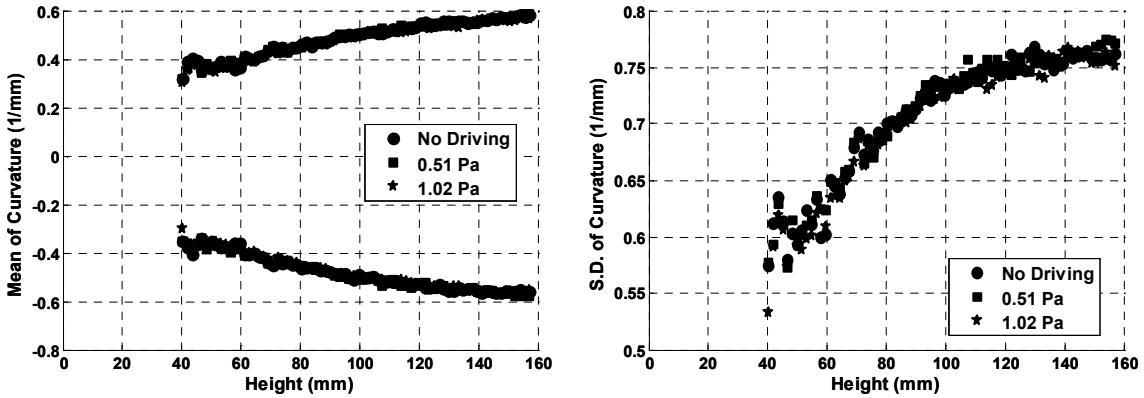

(a) **(b)**

Figure 57.(a) Mean of curvature plotted against height for multiple driving amplitudes with acoustic forcing at a height corresponding to 51 mm (b) Standard deviation all curvatures for the same case.

Figure 57(a) and (b) plot the mean and standard deviation of curvature, respectively, for different driving amplitudes at 51 mm height. The statistics are observed to be independent of the driving amplitude. Similar observation can be made for the case where driving height is varied at a constant amplitude of 1.02 Pa, as shown in Figure 58.

The curvature and flame brush thickness results presented here show no variation with driving amplitude, suggesting that at the driving amplitudes used in this study, the flame front response to the acoustic driving is negligible. The velocity fluctuations induced by the acoustic wave are typically of the order of 1% of the turbulent velocity fluctuations (~ 0.1% of the mean velocity) and thus have negligible effect on the flame front. For comparison, the amplitude threshold for parametric instability, expressed as ratio of acoustic velocity amplitude to flame speed, is 7 at 500 Hz.[22] The ratio of acoustic velocity amplitude to flame speed for the experiments reported here is 0.01. Similarly, the DNS studies performed by Laverdant and his co-workers, where a Gaussian acoustic wave, with pressure amplitudes approximately at 10 Pa, interacts with a turbulent,

premixed flame[32] and diffusion flame[33], reported that the effect of the acoustic wave on the heat release fluctuation are negligible.

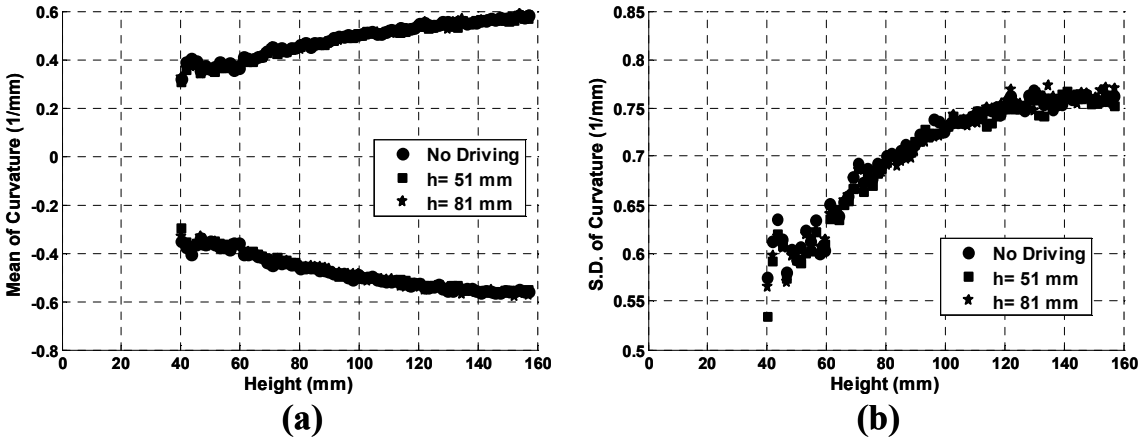

Figure 58.(a) Mean of curvature plotted against height for 1.02 Pa driving amplitude with driving at different heights (b) Standard deviation for all curvatures for the same case.

Chapter 5

Scattered Acoustic Field Measurements

This chapter describes the nature of the scattered acoustic field from premixed turbulent flames. First, it describes the parameters considered in this study- frequency, flame brush thickness, etc. Second, it describes the two experimental approaches, both the near field and far field scattering measurements, used in this study. The last section presents the experimental results, describing the role of each of the parameters in the flame-acoustic wave interactions.

5.1 Overview of the study

This section briefly describes the important experimental parameters investigated in this study. These parameters are discussed in detail in chapter 1.

5.1.1 Frequency

The frequency of the incident acoustic wave and the associated length scale, wavelength (λ), are expected to play an important role in these interactions. The phase of the scattered wave differs from point to point along the flame front because of differences in distance the wave travels before impinging on the flame front and reflecting.[25,10,27] Interference between out of phase waves leads to reduction in coherent power and increase in incoherent power. For a given surface roughness, as the frequency (wavelength) increases (decreases), more and more of the power in the coherent field is transferred in to the incoherent field, leading to incoherent field power saturation once all

the available coherent power is transferred into the incoherent field. In this study, frequency is varied from 1 kHz to 24 kHz.

5.1.2 Flame Brush Thickness (σ)

The characteristic length scale of the turbulent flame is the flame front wrinkling and is quantified as flame brush thickness (σ). Since the phase of the acoustic wave reflecting from different parts of the flame front is strongly dependent on flame front wrinkling, the relative magnitude of the flame brush thickness to the acoustic length scale, σ/λ, is expected to play an important role in these interactions.[10] Flame brush thickness is varied independent of mean velocity and flame speed by controlling the turbulence intensity between values of 5.6% to 13.4%. The flame brush thickness increases from 1.2 mm to 5.2 mm, a factor of 4, for this range of turbulent intensities. For these conditions, σ/λ varies from 0.0035 to 0.36 and $k\sigma$ from 0.022 to 2.3, two orders of magnitude.

5.1.3 Incident Angle (θ_i) and Measurement Angle (θ_r)

As the incident angle and the measurement angle are varied, the wave vector normal to the flame front, $\vec{\ }$, is modified. This has an effect on the perturbation length scale in the direction normal to the flame front. In addition, as indicated by equation (4), which describes the bandwidth of the scattered field, incident and measurement angles have an influence on the spatial dependence of the scattered field. Studies, both theoretical[35,36] and experimental[41], involving ultrasonic wave scattering from thermal plumes, suggest that the processes behind the forward wave scattering and backward wave scattering are different. Varying the incident and measurement angles will illustrate the spatial dependence of the scattered field. Four incident angles (10^o, 25^o, 35^o, and 45^o)

and for each incident angle, four measurement angles (0^o, 10^o, 25^o and 35^o) were considered to evaluate the spatial dependence of the scattered field.

5.1.4 Mean Velocity (U_m) and Flame Speed (S_L)

The effect of velocity fluctuations, u' (dependent on mean velocity), is to perturb the flame while that of the flame speed, S_L, is to smooth out these perturbations. The flame front movement, which plays an important role in these interactions, is determined by the competing effects of u' and S_L. Both mean velocity and flame speed (through equivalence ratio) are varied in this study. Three mean velocities (3.7 m/s, 4.2 m/s and 4.7 m/s) and two flame speeds (0.21 m/s and 0.25 m/s) were considered in this study. These combinations of mean velocity and flame speed results in 6 u'/S_L ratios, ranging from 0.82 to 1.24. The effects of varying these parameters on the flame front characteristics themselves are discussed in Chapter 4.

Note, however, that with changes in equivalence ratio the adiabatic temperature of the flame also changes. Change in temperature has an effect on the sound speed and acoustic impedance jump across the flame front. This has an effect on the critical angle of incidence and the reflection coefficient of the flame front. The ratio of impedance of products to reactants, $\frac{\rho_2 c_2}{\rho_1 c_1}$, changes from 0.37 to 0.39 for the above range of conditions. The speed of sound and critical angles vary from 828 m/s to 853 m/s and 23.2^o to 24^o, respectively, for the above conditions.

5.2 Experimental Approaches

Acoustic measurements were obtained in the far field and the near field. The two measurements are described below. In both the configurations, the source is driven such that the pressure amplitude at the center of the burner is approximately 0.7 Pa.

5.2.1 Far Field Measurements

A large part of the experiments were performed with the acoustic source and the measuring microphones in the far field. The far field for the source and the microphone are determined based on the inverse square law behavior of scattered field, as detailed in Appendix D.

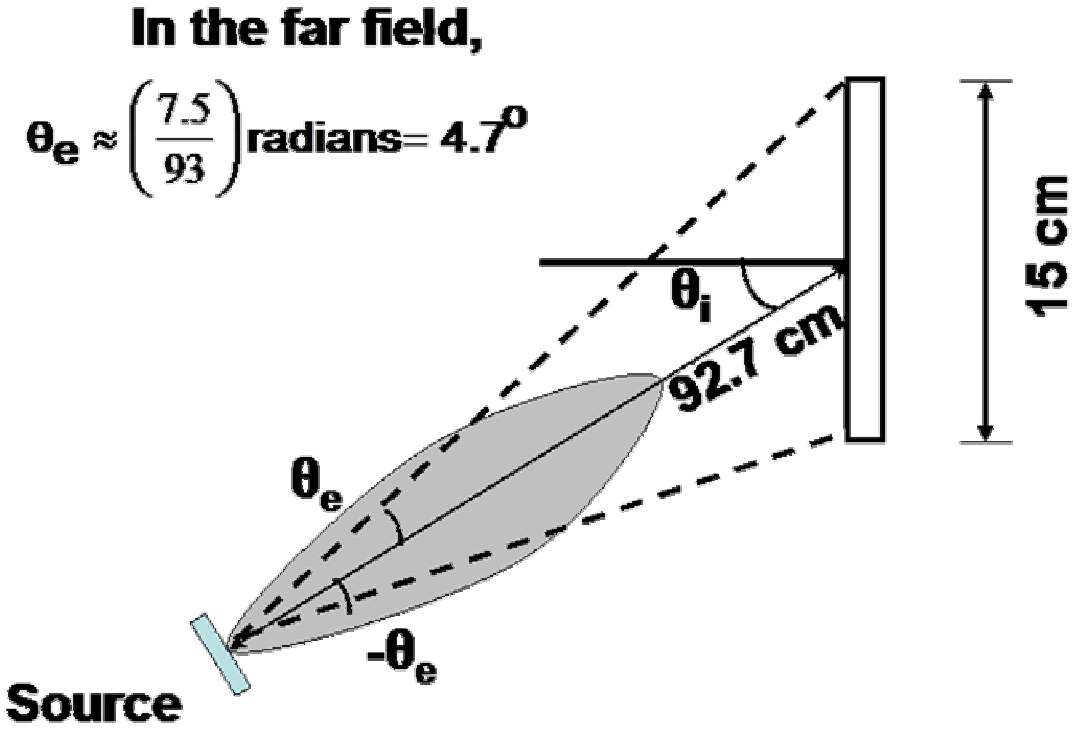

Figure 59. Schematic illustrating the angles made by the burner edges with the acoustic source. The gray cone represents the directivity pattern of the source. The area of the cone included by the dashed lines represents the acoustic power incident on the flame.

The response and directivity patterns of the acoustic source were measured, as explained in chapter 3, and used to correct for the scattered field. For directivity corrections, the angles subtended by the far edge and near edge of the burner with the source are calculated. Figure 59 illustrates the angles involved. Both the near edge and the far edge of the burner make an angle of θ_e with the source. From the dimensions of the burner and the distance of the source from the center of the burner, θ_e is calculated to be approximately 4.7^o for the dimensions shown in Figure 59. The gray cone in the schematic represents the typical measured directivity pattern of the acoustic source. The acoustic power in the directivity cone from -4.7^o to 4.7^o angle is calculated at the experimental frequencies using the corresponding directivity patterns. These values are used to make directivity corrections for the scattered acoustic field power.

The test conditions to evaluate the role of different parameters are listed in Table 3 and Table 4. The role of frequency, flame brush thickness, and angles are discussed in the context of data obtained from conditions listed in Table 3. The mean velocity and flame speed for these conditions are 3.7 m/s and 0.23 m/s, respectively. Table 4 lists the conditions used to study the role of u'/S_L. For these measurements the source is located approximately at 50 mm from the lip of the burner.

In addition to experiments corresponding to Tables 3 and 4, measurements were performed in certain cases for extended set of conditions where it was found useful to support an argument. In those cases, the experimental conditions are explicitly mentioned. Unless otherwise mentioned, the results presented were measured in the far field.

Table 3. Experimental conditions to evaluate the role of frequency, flame brush thickness and incident and measurement angles. The mean velocity and flame speed are 3.7 m/s and 0.23 m/s, respectively. The incident and measurement angles are 10^o, 25^o, 35^o, 45^o and 0^o, 10^o, 25^o and 35^o, respectively. The driving frequency is varied from 1 - 24 kHz. Flame speed values are obtained from Andrews and Bradley[58].

u' (RMS Velocity) (m/s) (Turbulence Intensity)	Flame Brush Thickness (σ) (mm) measured at 51 mm height from burner exit	u'/SL
0.21 m/s (5.6%)	1.2	0.9
0.36 m/s (9.8%)	2.8	1.57
0.38 m/s (10.3%)	2.9	1.66
0.47 m/s (12.7%)	4.1	2.04
0.50 m/s (13.4%)	5.2	2.16

Table 4. Experimental conditions corresponding to u'/S_L studies. The turbulence intensity and incident angles are 5.6% and 25^o, respectively. Scattered field is measured at four measurement angles: 0^o, 10^o, 25^o and 35^o.

Mean Velocity (U_m) (m/s)	Flame Speed (S_L) (m/s)	u'/S_L
3.7	0.21	0.98
3.7	0.25	0.82
4.2	0.21	1.11
4.2	0.25	0.93
4.7	0.21	1.24
4.7	0.25	1.04

5.2.2 Near Field Measurements

Near field measurements are primarily aimed at clarifying specific questions raised by the far field measurements. In the near field measurements, the acoustic source

and the microphones were placed close to the flame, typically at 20 cm from the center of the burner. Since the source was close to the flame in the near field, the distance from the source to different parts of the flame varies considerably. For example, for the case where the source was placed at an angle of 45^{o} to the mean flame and at a distance of 20 cm from the center of the burner, the near side and the far side of the flame edges were at 15.6 cm and 25.8 cm, respectively. This variation in distance means that different parts of the flame front experience different incident acoustic amplitudes, as much as by 50%, assuming an inverse square law[†]. In the far field case, if the source was located at 100 cm and at an angle of 45^{o}, the near side and the far side edges were at 94.8 cm and 105.5 cm, respectively. In this case, the amplitudes experienced by different parts of the flame are with in 10% of each other. Similarly, the near side and the far side angles formed by the burner at the source in the near field are 25^{o} and 57^{o}, respectively, while those angles in the far field are 42^{o} and 48^{o}, respectively. This wide variation of angles in the near field with respect to different parts of the flame makes the directivity corrections complex. Finally, the source pattern itself is complex in the near field, e.g., the acoustic field could have pressure nodes in the axial location.[59] Because of these complexities in the near field, it is difficult to make corrections to the scattered acoustic field. For this reason, acoustic field results are discussed only in a qualitative sense.

The main advantage offered by the near field measurements is this: it is possible to study the scattered field dependence on the local flame front characteristics. For example, in the far field, the scattered field characteristics are determined by the characteristics of the whole flame. In the near field, however, the scattered field characteristics are determined only by the part of the flame that is exposed to the acoustic

[†] Not a good assumption in the near field.

beam. At high frequencies, the acoustic beam tends to be quite narrow, see Figure 11, and it is possible to direct the acoustic beam on to different parts of the flame. This is particularly advantageous because it allows us to traverse along the height of the axially developing turbulent flame in the near field. Notice from discussions in chapter 4 that the flame brush thickness increases with height.

5.3 Scattered Field Description

This section describes the nature of the scattered field and its dependence on the parameters described in section 1. We start with the role of frequency (wavelength), followed by the flame brush thickness variation. Next, the dependence of scattered field on incident and measurement angles is discussed. This section ends with the description of u'/S_L effects on the scattered field.

5.3.1 Frequency

Figure 60(a) presents a typical power spectrum of the measured scattered acoustic field when the flame and the transducer are on. The driving frequency (f_d), spectral resolution of the spectrum (Δ), mean velocity (U_m), flame speed (S_L), turbulence intensity (TI), incident (θ_i) and measurement (θ_r) angles are 18 kHz, 2 Hz, 3.7 m/s, 0.26 m/s, 5.6%, 30^o and 20^o, respectively. The large peak at the driving frequency is evident in Figure 60(a).

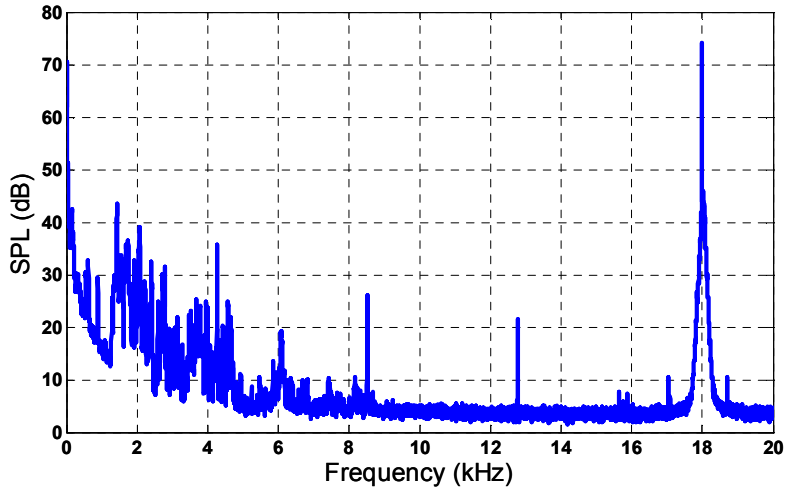

(a)

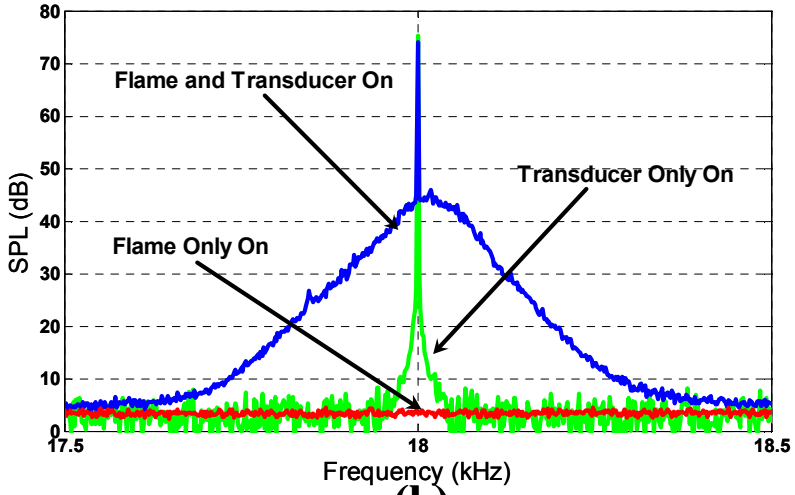

(b)

Figure 60.(a) Typical measured power spectrum of acoustic field with flame and transducer on, f_d =18 kHz (b) Detail of measured power spectrum of acoustic data, f_d =18 kHz. [Δ, U_m, S_L, TI, θ_i, θ_r] =[2 Hz, 3.7 m/s, 0.26 m/s, 5.6 %, 30^o and 20^o].

Figure 60(b) shows a detail of the spectrum when f_d = 18 kHz for three cases: 1) flame on and transducer off, 2) transducer on and flame off, and 3) both flame and transducer on. Several items should be noted from these results.

First, note the extremely narrow bandwidth of the spectrum when only the transducer is on. It is dominant only at the driving frequency and negligible at all others.

This result demonstrates that spectral leakage from the driving frequency is a negligible source of error.

Second, when the transducer is on, the power spectrum has substantially more power than the background combustion noise in the frequency interval centered around the driving frequency; e.g., between f = 17.5 - 18.5 kHz in Figure 60(b). This result illustrates that the sidebands of interest can be clearly distinguished from background noise over a range of frequencies. It also shows that the dominant noise source in the vicinity of the driving frequency is due to incoherent waves excited by the incident disturbance and not turbulent combustion and flow noise[‡].

To provide some context on the effects of the flame, it is useful to briefly consider the related problem of sound scattering from the heated jets[38] and thermal plumes[39,40,41]. Petrossian and Pinton[38] measured acoustic waves scattered off a heated jet in back scattering mode (meant to capture temperature fluctuations as opposed to temperature and vorticity fluctuations in the forward scattering mode). A typical spectrum (for a nominal driving frequency of 60 kHz) measured in that study is reproduced in Figure 61 for comparison. The x-axis is the frequency in kHz and y-axis is power spectral density in Decibels. Figure 61(a) corresponds to the isothermal jet case. Figure 61(b) corresponds to the case with temperature fluctuations. Notice that for the case with temperature fluctuations, there is a clear band of frequencies to the left of the driving frequency peak. The source of these frequencies is the temperature inhomogeneities in the flow. The maximum amplitude point in the sideband is related to the mean advection velocity due to the Doppler shift.

[‡] Relative contribution of the cold jet and the pilot flame to the scattered field are small and are discussed Appendix E.

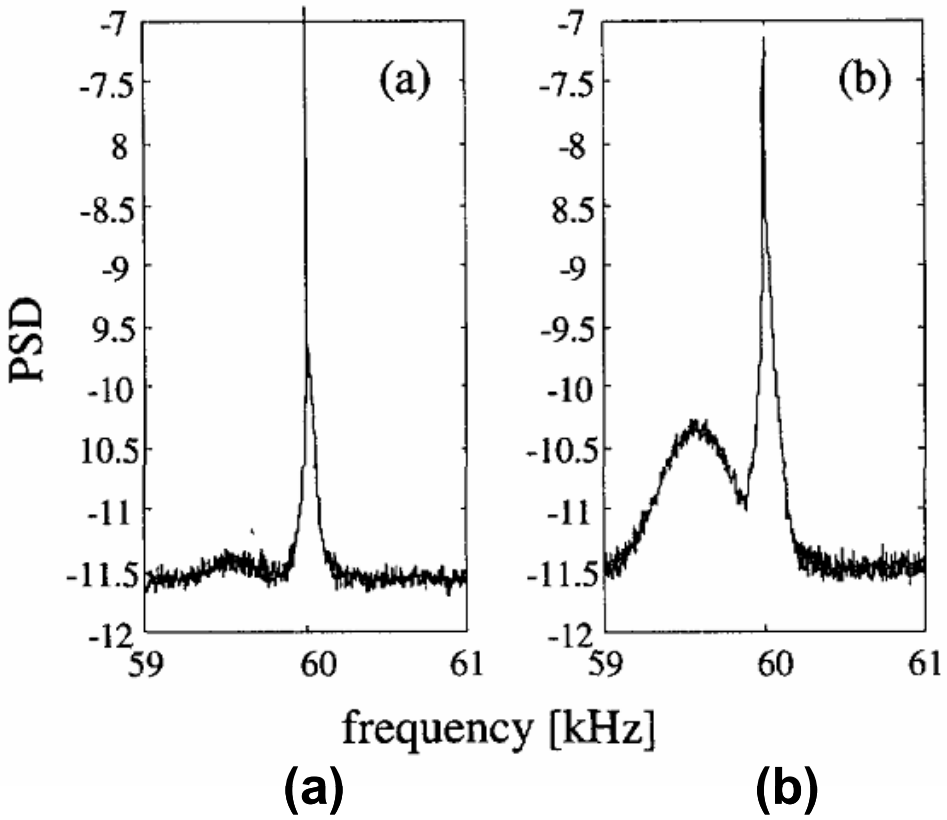

Figure 61. Typical scattered acoustic spectra measured off a heated jet in the study reported by Petrossian and Pinton[38] for a nominal incident frequency of 60 kHz (a) Isothermal jet (b) Jet with temperature fluctuations.

Referring to Figure 60, different aspects of the scattered field spectrum such as the incoherent field strength, bandwidth and the shape of the spectral sidebands are discussed below.

Spectra as shown in Figure 60 are obtained for each of the driving frequencies for all conditions listed in Table 3. Figure 62(a) plots the raw spectra (uncorrected for the source response and directivity) for six frequencies (4, 8, 12, 16, 20 and 24 kHz). Figure 62(b) plots the spectra, corrected for the source response and directivity. The mean velocity, flame speed, turbulence intensity, incident and measurement angles are 3.7 m/s,

0.23 m/s, 5.6%, 10° and 0°, respectively. The spectra are plotted on the frequency axis as f-f_d, such that the driving frequency is always at 0 Hz. The contribution of the background combustion noise has been subtracted out using data taken at the same conditions with only the flame on.

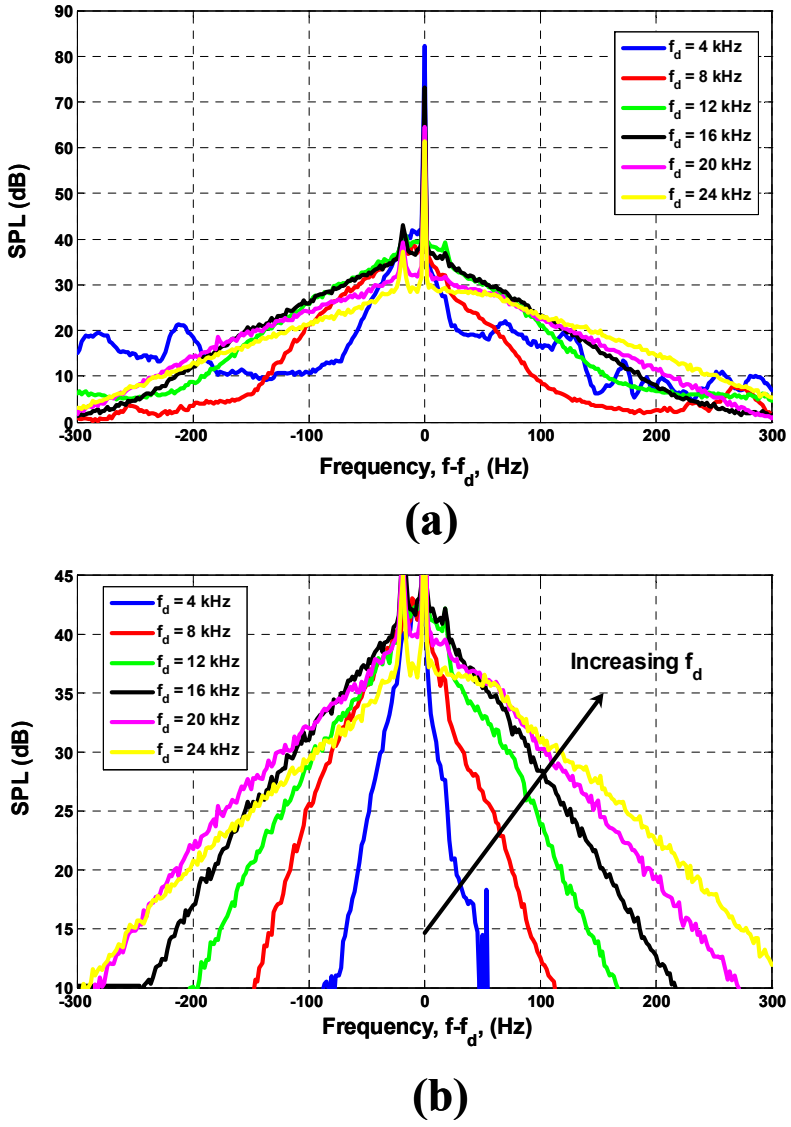

Figure 62. Spectra for 6 frequencies for [U_m, S_L, TI, θ_i, θ_r] = [3.7 m/s, 0.23 m/s, 5.6%, 10° and 0°]. (a) Raw spectra (b) Spectra corrected for response and directivity characteristics of the source.

Figure 62(b) shows that the area under the spectra, related to the scattered incoherent power, increases substantially with driving frequency (note that the y-axis is in Decibels, a logarithmic scale). The area under the spectra is quantified as sound pressure level[§] (SPL). First, the area contained between the background combustion noise spectrum and the case when both the flame and the transducer are on is determined, excluding the coherent peak at f = f_d. Then SPL is determined using the following expression:

$$SPL = 10\log_{10}\frac{\overline{p'^2}}{p_{ref}^2} \tag{13}$$

where $\overline{p'^2}$ is the area referred to above and p_{ref} is 20 μPa.

The dependence of scattered incoherent field, quantified as SPL, on driving frequency is plotted in Figure 63(a) and (b) for 1-24 kHz[**]. From Figure 63(a), where the x-axis is set to linear scale, we see that the SPL increases substantially at lower frequencies, and then appears to saturate to a limiting value at approximately 16 kHz. With increase in frequency, the wavelength decreases and the scattered waves from different parts of the flame tend to be more and more out of phase, leading to further conversion of the incident (coherent) acoustic power into the incoherent power in the sidebands. The incoherent field, quantified as SPL, saturates once all the available power in the coherent field is transferred into the incoherent field.[10] This argument suggests that any characteristic of the flame front that enhances phase difference of the acoustic wave

[§] Further details of the SPL estimation are discussed in Appendix A.

[**] Experiments were performed for driving frequencies up to 45 kHz. No new features were observed for frequencies beyond 20 kHz, See Appendix G. For that reason, experiments reported here were performed for 1-24 kHz range of frequencies.

from different parts of the flame front will enhance the coherent to incoherent field transfer process, leading to a lower saturation frequency.

To illustrate the nature of SPL dependence on frequency, the x-axis is set to logarithmic scale in Figure 63(b). We see that the SPL increases linearly in Figure 63(b), suggesting a power law dependence on the driving frequency. Analysis by Lieuwen[10] predicts that the incoherent power increases as f_d^2 at low frequencies and as $e^{-\frac{1}{f_d^2}}$ at high frequencies.

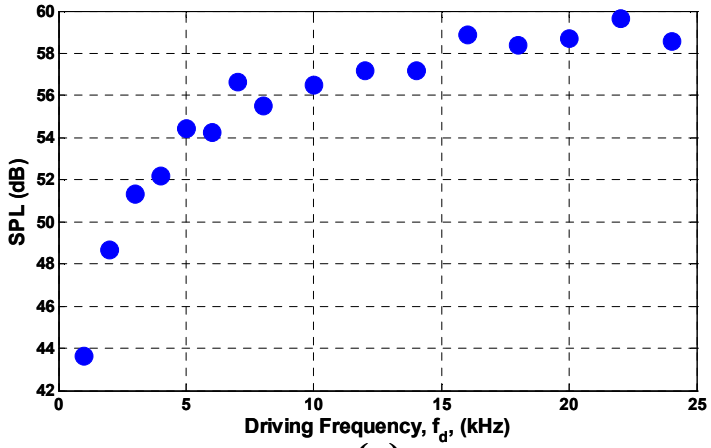

(a)

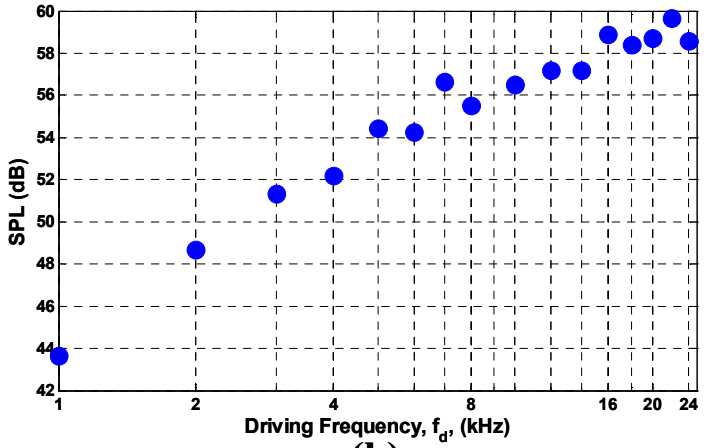

(b)

Figure 63. SPL plotted against driving frequency for [U_m, S_L, TI, θ_i, θ_r] = [3.7 m/s, 0.23 m/s, 5.6%, 10^o and 0^o]

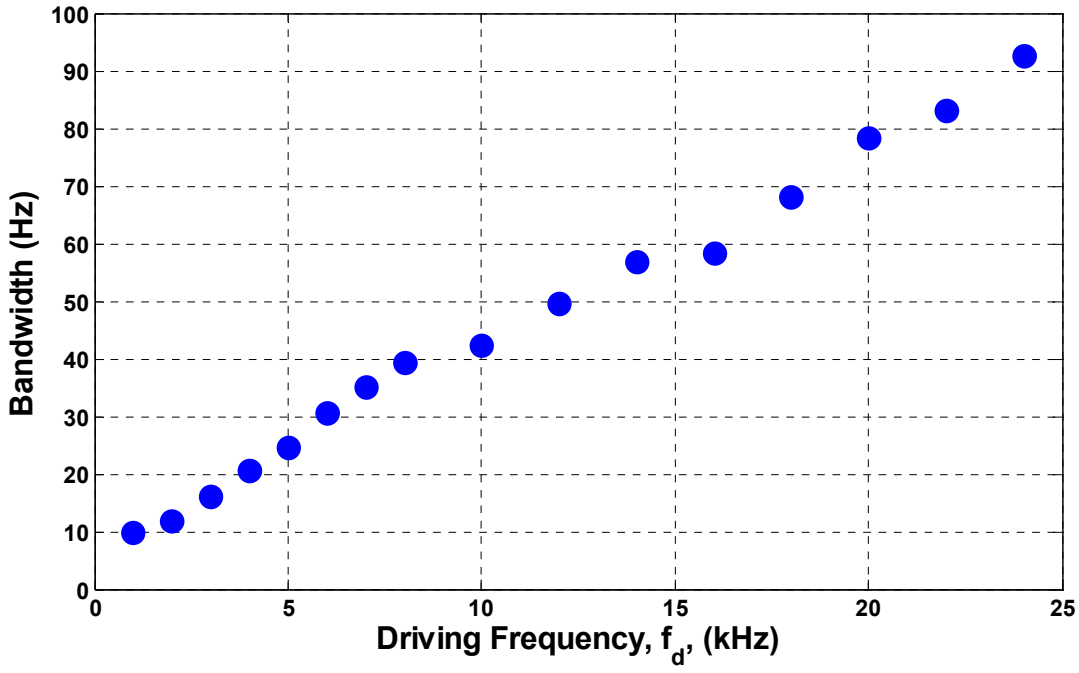

Figure 64. Spectral bandwidth plotted against frequency for [U_m, S_L, TI, θ_i, θ_r] = [3.7 m/s, 0.23 m/s, 5.6%, 10^o and 0^o]. These are the same conditions as in Figure 62 and Figure 63.

Figure 62(b) shows that the range of frequencies over which the incoherent sidebands contain appreciable power, referred to as bandwidth, increases monotonically with frequency. Bandwidth is calculated based on a centroid approach. It is quantified using the following expression:

$$bandwidth = \frac{\int_{f_l}^{f_h} |f_d - f| P(f) df}{\int_{f_l}^{f_h} P(f) df} \tag{14}$$

where $P(f)$ is the power spectral density of the scattered field. The quantities, f_l and f_h are the frequencies beyond which the low and high frequency sidebands are indistinguishable

from background combustion noise. Essentially, a centroid is found for low and high frequency sidebands and added to get the total bandwidth.

The calculated bandwidth is plotted against driving frequency in Figure 64. Notice that the bandwidth increases monotonically with frequency. Simple Doppler shift arguments summarized in equation (4) suggests that this relationship should be linear. The bandwidth, as shown in Figure 64, is linear with driving frequency. This measured dependence shows that the scattered wave characteristics are generated by a phase-modulation process (as opposed to amplitude modulation). Indeed, the theoretical studies[10,25] that analyzed the nature of the scattered field from turbulent premixed flames made this assumption and the results presented here support that. Aforementioned ultrasound scattering experiments on heated jet[38] and thermal plume[40] have also reported such linear increase in bandwidth with incident acoustic wave frequency. They[38] suggest that the band of frequencies near the incident wave frequency are generated by phase modulation processes induced by the temperature fluctuations.

Next, the shape of the incoherent sidebands is considered. Note from Figure 62(b), that both low and high frequency sidebands exhibit an almost perfect exponential decay[††], as evidenced by the near linear dependence of the PSD in Decibels upon $f-f_d$. The relative change in shape of these sidebands is illustrated in Figure 65, where the x-axis has been scaled by driving frequency and both low and high frequency side bands are normalized to have the same area under them. These curves clearly illustrate the nearly constant shape of the sidebands.

[††] The 20 Hz peak seen in the low frequency sideband is thought to be because of the oscillations in the shear layer on the products side. This is described further in Appendix E.

Scattered field measurements performed on an axi-symmetric burner[60] reported a dramatic change in shape of the high frequency sidebands for driving frequencies greater than 10 kHz and nearly constant shape in the low frequency side bands. However, note that the high temperature products between the acoustic source and the flame front in this axi-symmetric burner introduces complexities, as explained in chapter 2, and could possibly be reason for such observed behavior with high frequency sidebands.

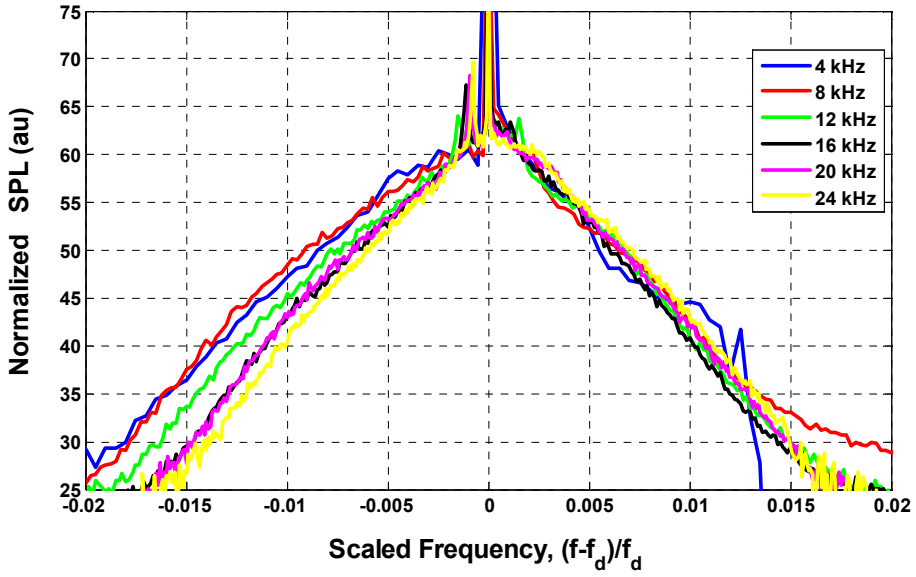

Figure 65. Normalized spectra for 6 driving frequencies plotted against scaled frequency. Area under the low frequency sidebands and high frequency sidebands are made equal separately. Experimental conditions are same as in Figure 63 and Figure 64.

5.3.2 Turbulence intensity (Flame Brush Thickness)

In the discussion above in detailing the role of frequency, it is argued that:

(i) Phase of the scattered wave from different parts of the flame front is different due to distance traveled by the wave before impinging and reflecting

(ii) As frequency increased, for a given flame front surface variation (wrinkling), the surface appears progressively rougher, which leads to further conversion of

coherent field power into incoherent field leading to incoherent power saturation

Extending these arguments, if the wrinkling of the flame front is increased, the scattered field from different parts of the flame will be further out of phase for a given frequency. In other words with increased flame front wrinkling, incoherent SPL is expected to increase at a faster rate with frequency leading to saturation at low frequency. These arguments suggest that the ratio of flame front wrinkling to wavelength, σ/λ, is an important parameter. In this section, experimental results are presented to illustrate the role of flame brush thickness.

Measurements are performed both in the far field and near field to capture the effect of flame brush thickness. In the far field measurements, the flame brush thickness is varied by varying turbulence intensity. Table 3 lists the flame brush thickness measured at a height of 51 mm from the lip of the burner for the 5 turbulence intensities. In the near field, for a fixed turbulence intensity, the source and the microphones are traversed along the height. With height, flame brush thickness increases and thus the near field measurements are expected to capture the effect of flame brush thickness. However, as explained in section 2, only qualitative observations are made for near field measurements. We first present the far field measurements.

Figure 66 plots SPL of the scattered incoherent field against driving frequency for five turbulence intensities. The mean velocity, flame speed, incident and measurement angles are 3.7 m/s, 0.23 m/s, 25^o and 0^o, respectively. The results in Figure 66 show that, for a given flame brush thickness (turbulence intensity), the SPL increases exponentially at lower frequencies and then seems to saturate approximately at 8 kHz. The key

observation is that the saturation frequency does not change with increase in turbulence intensity. Flame brush thickness increases by a factor of 4 (1.2 mm to 5.2 mm) over the range of conditions presented in Figure 66. The parameter, σ/λ, varies from 0.0035 to 0.36, over two orders of magnitude, for these conditions. If the ratio of flame brush thickness to the wavelength, σ/λ, is the parameter governing these interactions, then, with increase in flame brush thickness, the SPL is expected to saturate at a lower frequency, close to 2 kHz for the largest turbulence intensity case. Data presented in Figure 66 do not show such behavior.

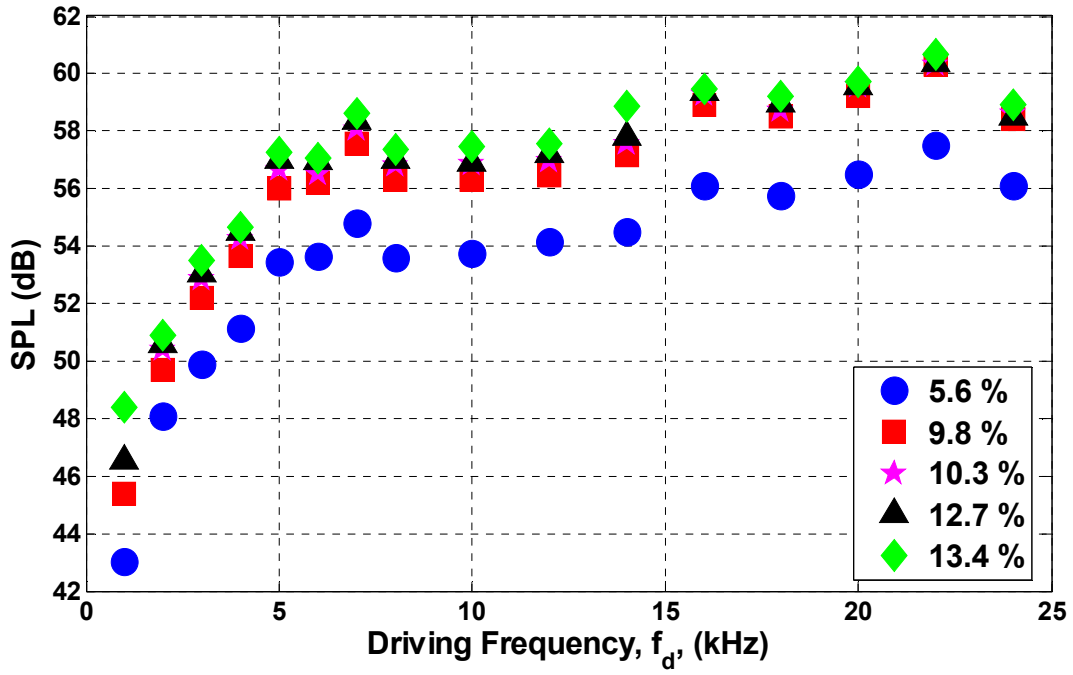

Figure 66. SPL plotted against frequency for five different turbulence intensities (flame brush thickness) for $[U_m, S_L, \theta_i, \theta_r] = [3.7 \text{ m/s}, 0.23 \text{ m/s}, 25^o, 0^o]$.

Figure 67 plots results for similar experimental conditions to Figure 66 except for a measurement angle of 35^o instead of 0^o. Again, there is no change in saturation frequency with increased turbulence intensity. However, there is a change in saturation

frequency from Figure 66 to Figure 67. This dependence on angle is discussed in the next section.

The key observation from the results presented in Figure 66 and Figure 67 is the invariance of the saturation frequency with flame brush thickness.

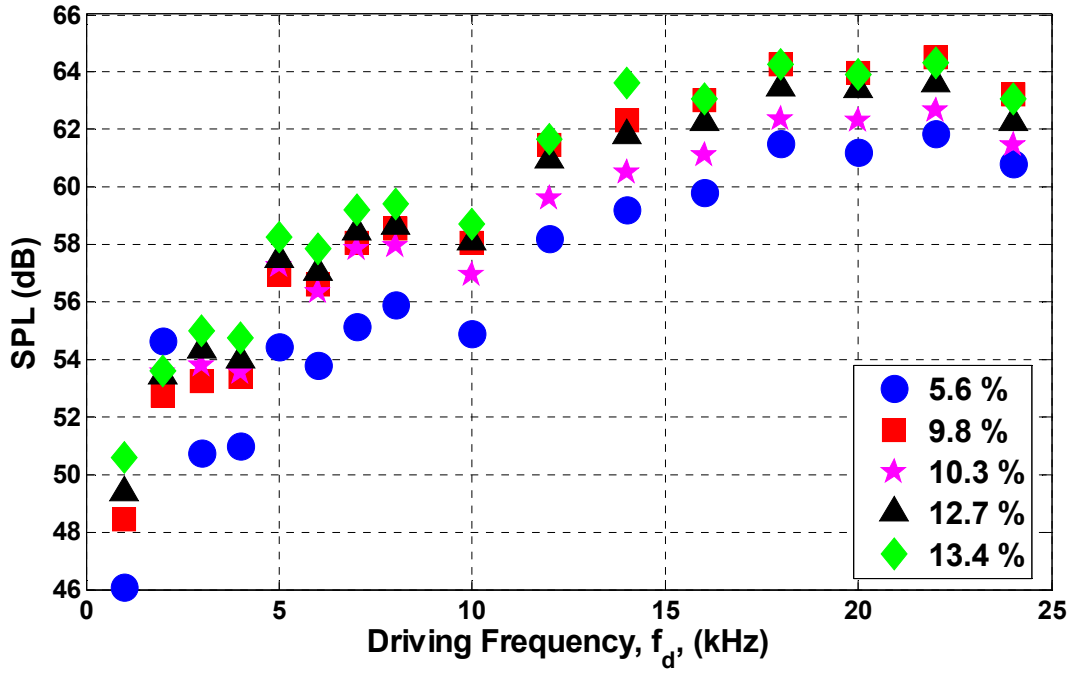

Figure 67. SPL plotted against frequency for five different turbulence intensities (flame brush thickness) for $[U_m, S_L, \theta_i, \theta_r] = [3.7 \text{ m/s}, 0.23 \text{ m/s}, 25^o, 35^o]$.

Next, near field measurement results are compared with far field measurements in Figure 68. For the near field case, the acoustic source and microphones were located approximately at a distance of 23 cm from the center of the burner. The source and the microphones were traversed with height in the near field. The source and microphones for the far field measurements compared here were located at approximately 100 cm. Measurements for two turbulence intensities are reported for the far field case. The mean

velocity, flame speed, incident and measurement angles are 4.7 m/s, 0.26 m/s, 30° and 20°, respectively, for both near field and far field measurements.

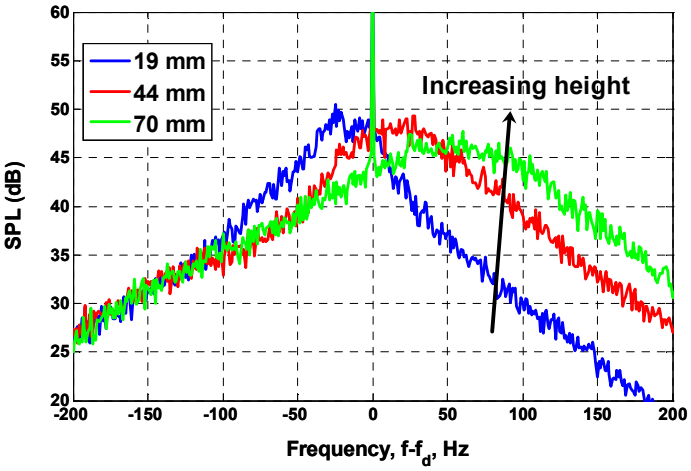

Figure 68. Incoherent spectral sidebands for f_d = 18 kHz. [U_m, S_L, θ_i, θ_r] = [4.7 m/s, 0.26 m/s, 30°, 20°] (a) Three heights, near field measurements. (b) Two turbulence intensities, far field measurements.

Figure 68(a) plots the dependence of the incoherent sidebands, measured in the near field, for f_d =18 kHz upon f-f_d at three heights. In this case, increasing height is equivalent to increasing flame brush thickness. Notice that, as the height increases, the high frequency sideband shifts upward more than the low frequency sideband. Figure

68(b) plots the incoherent sidebands for f_d = 18 kHz upon f-f_d for two turbulence intensities measured in the far field. Again, notice that there is very little change in the low frequency sidebands while the high frequency sideband shifts upward with increase in turbulence intensity. The two different methods of varying the flame brush thickness yielded similar trends in the spectral shape, indicating that flame brush thickness has a role in these interactions, but isn't manifested in the far field measurements.

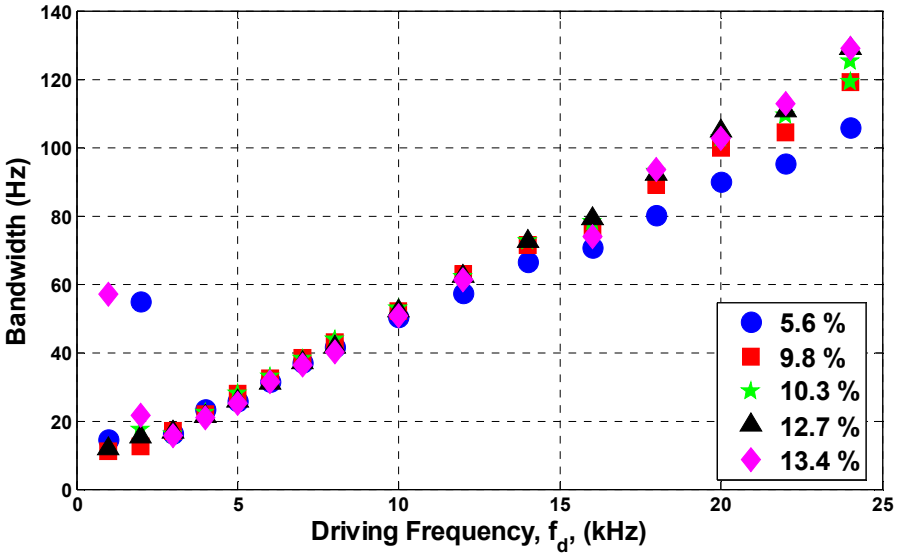

Figure 69. Bandwidth plotted against frequency for 5 turbulence intensities. [U_m, S_L, θ_i, θ_r] = [3.7 m/s, 0.23 m/s, 25°, 0°].

Next, the dependence of spectral bandwidth on turbulence intensity is considered. Figure 69 and Figure 70 plots bandwidth against frequency for the same experimental conditions as Figure 66 and Figure 67, respectively. First, note that the bandwidth increases with frequency, as already pointed out in the discussion of frequency. Second, bandwidth slightly increases with turbulence intensity. From Figure 69, we see that the bandwidth increases from 10 Hz to 100 Hz for 5.6% turbulence intensity case and from 10 Hz to 120 Hz for 13.4% turbulence intensity case. This trend can be explained based

on the bandwidth equation derived in the introduction chapter. Increase in turbulence intensity leads to increased flame front movement, as indicated by increase in flame brush thickness. Increased flame front movement leads to the coherent power being transferred into a wider range of frequencies because of the Doppler shift effect. By definition, this results in an increase in bandwidth. However, notice that the bandwidth changes by only 20% for a factor of 3 change in turbulence intensity.

Comparing across Figure 69 and Figure 70, we see that the rate (slope) at which bandwidth increases with frequency is different for the two measurement angles. Bandwidth varies approximately from 10 Hz to 120 Hz and 10 Hz to 100 Hz for 0^o and 35^o measurement angles, respectively. This dependence on measurement angles is further discussed in the next section.

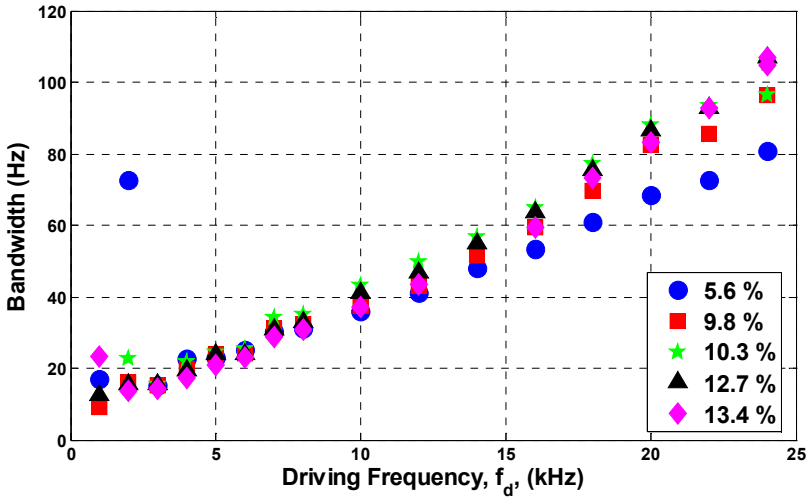

Figure 70. Bandwidth plotted against frequency for 5 turbulence intensities. [U_m, S_L, θ_i, θ_r] =[3.7 m/s, 0.23 m/s, 25^o, 35^o].

5.3.3 Incident and Measurement Angles

Far field measurements of the scattered field, as listed in Table 3, were performed for four incident angles (θ_i =10°, 25°, 35° and 45°). For each incident angle, spatial measurements were performed at four measurement angles (θ_r = 0°, 10°, 25° and 35°). Mean velocity and flame speed are set to 3.7 m/s and 0.23 m/s, respectively.

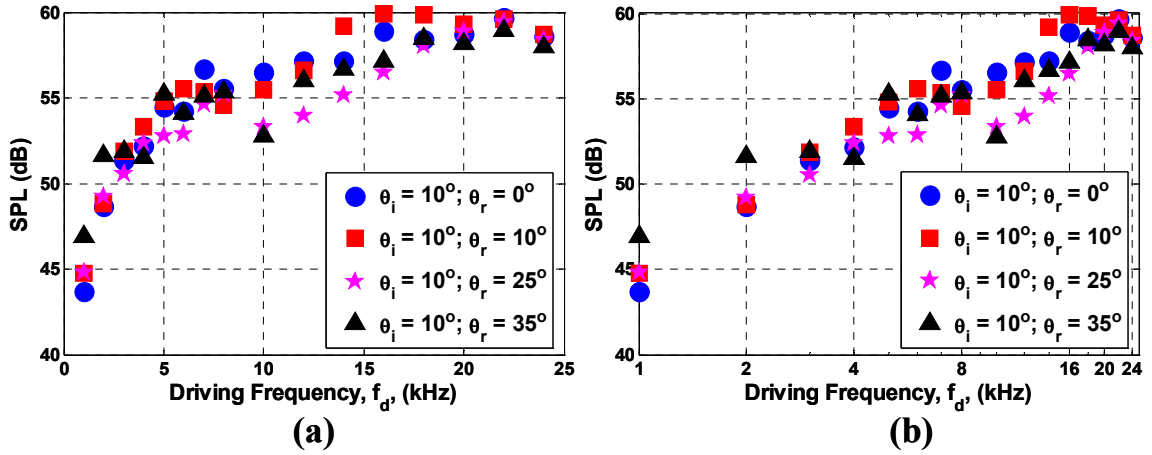

Figure 71. SPL plotted against frequency for four measurement angles. [U_m, S_L, TI, θ_i] = [3.7 m/s, 0.23 m/s, 5.6%, 10°].

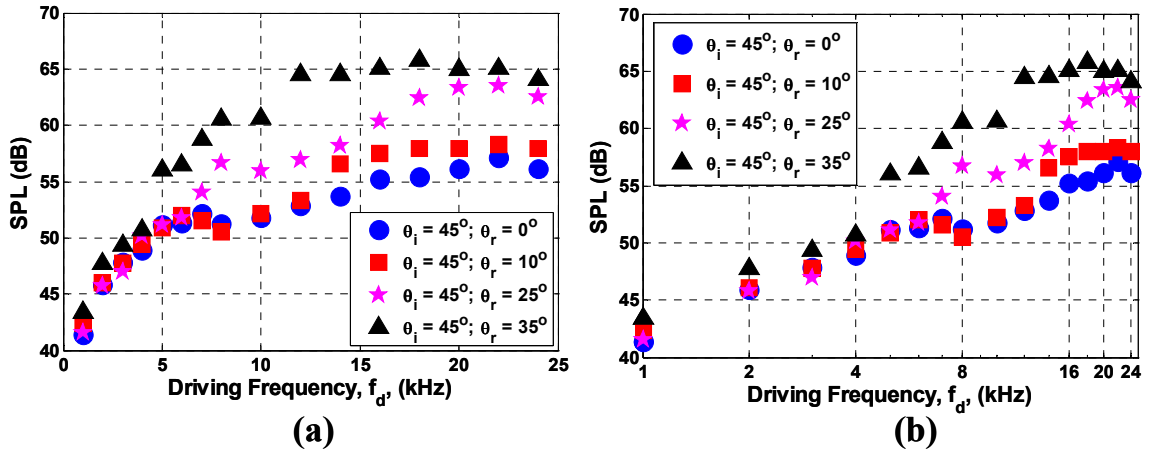

Figure 72. SPL plotted against frequency for four measurement angles. [U_m, S_L, TI, θ_i] = [3.7 m/s, 0.23 m/s, 5.6%, 45°].

Figure 71 and Figure 72 plot the SPL against frequency for four measurement angles for a fixed incident angle corresponding to 10^o and 45^o, respectively. From Figure 71, we see that there is a definite change in the SPL behavior with measurement angle. This behavior is further evident in Figure 72, where the SPL saturation frequency is observed to change with measurement angle. In Figure 72, for 10^o measurement angle case, the SPL seems to saturate at approximately 14 kHz while it does not saturate until about 20 kHz for 25^o measurement angle case. From Figure 72(b), where the x-axis is set to log scale, notice that the SPL increases in a linear fashion for until 14 kHz and 20 kHz for $\theta_r = 25^o$ and 35^o, respectively, while there is a definite change in slope at 8 kHz for $\theta_r = 0^o$ and $\theta_r = 10^o$. Similar behavior is observed with incident angles for a fixed measurement angle, as discussed below.

Figure 73 and Figure 74 plot the SPL against driving frequency for multiple incident angles for a fixed measurement angle corresponding to 0^o and 35^o, respectively. Trends that are similar to Figure 72 are observed here: a change in slope is observed with increase in incident angle, particularly evident in Figure 74.

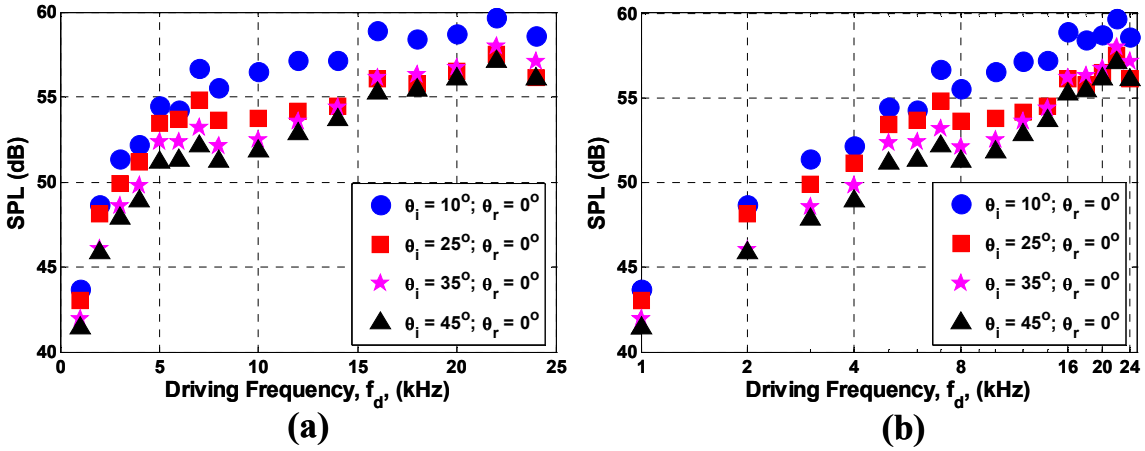

Figure 73. SPL plotted against frequency for four incident angles. [U_m, S_L, TI, θ_r] = [3.7 m/s, 0.23 m/s, 5.6%, 0^o].

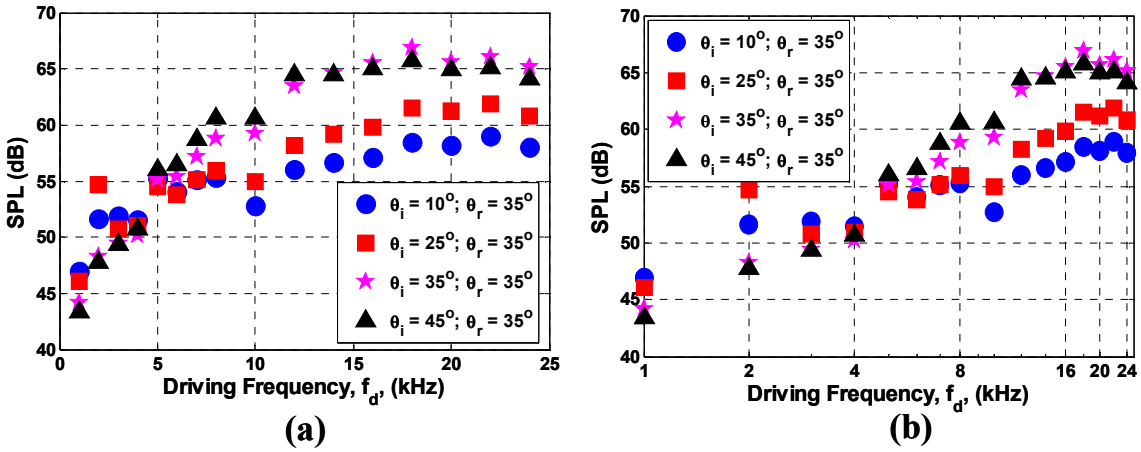

Figure 74. SPL plotted against frequency for four incident angles. [U_m, S_L, TI, θ_r] = [3.7 m/s, 0.23 m/s, 5.6%, 35^o].

This observed dependence of saturation characteristics on angles is expected. With angles, the wave vector, $\vec{k}$, is modified leading to a change in the "effective" wavelength. The wave vector normal to the flame, as illustrated in Figure 75, takes the flowing form:

$$|\vec{k}n| = |\vec{k}||\vec{n_r} - |\vec{k}||\vec{n_i}| = |\vec{k}|(\cos\ \theta_i + \cos\ \theta_r) \tag{15}$$

This argument implies that if the SPL is plotted against a quantity related to the wave vector in the normal direction to the flame front, such curves for all incident and measurement angles should collapse. However, before we do that, each of those curves needs to be normalized by the saturation SPL because saturation SPL is not the same for all combinations of incident and measurement angles, as can be seen in Figure 74. This

behavior is thought be because of the critical angle of the flame front and its dependence on temperature ratio across the flame front and is addressed further in the next section.

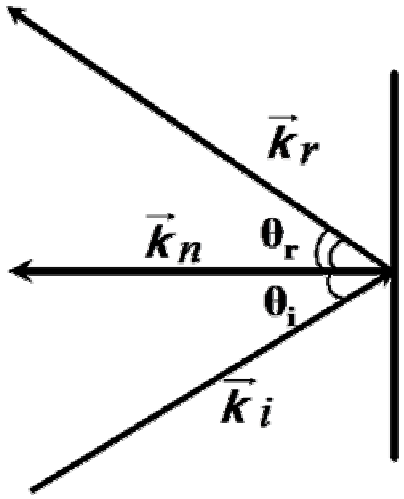

$$|\vec{k}_n| = |\vec{k}||\vec{n}_r| - |\vec{k}||\vec{n}_i| = |\vec{k}|(\cos\theta_i + \cos\theta_r)$$

Figure 75. Illustration of the wave vector normal to the flame front. Incident and scattered wave vectors are also shown in this figure. The vectors $\vec{n}_i$ and $\vec{n}_r$ are the unit vectors in the incident and the measurement directions, respectively.

Figure 76 plots the normalized SPL against frequency multiplied by the sum of the cosines of the incident and measurement angles for the 5.6% turbulence intensity case. Notice that the frequency is proportional to the wave number of the incident wave and thus Figure 76 is equivalent to plotting SPL against the wave number. Figure 76 contains all the 16 combinations of incident and measurement angles with 16 frequencies for each combination. The data is smoothed over 3 points, i.e., one point to the left and one point to the right. We see that the saturation seems to occur approximately at 14 kHz. Also, notice that this curve is similar to Figure 63 where the SPL is plotted against the frequency for an incident angle of 10^o and measurement angle of 0^o. For both Figure 76

and Figure 63, the turbulence intensity, mean velocity and the flame speed are the same (5.6%, 3.7 m/s and 0.23 m/s, respectively). Notice that the dependence of SPL against frequency shown in Figure 63, is the closest to the "universal" SPL vs. frequency for this turbulence intensity condition because these conditions represent the case where incident and measurement angles are the closest to the flame surface normal and hence need smallest correction because of the angles. This similarity between two figures further points towards the role of wavelength (inversely proportional to frequency) as a key parameter in these interactions.

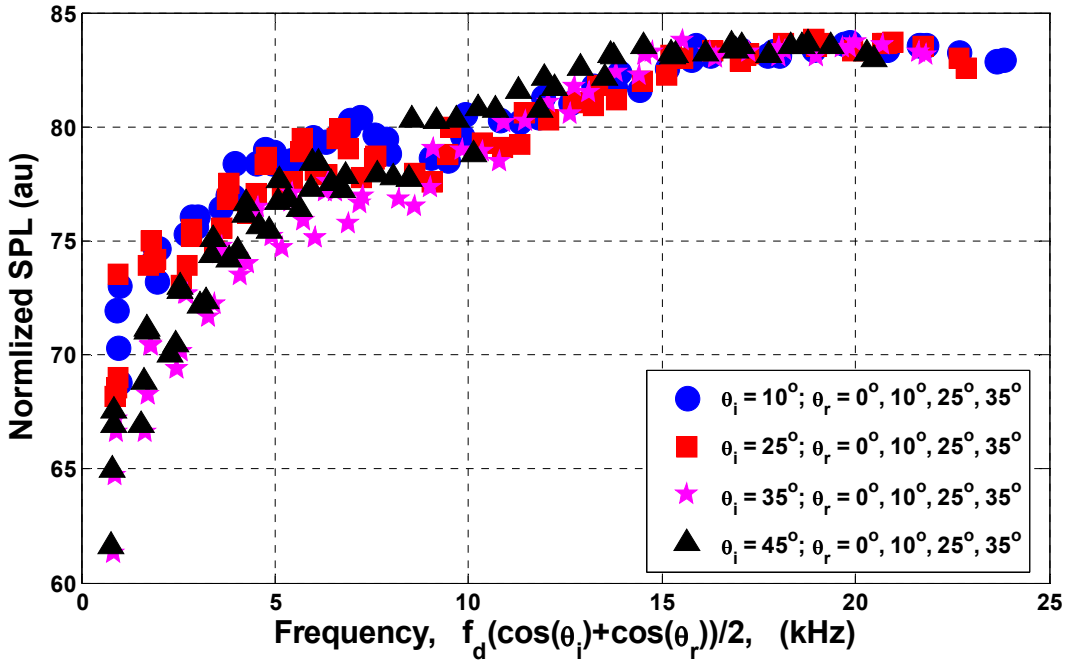

Figure 76. Normalized SPL plotted against the product of frequency and the sum of the cosines of the incident and measurement angles. This plot includes data from 4 incident angles and 4 measurement angles for each incident angle. [U_m, S_L, TI] = [3.7 m/s, 0.23 m/s, 5.6%]

Figure 77 plots curves similar to Figure 76 for the 13.4 % turbulence intensity. As listed in Table 3, this plot corresponds to approximately 4 times the flame brush thickness

of that of Figure 76. However, the variation seen in here is similar to Figure 76. This observation, again, points towards the invariance of the saturation frequency with flame brush thickness, as pointed out in the previous section.

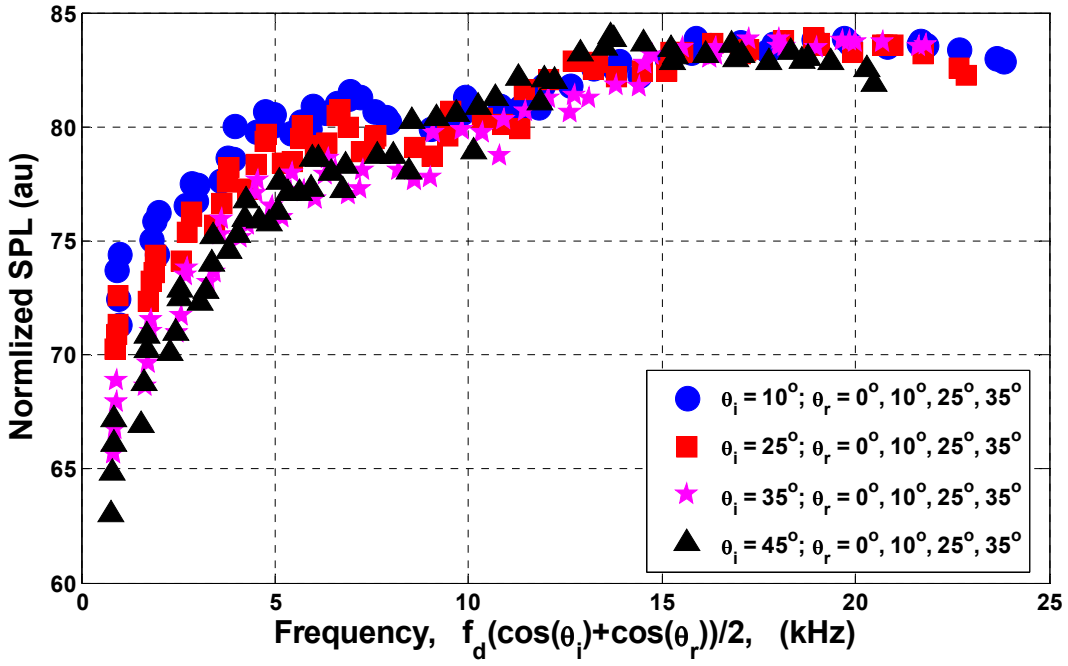

Figure 77. Normalized SPL plotted against the product of frequency and the sum of the cosines of the incident and measurement angles. This plot includes data from 4 incident angles and 4 measurement angles for each incident angle. [U_m, S_L, TI] = [3.7 m/s, 0.23 m/s, 13.4%]. This figure is similar to Figure 76 except for the turbulence intensity.

Next, we discuss the dependence of the spectral bandwidth on the incident and measurement angles. Figure 78 plots bandwidth against frequency for multiple measurement angles for a fixed incident angle. Part (a) and (b) correspond to 25^o and 45^o incident angles, respectively. We see that the rate at which the bandwidth increases, the slope, decreases with increase in measurement angle.

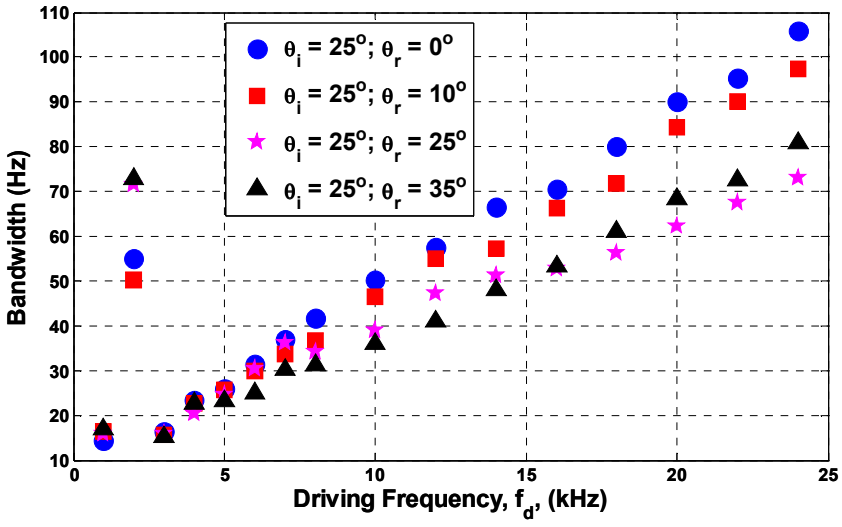

Figure 78. Bandwidth plotted against frequency for four measurement angles. [U_m, S_L, TI] = [3.7 m/s, 0.23 m/s, 5.6%]. (a) θ_i=25° (b) θ_i=45°.

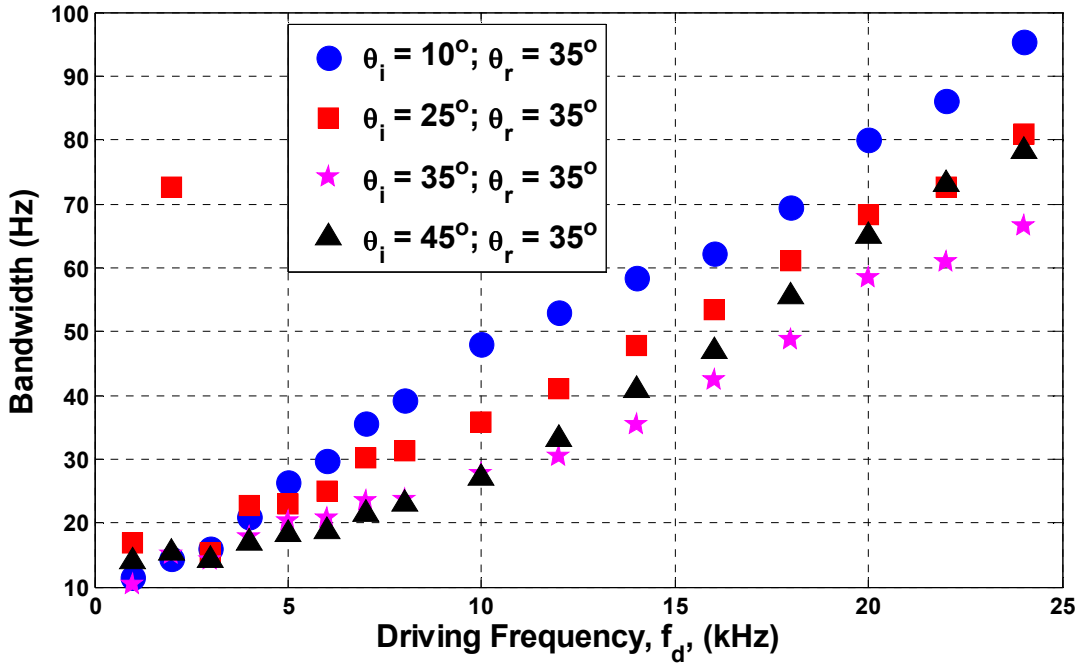

Figure 79. Bandwidth plotted against frequency for four incident angles. [U_m, S_L, TI, θ_r] = [3.7 m/s, 0.23 m/s, 5.6%, 35°].

Figure 79 plots the spectral bandwidth against frequency for multiple incident angles at a fixed measurement angle of 35°. We see that the slopes decrease in general with increase in incident angle. This observed dependence of slopes on angles can be explained based on the Doppler shift equation derived in the introduction chapter and quoted here for convenience:

$$\left\langle \left(f - f_{drive}\right)^2 \right\rangle^{\frac{1}{2}} \approx f_{drive}\left(\cos\theta_i + \cos\theta_r\right)\left(\frac{\left\langle u^2 \right\rangle^{\frac{1}{2}}}{a}\right) \tag{16}$$

This equation suggests that the slope of the bandwidth against frequency plots is dependent on RMS velocity and the incident and measurement angles. The dependence on angles comes from the fact that only the component of velocity of the scattering

surface (in this case, flame front) in the direction of incident and measurement angles is responsible for Doppler shift of the incident wave.

From the equation, we see that the slope of bandwidth against frequency plots is expected to vary linearly with sum of the cosines of the incident and the measurement angles. For this reason, bandwidth is plotted against the product of frequency and the sum of the cosine terms on the right hand side of equation 16, in Figure 80 for the 5.6% turbulence intensity case. This data set includes all the 16 possible (4 incident and 4 measurement angles) combinations of angles and 16 frequencies for each combination.

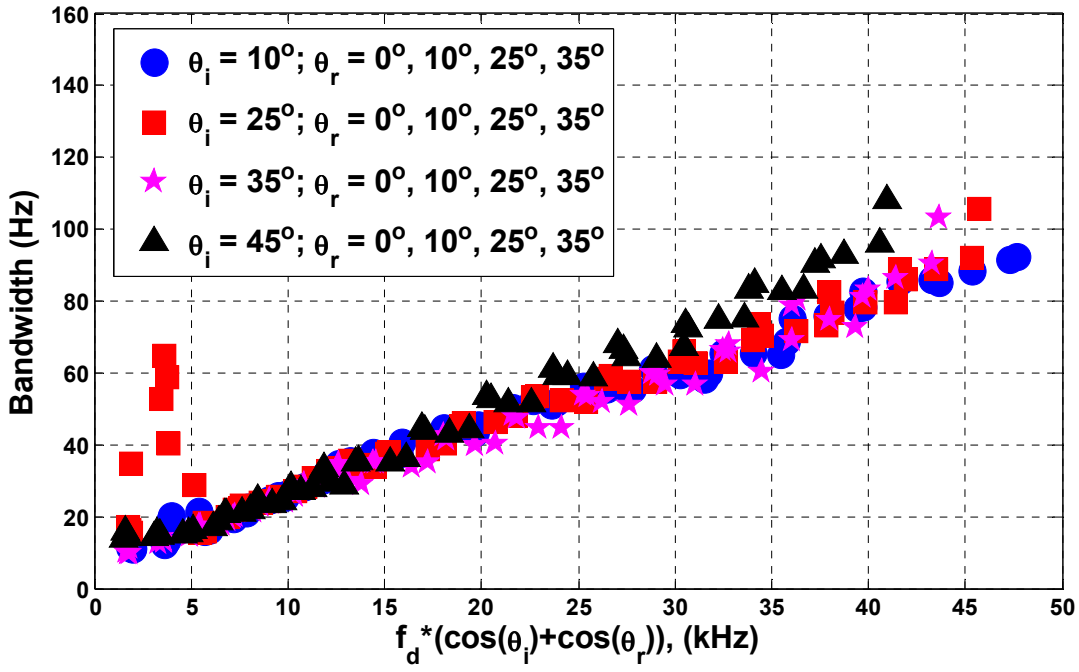

Figure 80. Bandwidth plotted against the product of frequency and the sum of the cosines of the incident and measurement angles for all incident and measurement angles. [U_m, S_L, TI] = [3.7 m/s, 0.23 m/s, 5.6%].

Figure 80 shows that the bandwidth increases in a linear fashion for the whole range of experimental conditions for the given turbulence intensity case, implying the validity of the above mentioned formulation.

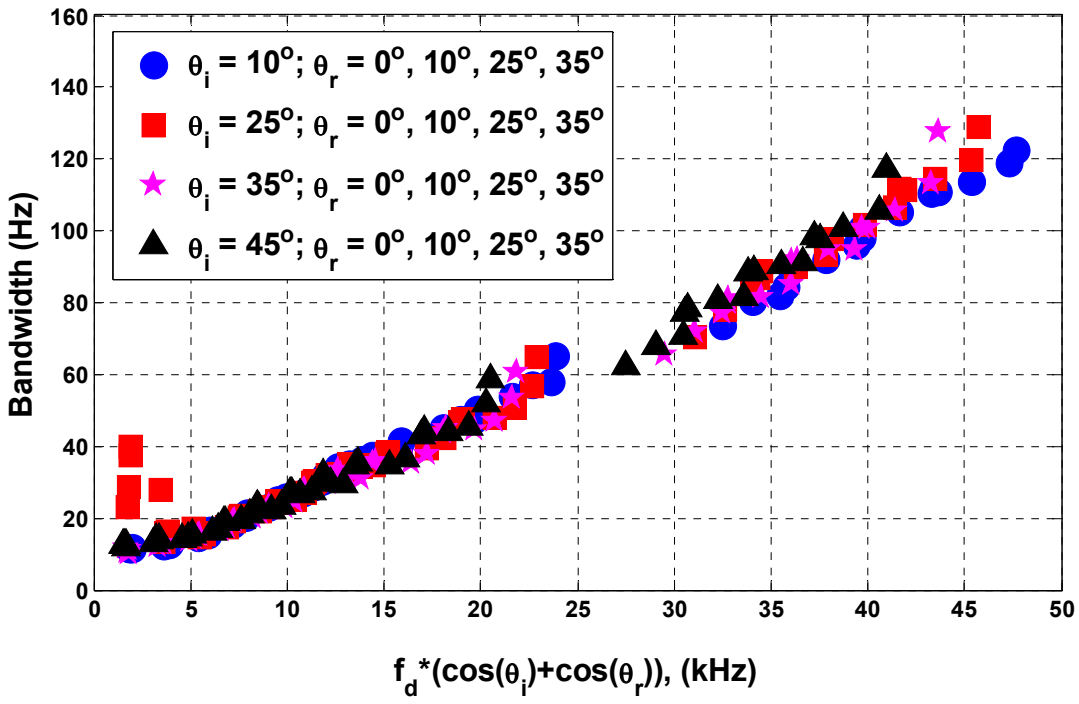

Figure 81. Bandwidth plotted against the product of frequency and the sum of the cosines of the incident and measurement angles for all incident and measurement angles. [U_m, S_L, TI] = [3.7 m/s, 0.23 m/s, 13.4%].

Figure 81 plots bandwidth against product of frequency and sum of the cosines of the incident and measurement angles for the 13.4% turbulence intensity. We see that the bandwidth increases with modified frequency, as expected. Comparing Figure 80 and Figure 81, we see that bandwidth changes from 10 Hz to 100 Hz for 5.6% turbulence intensity and from 10 Hz to 120 Hz for 13.4% turbulence intensity case. As the RMS velocity is increased, range of frequencies over which incoherent power is distributed increases for a fixed incident and measurement angle, which in turn results in higher bandwidth. This variation in slope with turbulence intensity is quantified in Figure 82.

A straight line is fit though the data plotted in Figure 80 to evaluate the slope. Such slopes, obtained for different turbulent intensities, are plotted against turbulence intensities in Figure 82. This plot shows that the slope increases monotonically with

turbulence intensity. This observation suggests that the RMS velocity of the flame front responds in a monotonic fashion to the increased turbulence velocity perturbations over the range of conditions tested here, i.e., u'/S_L from 0.9 to 2.16. Equation (16) implies that the slope should vary linearly with turbulence intensity and should have a zero intercept. However, the plot shown in Figure 82 does not have a zero intercept.

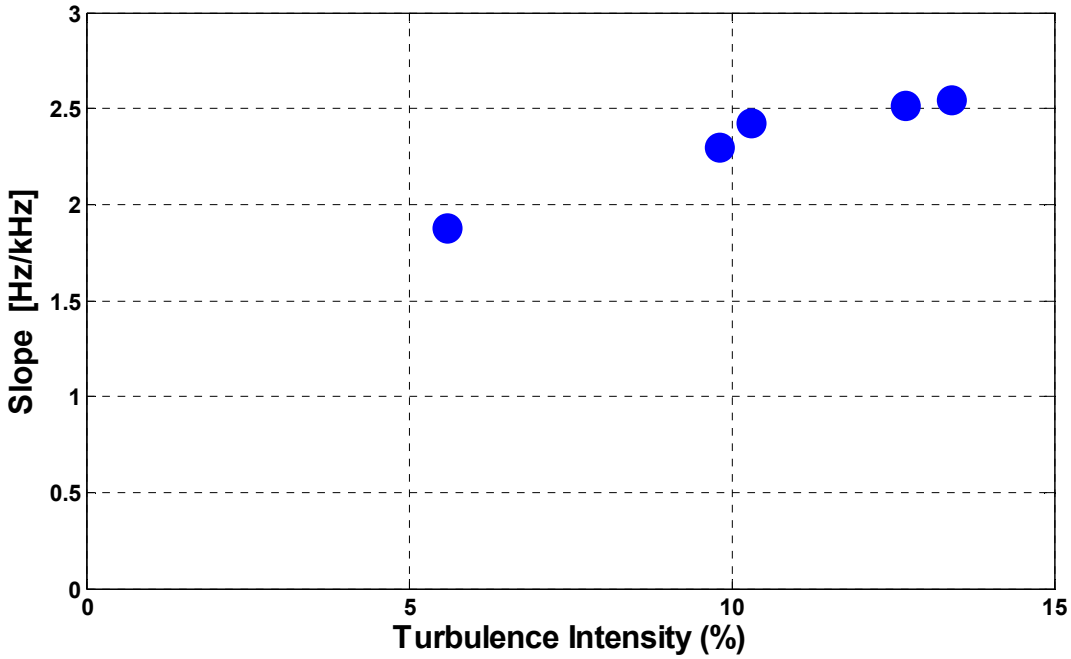

Figure 82. Slopes of bandwidth, as obtained from Figure 80 and Figure 81, plotted against turbulence intensity.

5.3.4 Mean Velocity (U_m) and Flame Speed (S_L)

This section describes the dependence of the scattered acoustic field on mean velocity and flame speed. Experiments were performed for 6 combinations of mean velocity and flame speeds: three mean velocities (3.7, 4.2 and 4.7 m/s) and two flames speeds (0.21 and 0.25 m/s). Incident angle for these experiments is set at 25^o. The four measurement angles chosen for this study are 0^o, 10^o, 25^o and 35^o. Turbulence intensity is 5.6%. For these conditions, u'/S_L varies from 0.82 to 1.24.

The reason for the choosing the lowest turbulence case is this: with increase in turbulence intensity, the flame height (correspondingly, flame area) decreases and with further increase in flame speed, it decreases further leading to a very short flame. For the lowest turbulence intensity case, reported here, flame height is approximately 115 mm and 95 mm for S_L = 0.21 m/s and 0.25 m/s, respectively. Experiments were also performed for 0.32 m/s flame for the three velocities mentioned above. However, the flame height for this case was deemed to be too short (~ 55 mm) and are not reported here.

Figure 83 plots the SPL against driving frequency for two flame speeds at a fixed mean velocity: (a) U_m = 3.7 m/s and (b) U_m = 4.7 m/s. The SPL is seen to increase with increase in flame speed. This trend is observed for both mean velocities.

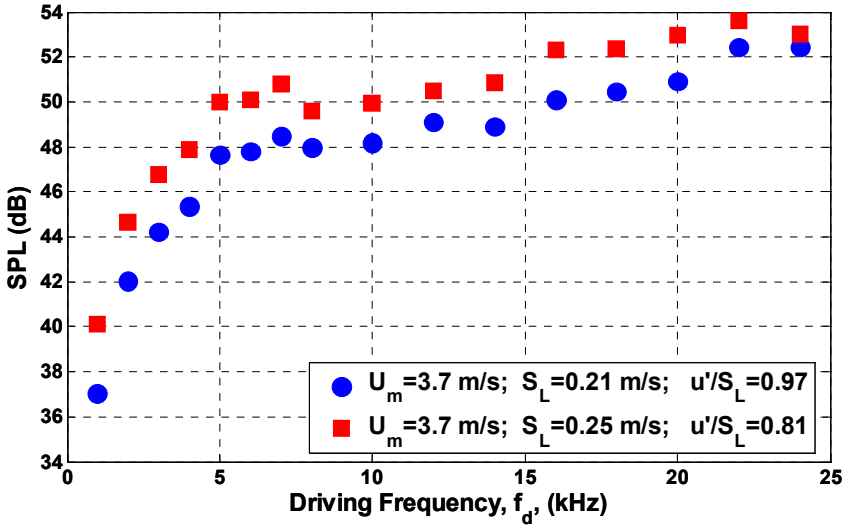

(a)

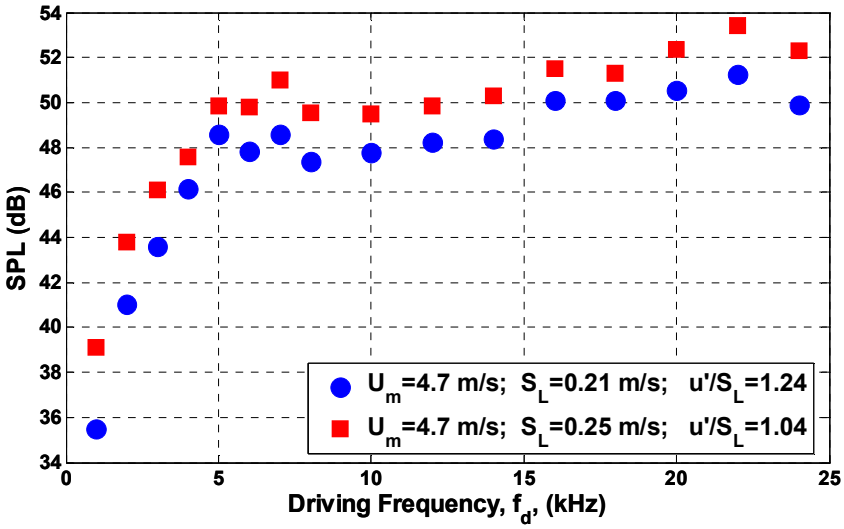

(b)

Figure 83. SPL plotted against frequency for two flame speeds. $[\theta_i, \theta_r] = [25^o, 0^o]$. (a) U_m = 3.7 m/s and (b) U_m = 4.7 m/s.

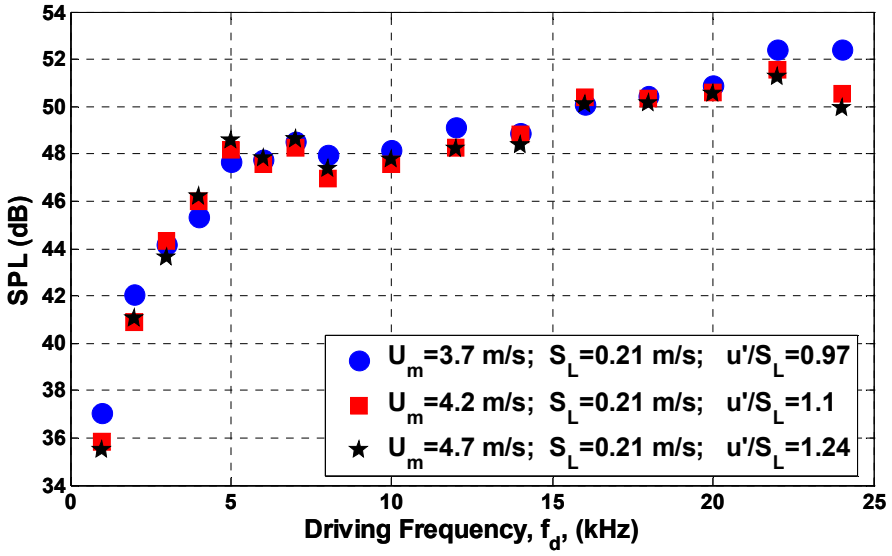

(a)

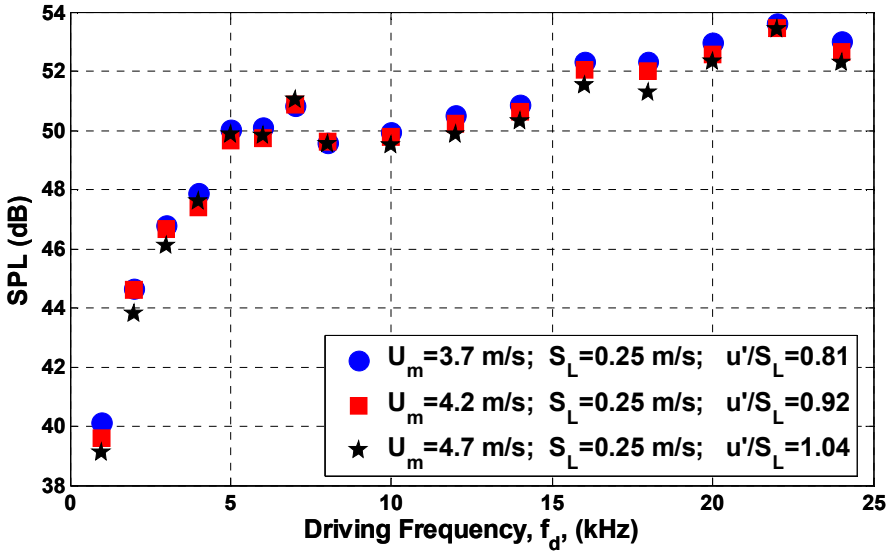

(b)

Figure 84. SPL plotted against driving frequency for three mean velocities. $[\theta_i, \theta_r] = [25^o, 0^o]$. (a) $S_L = 0.21$ m/s and (b) $S_L = 0.25$ m/s.

Figure 84 plots the SPL against driving frequency for three mean velocities at a fixed flame speed: (a) S_L = 0.21 m/s and (b) S_L = 0.25 m/s. There seems to be little influence of mean velocity on the SPL. These observed trends are discussed below.

As pointed out earlier, in this study, flame speed is increased by increasing the equivalence ratio. With increase in equivalence ratio, the adiabatic flame temperature is also increased. The effects of the increase in flame speed and temperature on the parameters that effect scattering are discussed in chapter 1. They are:

(i) Critical angle, $\theta_{crit} = \sin^{-1}\left(\frac{c_r}{c_p}\right)$ (Temperature)

(ii) Impedance ratio of products to reactants, $z=\frac{\rho_p c_p}{\rho_r c_r}$, (Temperature)

(iii) Flame orientation angle distribution (Flame speed)

We will first discuss the role of orientation angle distribution on the average reflection coefficient of the turbulent flame.

In general, the flame front orientation angle distribution has an effect on the average reflection coefficient and the spatial distribution of the scattered acoustic field. Since the change in orientation angle distribution could alter spatial distribution of the scattered field, a better way to quantify the effect of flame speed on reflection coefficient is to compare a quantity more closely related to the totaled scattered power. In essence, the scattered field measured at the four measurement locations (from 0^o to 35^o) are added to get the totaled scattered field. It has to be pointed out that the scattered field does exist beyond these angles, including the backscattering (in the same direction as the source) direction. However, issues such as edge scattering, discussed in Appendix C, interference

of the source, in the backscattering mode, limit the accuracy of the measurements at other angles. So, here, we present results for the range of angles that are available.

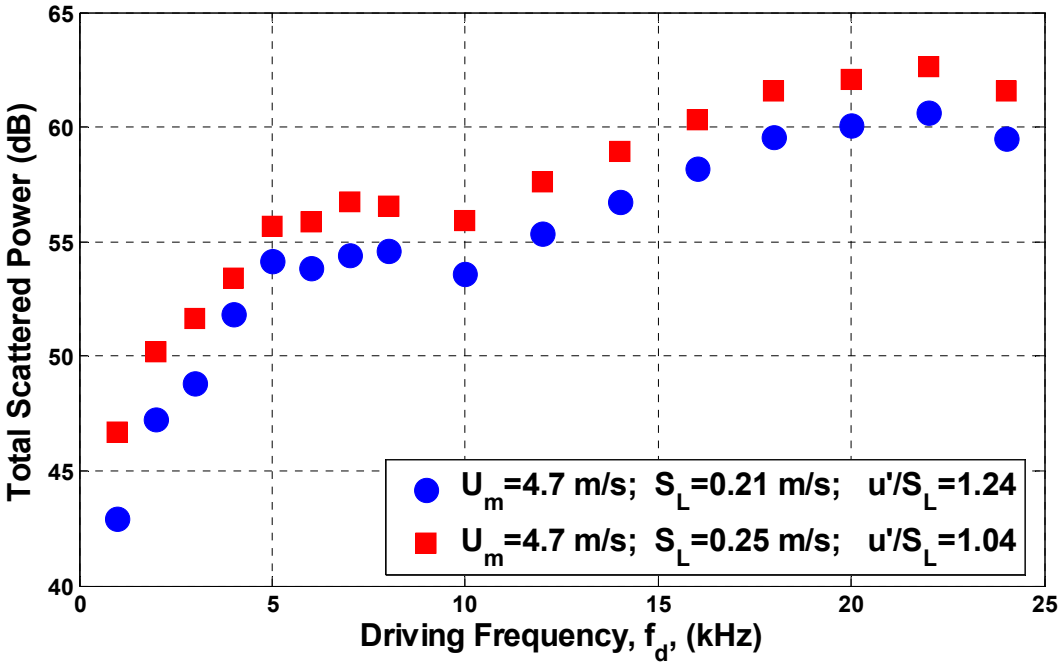

Figure 85. Total incoherent power, quantified as sum of SPLs measured at four measurement locations, plotted against driving frequency for two flame speeds.

Figure 85 plots the sum of the SPL contributions from four measurement locations, against driving frequency for two flame speeds. The higher flame speed case is seen to have approximately 70% more power compared to the lower speed case. Notice from Table 5 that the reflection coefficient for the smooth flame front is unity for both the flame speeds because the incident angle is greater than the critical angle. However, from the discussion in the introduction section, we expect the orientation angle distribution to play a role on the average reflection coefficient of the turbulent flame. This influence of orientation angle is quantified in Figure 86.

Table 5. Smooth flame front properties calculated for two flame speeds for 25^o incident angle. The product gas properties are calculated using the GasEq equilibrium calculation program.

Flame Speed (SL) (m/s)	Temperature Ratio, T_b/T_u	Critical Angle θ_{crit}	Reflection Coefficient $\|R\|$
0.21	6.1	23.2^o	1
0.25	6.5	24^o	1

Figure 86 plots the reflection coefficient against incident angle for four cases:

(i) smooth flame front with a burned to unburned temperature ratio of 6.1, corresponding to 0.21 m/s

(ii) smooth flame front with a burned to unburned temperature ratio of 6.5, corresponding to 0.23 m/s

(iii) turbulent flame front with orientation angle distribution corresponding to 0.17 m/s

(iv) turbulent flame front with orientation angle distribution corresponding to 0.23 m/s

Notice that the orientation angle distributions used in (iii) and (iv) are different from the cases for which acoustic data is presented in Figure 85. However, these are still useful to illustrate the role of the orientation angle distribution. The orientation angle distributions used in (iii) and (iv) above are shown in Figure 87. This figure also highlights the approximate ranges of flame front orientation angles that see local incident angle greater than critical angle.

Figure 86 plots the reflection coefficient for the four cases listed above. First notice that the reflection coefficient increases sharply from 0 to 1 for smooth flame

between approximately 20° and 25°, the angles of intromission and the critical angle, respectively. However, the turbulent flame cases show a relatively smooth variation for the same range of angles. The reason is that the local incident angles for the turbulent flame front occur both below and above the angle of intromission and critical angle.[25] Referring to Figure 86(b), where a detail of Figure 86(a) between angles 20°-30° is shown, we notice that the reflection coefficient for higher flame speed (temperature ratio) is 3% higher compared to the low flame speed case at 25° angle of incidence. However, for angles of incidence less than 25°, notice that the higher flame speed case has a much higher reflection coefficient. This difference is quantified as ratio of reflected power in Figure 88.

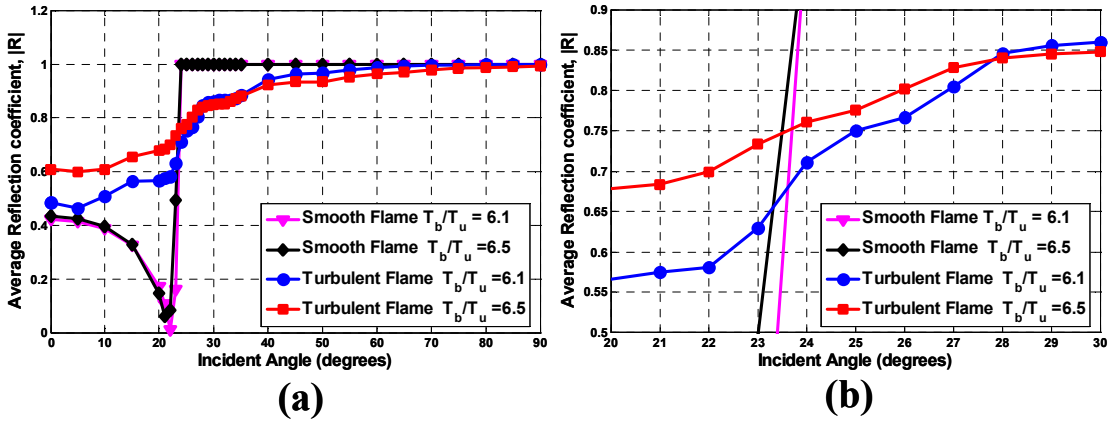

Figure 86. Reflection coefficient plotted against the incident angle for two flame speeds. Part (b) is a close up of part (a). The orientation angle distributions corresponding to S_L=0.17 m/s and 0.23 m/s are used to calculate the turbulent flame reflection coefficient for T_b/T_u = 6.1 and 6.5, respectively. The temperature ratios, T_b/T_u, = 6.1 and 6.5 correspond to flame speeds of 0.21 m/s and 0.25 m/s, respectively.

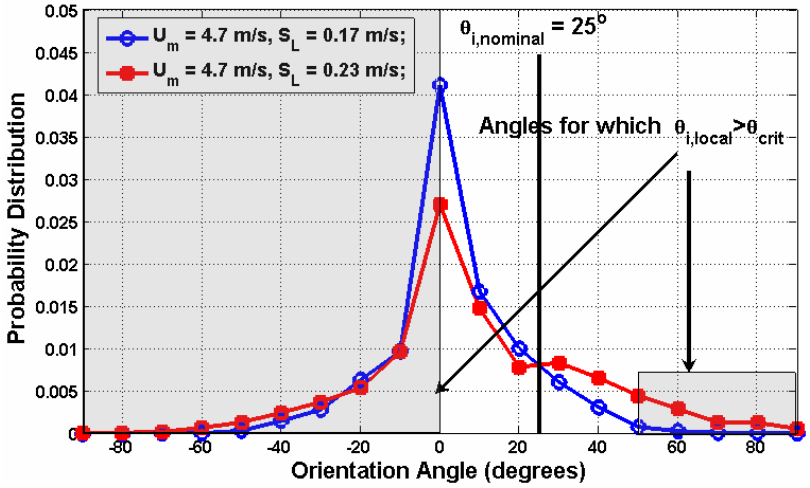

Figure 87. Probability distribution of orientation angles of the flame front, measured in the horizontal plane at 76 mm from the burner exit, for the 5.6% turbulence intensity case. The nominal incident angle and approximate ranges of flame front orientation angles that fall below and above the critical angle are indicated.

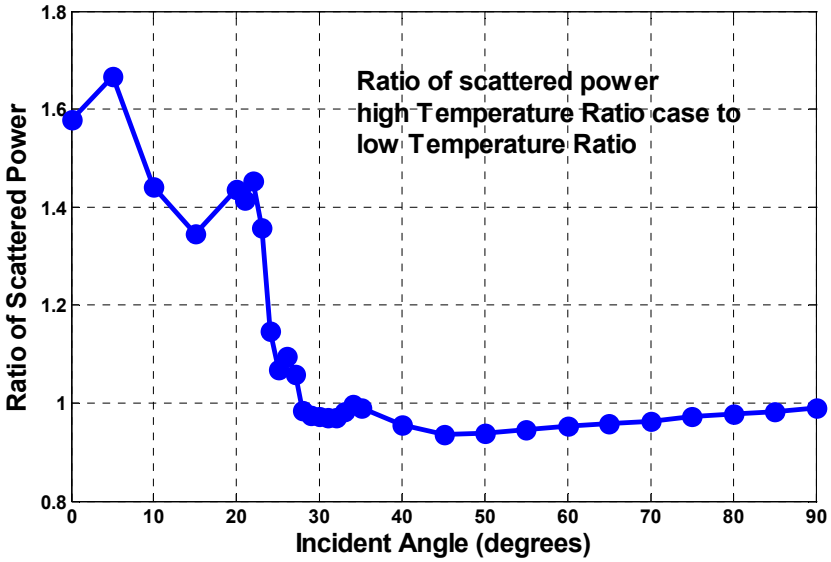

Figure 88. Ratio of high flame speed scattered power to low flame speed scattered power for the turbulent flame case. Scattered power is proportional to square of the reflection coefficient shown in Figure 86.

The ratio of scattered power of the high flame speed to that of the low flame speed is plotted in Figure 88. From Figure 88, we see that the reflected power is approximately 35% higher at 23^o angle of incidence and is about 40% higher at 20^o angle of incidence for the higher flame speed case. This plot suggests that even a small deviation from the nominal angle of incidence of 25^o would lead to large change in the average reflection coefficient and is a possible reason for the observed difference in the scattered power for the two flame speeds.

In this context, it is interesting to look back at the data presented in Figure 74, where SPL is plotted against frequency for four incident angles ($\theta_i = 0^o$, 10^o, 25^o and 35^o) for a fixed measurement angle. We see that the SPL for incident angles corresponding to 35^o and 45^o saturate to a higher value than the 10^o and 25^o incident angle cases in Figure 74. The equivalence ratio for this case is 0.72. The adiabatic temperature, density and sound speed of the products, calculated using GasEq equilibrium calculation program, are 1938 K, 0.175 Kg/m^3 and 844 m/s, respectively. The speed of sound in the reactants, calculated using the room temperature (300 K) and pressure, is 352 m/s. Critical angle is calculated based on these properties of the reactants and products and is found to be 23^o. The incident angles 35^o and 45^o, which saturated to a higher value, are larger than the calculated critical angle. This would mean that the reflection coefficient will be higher for 35^o and 45^o incident angles compared to 10^o and 25^o. Figure 89 further illustrates this argument.

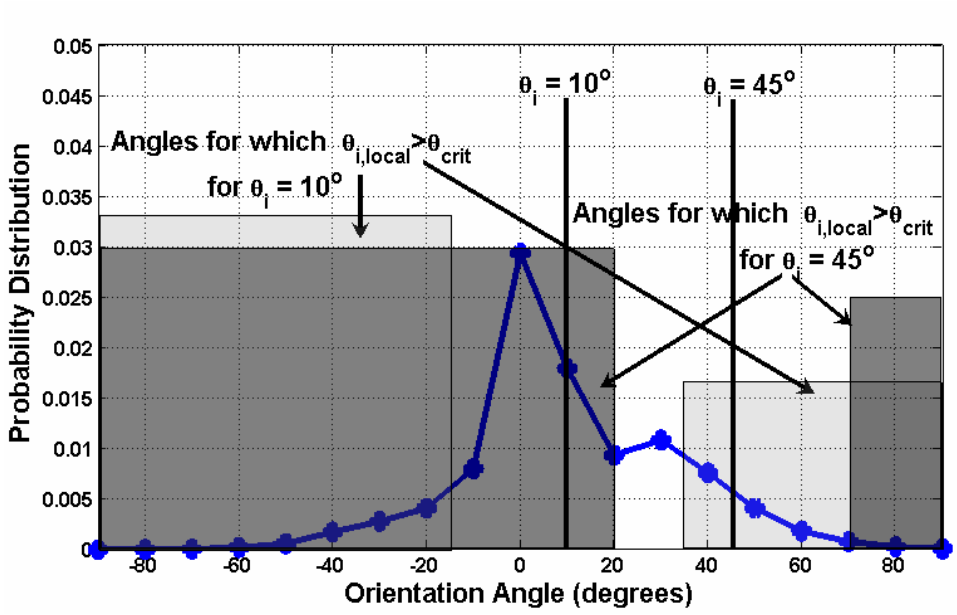

Figure 89. Probability distribution of flame orientation angle, measured in the horizontal plane measured at 76 mm from the burner exit, for same conditions as data presented in Figure 74. The flame orientation angles that see local incident angles greater than critical angle (25°) are highlighted for two incident angles: 10° and 45°. The percentage of angles that sees local incident angle greater than critical angle are 23% and 75% for 10° and 45°, respectively.

Figure 89 plots the probability distribution of the orientation angle for the case where U_m = 3.7 m/s and S_L = 0.23 m/s, same as the data represented in Figure 74. It also indicates the ranges of orientation angles that see local incident angles that are greater than the critical angle for the smallest and the largest nominal incident angles (10° and 45°, respectively). Notice the dramatic change in the probability of seeing a local incident angle greater than the critical angle for the two incident angles. For 10° case, 23% of the orientation angles see local incident angles greater than critical angles while it increases to 75% for 45°. This would mean that the scattered field SPL will increase with incident angle since the effective reflection coefficient has increased. However, this explanation

refers to the total scattered incoherent power and does not exclude the possibility of SPL decreasing with incident angle at a spatial location.

From Figure 84(a) and (b), we see that the SPL plots show minimal change with increase in mean velocity. Note that mean velocity does not change the temperature ratio, incident angle or the flame orientation angle distribution, as shown in chapter 4. From the above arguments, this would mean that there be no change in the SPL with mean velocity. Data presented in Figure 84 confirms argument.

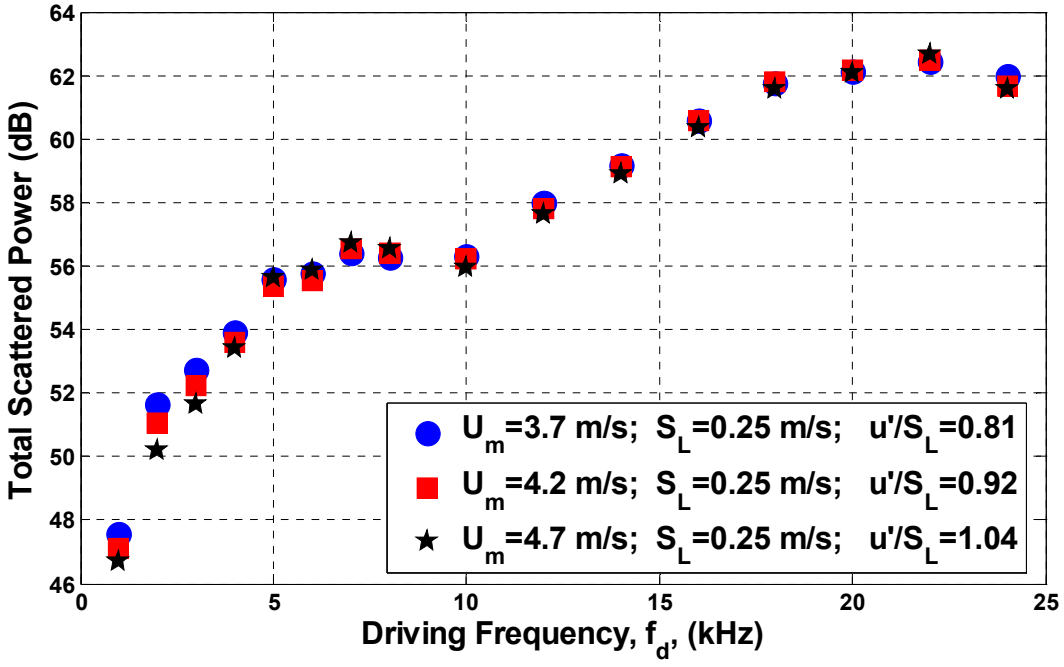

Figure 90. Total incoherent power, quantified here as the sum of SPLs measured at 4 measurement locations, plotted against driving frequency for three mean velocities.

Figure 90 plots the total incoherent power (contribution from all four measurement angles) against driving frequency for three mean velocities at a fixed flame speed. Notice that there is no obvious trend in the incoherent power with mean velocities, confirming the observations from Figure 84.

Figure 91 plots bandwidth against driving frequency for two flame speeds for (a) $U_m = 3.7$ m/s and (b) $U_m = 4.7$ m/s. It can be seen that the bandwidth increases with flame speed. This is not an expected trend because the typical role associated with flame speed is to smooth out the flame front wrinkling caused by the turbulent fluctuations. Thus, for a fixed turbulence intensity and mean velocity, we expect the flame front movement to be diminished with increase in flame speed. That should result in a decreased bandwidth with increased flame speed. However, these results show the opposite trend. In this context, it is interesting to look at the effect of flame speed on flame brush thickness, as discussed in chapter 4. It was seen that the flame brush thickness increased with flame speed suggesting that the role of flame speed is not as straight forward in these interactions. Notice that the bandwidth also increased with turbulence intensity, the parameter that was used to vary the flame brush thickness independent of mean velocity and flame speed. Numerous studies, as reviewed by Lipatnikov and Chomiak[55], have reported the trend of increasing flame brush thickness with flame speed and is an ongoing research problem.

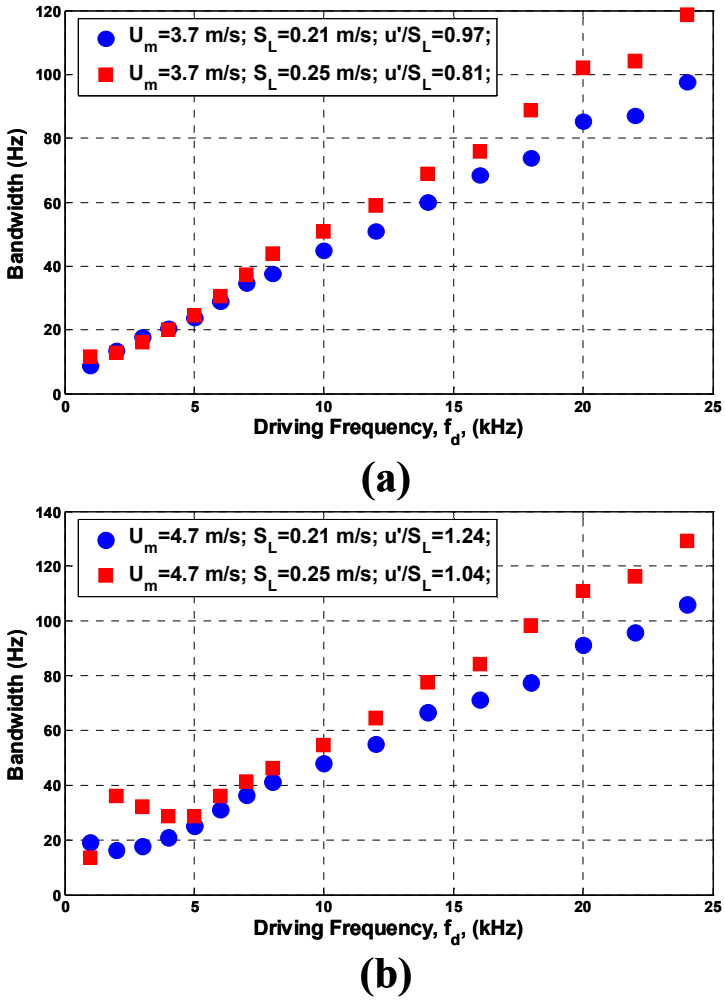

Figure 91. Bandwidth plotted against driving frequency for two flame speeds. $[\theta_i, \theta_r] = [25^o, 0^o]$. (a) U_m = 3.7 m/s and (b) U_m = 4.7 m/s. Experimental conditions are same as in Figure 83.

Figure 92 plots the bandwidth against frequency for multiple mean velocities at a fixed flame speed. This plot shows that there is no significant change in bandwidth with mean velocities, particularly in comparison to the influence of flame speed. Again, it is helpful to revisit the effect of mean velocity on flame brush thickness. Velocity fluctuations increase with mean velocity. However, the balance between the decrease in time available for flame front to interact with eddies, and the increased velocity

fluctuations with increase in mean velocity leads to no change in flame brush thickness. This argument, along with the observation that the bandwidth for flame speed variation behaved like the flame brush thickness, seems to indicate that the flame front movement characteristics are not influenced by the mean velocity for the range of conditions tested here.

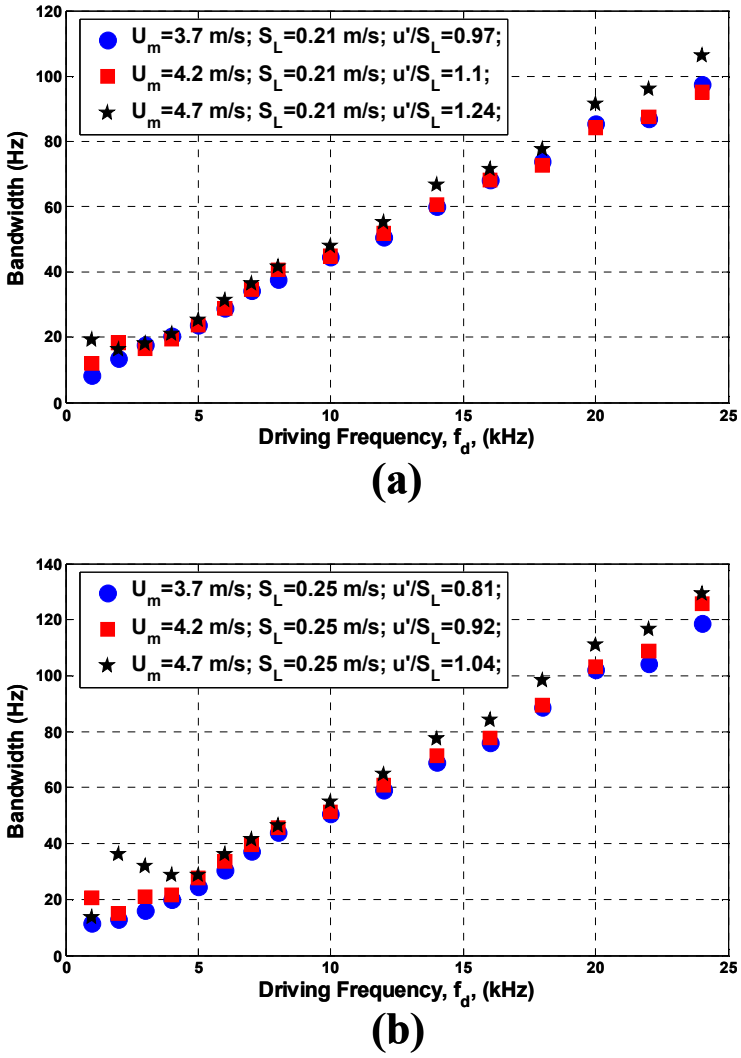

Figure 92. Bandwidth plotted against frequency for multiple mean velocities. $[\theta_i, \theta_r] = [25^o, 0^o]$ (a) $S_L = 0.21$ m/s and (b) $S_L = 0.25$ m/s.

Chapter 6

Conclusions and Recommendations for Future Work

6.1 Conclusions

The objective of this study was to characterize the nature of the scattered incoherent acoustic field from turbulent premixed flames. Frequency (inversely proportional to the wavelength) was varied to study the role of the length scale of the incident acoustic field. Measurements were performed on multiple flames with different flame front characteristics to evaluate the role of flame brush thickness in the scattering process. Incident and measurement angles were varied to determine the spatial variation of the scattered field. Measurements were performed for multiple combinations of flame speeds and mean velocities to study their relative effects on the flame front movement.

The measured scattered acoustic field power spectra showed distinct incoherent spectral sidebands on either side of the driving frequency. The strength of the incoherent field, quantified as SPL, was found to increase at low frequencies and saturate at high frequencies. This result suggested that the random movement of the turbulent flame acts as a source of damping at the incident acoustic wave frequency. Since the random flame front movement is the key to this mechanism, such a mechanism will play any role in the laminar flame - acoustic wave interactions. In addition, these results indicate that the wavelength of the incident acoustic wave is an important parameter in these interactions. The saturation characteristics of the SPL, such as the saturation frequency, were observed

to change with the incident and measurement angles. The normalized SPL plotted against the wave vector normal to the flame front for 16 combinations of incident and measurement angles were similar. This result further confirmed wavelength as a key parameter in these interactions. These results are in agreement with the theoretical analysis based on infinite, weakly wrinkled, statistically homogeneous turbulent flame.

The bandwidth of the incoherent field spectra was observed to increase monotonically with frequency. This result suggested that these interactions are governed by a phase modulation process. The spectral bandwidth was observed to decrease with increase in incident and/or measurement angles. These results are in agreement with the predictions from Doppler shift arguments, further confirming phase modulation as a key process in these interactions.

The saturation characteristics of the scattered field did not change with flame brush thickness. However, the measurements in the far field, as is the case here, reflect the scattered field averaged over the surface of the developing flame and could be the reason for the observed independence with flame brush thickness. While the spectral bandwidth increased with turbulence intensity, the observed change was small compared to the change in turbulence intensity.

The scattered incoherent power was observed to depend strongly on the flame speed (equivalence ratio). Reflected power for the higher temperature ratio (higher equivalence ratio) case, calculated based on the orientation angle distribution in the horizontal plane, was found to be 40% higher at incident angles close to the experimental case. The change in the orientation angle distribution with equivalence ratio was seen to have large effect on the average reflection coefficient compared to the change in

adiabatic temperature. Spectral bandwidth was observed to increase with flame speed. This trend reflected the increase in flame brush thickness with flame speed. For a fixed flame speed, variation in mean velocity did not have any appreciable influence on the scattered field power or the bandwidth. The parameters which affect the scattering process, temperature ratio across the flame front, critical angle and the orientation angle distribution were observed not to change with mean velocity.

6.2 Recommendations

The following recommendations discuss the various improvements to this study that will help gain further understanding of these interactions.

This study has focused on the far field characteristics of the scattered incoherent field. The role of the frequency (inversely proportional to wavelength) in these interactions has been identified. The result that the saturation characteristics were dependent on the wave vector normal to the flame front further implied that the wavelength is a key parameter in these interactions.

However, the role of the flame front wrinkling scale, i.e., flame brush thickness, was observed to be qualitatively different to that of the wavelength. The increase in flame brush thickness was expected to enhance the energy transfer from the coherent field to the incoherent field. However the saturation characteristics of the scattered field did not suggest any such dependence on flame brush thickness. This behavior warrants further investigation. In addition, while the spectral bandwidth was observed to increase with turbulence intensity, the magnitude of variation was small compared to the change in the velocity fluctuations. Direct flame front velocity measurements at different turbulent

intensities could help explain the observed dependence of the bandwidth on turbulence intensity.

In this thesis, the observed dependence of spectral bandwidth on frequency and the incident and measurement angles was quantitatively compared to the predictions based on the Doppler shift effect. However, the behavior of the incoherent field strength, SPL, was compared only qualitatively with the theoretical predictions. For example, theoretical analysis suggests a quadratic dependence for incoherent power on frequency. The measured incoherent SPL showed a power law dependence on frequency at low frequencies. The exponent of this power law has not been confirmed to be two. Such quantitative comparison requires addressing the role of finite and the spatially evolving nature of the flame front in the experiments.

The average reflection coefficient was calculated for two flame speeds based on the orientation angle distribution in the horizontal plane. This calculation assumed that the orientation angle distribution in the vertical plane and the horizontal plane were uncorrelated. The orientation angle in the vertical plane influences the spatial distribution of the field in the vertical plane and any correlation between the vertical and horizontal angle distributions would thus influence the spatial variation in the horizontal plane too. Detailed characterization of the flame front, such as flame front normal distribution will reveal the relationship between the orientation angle distributions. In addition, the average reflection coefficient has been evaluated based on a single scattering assumption. However, for highly wrinkled flames this assumption is not valid and needs to be addressed. Furthermore, with increase in flame speed, the temperature gradient in the reaction zone is expected to change. Thus the intensity threshold used to determine the

edges from the cross-sectional images refers to different locations in the flame front at different flame speeds. The effect of this variation on the flame front statistics and the corresponding effect on the scattering process need to be addressed.

In this study, distinction has been made between the true edge and the single valued edge statistics. These two cases represent two extremes in terms of the contribution from the "shadowed" flame front. A better approach in the context of reflection coefficient calculation would be to consider a distribution midway between the cases, depending on the incident angle. For example, orientations corresponding to the "shadowed" flame front could be included if the flame-let is oriented within 90^{o} of the incident angle.

At low frequencies, from the existing theory, the scattered field spectra are expected to be directly related to the flame front movement spectra. The observation that the measured scattered incoherent field dependence on frequency is predicted by the theory supports the possibility of using the scattered field measurements as a diagnostic tool to estimate the flame front characteristics such as the flame front movement spectrum. However, flame front velocity measurements need to be performed to verify the feasibility of such a technique.

Appendix A

Data Reduction

A.1 Estimation of the Scattered Field Acoustic Spectrum

Power spectra of the measured data were obtained using a standard Fast Fourier transform algorithm. Special care was taken in determining the number of data points taken and the sampling frequency in order to minimize bias errors and uncertainty in these spectral estimates, while still retaining good spectral resolution. Bias errors arise from spectral leakage[61], which was a particular concern in this study because of the need to measure potentially low amplitude, distributed frequency sidebands in the immediate vicinity (i.e., within 1 Hz) of large amplitude, narrow band coherent oscillations. Because of leakage, spectral estimates of these narrow band oscillations also contain slowly decaying nonphysical sidebands which can easily swamp out the incoherent sidebands of interest.

Leakage-induced bias errors were minimized by using large data record lengths and/or multiplying the data record by window functions.[61] A competing requirement, however, is the need for ensemble averaging to minimize the variance of the spectral estimate. This procedure reduces the standard deviation by the square root of the number of ensembles. However, it also decreases the size of each data record, thereby reducing spectral resolution and increasing bias error.

Data were acquired at 50 kHz sampling frequency for 100 seconds. These conditions correspond to 5 million data points (N_T) for each test case. The data is divided into 200 non-overlapping ensembles (N_e) with a resolution of 2 Hz ($= N_e f_{sample} / N_T$). The

standard deviation of the spectral estimate at each point is approximately $1/\sqrt{200} \approx 7\%$. Bias errors due to spectral leakage of the nearly discrete, coherent peak were made negligible by carefully aligning the sampling and driving frequencies such that

$$f_{drive} = jN_e f_{sample} / N_T \tag{17}$$

where j is an integer. For example, spectral estimates of data taken with only the transducer on at f_d = 18 kHz, see Figure 60, indicated that the SPL at 17998 Hz was 50 dB lower than at 18000 Hz. In comparison, the relative SPLs at these two frequencies differ by 30 dB when the flame and transducer are both on, indicating that bias errors due to spectral leakage from the coherent peak are less than 0.1%. Because leakage from the coherent peak is negligible, the resultant dominant source of bias error arises through leakage from one part of the distributed frequency, incoherent component to others. However, the total incoherent power is sum of all the incoherent components and thus is independent of leakage from one incoherent component to another.

A.2 Incoherent SPL

The area under the spectra is quantified as sound pressure level (SPL). First, the area contained between the background combustion noise spectrum and the case when both the flame and the transducer are on is determined, excluding the coherent peak at f = f_d. It is shown in Figure 93 as shaded area. Then SPL is determined using the following expression:

$$SPL = 10\log_{10}\frac{\overline{p'^2}}{p_{ref}^2} \tag{18}$$

where $\overline{p'^2}$ is the shaded area in Figure 93 and p_{ref} is 20 μPa.

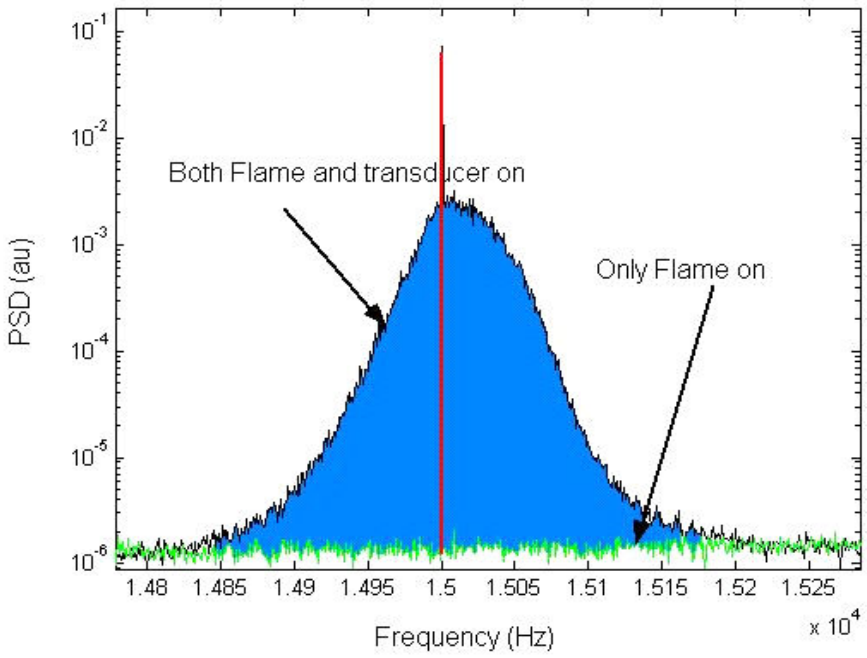

Figure 93. Scattered field spectrum for 15 kHz driving frequency. SPL is the area contained between the background combustion noise spectrum and both the flame and transducer on case, indicated by the shaded area. The coherent peak at the driving frequency is excluded in the estimation of SPL.

Appendix B

Error Analysis

This section closely follows the analysis performed in Ref. [62].

First, all the individual uncertainty factors from different components are considered. Then, the total uncertainty in the measurement system is estimated.

The combined uncertainty in the measurement system is due to the following factors:

1. Influence of Microphone Calibration

   The microphone calibrator had an uncertainty of ±0.3 dB @ 95% probability (implying a 2σ).

   $u_{calibrator} = 0.15\,dB$

2. Influence of Microphone Response

   The microphone manufacturers, Bruel & Kjaer, report 2 dB uncertainty with 95% confidence for the 4939(1/4" microphone).

   $u_{microphone} = 1\,dB$

3. Influence of Filter Response

   The uncertainty for the Krohn-Hite filter was assumed to be 0.21 dB. However the filter was used for both the high pass and low pass filtering of the signal. Hence uncertainty of the filter has to be accounted twice in the final analysis.

   $u_{filter} = 0.21\,dB$

4. Influence of Microphone positioning

   The position of the microphones was measured using a measuring tape. The uncertainty in the measurement of the distance between the microphone and the

burner was estimated to be ±6.4 mm. Since the microphones were placed at a distance of 1.02 m from the burner, the uncertainty in the acoustic measurement assuming the square law:

$$u_{microhonePosition} = 20\log_{10}\left(\frac{1016+6.4}{1016}\right) dB = 0.05\, dB$$

5. Influence of Finite Fourier Transform

   First, data is divided into 200 non-overlapping bins. Then the spectra are estimated from each bin and then averaged. The uncertainty at each frequency location is:

$$u_{FFT} = 20\log_{10}\left(1+\frac{1}{\sqrt{200}}\right) = 0.59\, dB$$

   The spectral leakage from the coherent peak is less than 0.1% and is not included in the calculation.

The combined uncertainty of the measurement due to all its factors is given by:

$$u_c^2 = u_{calibrator}^2 + u_{microphone}^2 + 2u_{filter}^2 + u_{microphoneposition}^2 + u_{FFT}^2$$

For the 4939 microphone the combined uncertainty is:

$$u_{combined} = \left(0.15^2 + 1^2 + 2\times 0.21^2 + 0.05^2 + 0.59^2\right)^{\frac{1}{2}} = 1.21\, dB$$

In order to estimate the uncertainty at 95% probability we have to multiply a factor of 2 to these uncertainties, if we assume the underlying distribution of uncertainty to be Gaussian. Therefore the combined uncertainty of the microphones is given by:

$$u_{combined,95\%} = 2.42\, dB$$

Appendix C

Edge Scattering Estimation

Because of the finite size of the scattering cross-section (turbulent flame in this study), the diffraction from edges is expected to contribute to the scattered field. This section presents a formulation to estimate the contribution of the edge scattering to the total scattered field. First, an analytical formulation is presented. Next, analytical results for a smooth surface are discussed. Finally, the results from a numerical simulation of scattering from a rough surface are presented.

The formulation presented here closely follows the analysis performed in Refs [63,64]. In this formulation, the scattering surface is treated as a series of point sources. The amplitude of each point source is determined by the local surface gradient through the local reflection coefficient which is in turn dependent on the local incident angle. The phase is determined by the local height.

The following assumptions are made to for the analysis:

(i) Kirchhoff theory is valid for approximating the field on the surface of the scatter

(ii) Observation point is in the far field

(iii) Incident wave is planar and monochromatic

(iv) The surface gradients are small

The co-ordinate system considered for this analysis is illustrated in Figure 94. The incoming wave is incident at an angle of θ_I to the z-axis. The observation point, P, is in

the far field at a distance r from the surface and is inclined at an angle θ_2 to the z-axis and the projection of the vector makes an angle θ_3 with the x-axis.

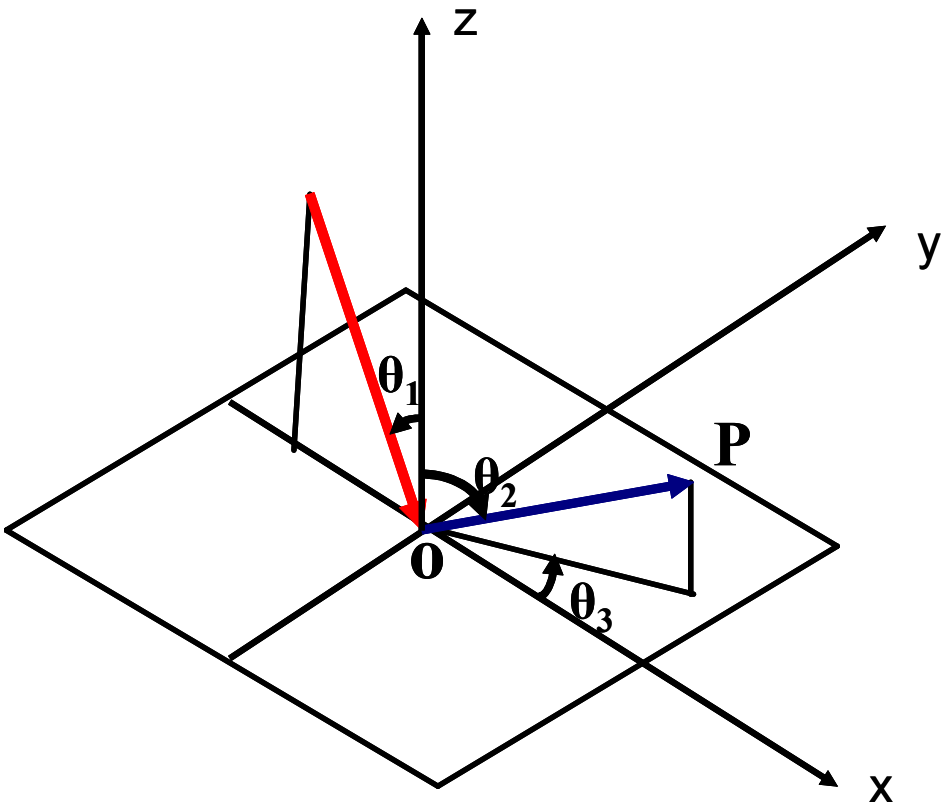

Figure 94. Scattering geometry considered in the formulation.

The scattered field at the observation point is given by:

$$\psi_{sc} = \frac{e^{ikr}}{r}\iint_S \left(a\frac{\partial h}{\partial x} + b\frac{\partial h}{\partial y} - c \right) e^{ik[Ax+By+Ch(x,y)]}dxdy \tag{19}$$

The quantities in the equation are defined as follows:

$$A = \sin\theta_1 - \sin\theta_2 \cos\theta_3$$
$$B = -\sin\theta_2 \sin\theta_1$$
$$C = -(\cos\theta_1 + \cos\theta_2)$$
$$a = \sin\theta_1(1 - R_o) + \sin\theta_2 \cos\theta_3(1 + R_o)$$
$$b = \sin\theta_2 \sin\theta_3(1 + R_o)$$
$$c = \cos\theta_2(1 + R_o) - \cos\theta_1(1 - R_o)$$

The quantities *h(x, y), Ro* are the height at the surface point *(x, y)* and the reflection coefficient, respectively.

In the above expression, the term the bracket inside the integral is related to the amplitude of the point source and the exponential term is related to the phase. For a rectangular surface extending from –X to +X and –Y to +Y, the above integral can be simplified into sum of two integrals:

$$\psi_{surface} = -\frac{e^{ikr}}{r}\left(\frac{Aa}{C} + \frac{Bb}{C} + c\right)\iint_S e^{ik[Ax+By+Ch(x,y)]}dxdy \tag{20}$$

$$\psi_{edge} = \frac{e^{ikr}}{krC}\left(a\int_{-Y}^{Y} e^{ik[Ax+By+ch(x,y)]}dy + b\int_{-X}^{X} e^{ik[Ax+By+Ch(x,y)]}dx\right) \tag{21}$$

$\psi_{surface}$, which involves integration over the surface, is the contribution from the surface and ψ_{edge}, which involves integration over the edges of the surface is the contribution form the surface edge contribution.

For a smooth surface with *Ro* = 1, the equations can be further simplified to the following form:

$$\psi_{surface} = -\frac{e^{ikr}}{r}\left(\frac{Aa}{C} + \frac{Bb}{C} + c\right)A_m\left(\frac{\sin kAX}{kAX}\right)\left(\frac{\sin kBY}{kBY}\right) \tag{22}$$

$$\psi_{edge} = \frac{e^{ikr}}{r}\left(\frac{Aa}{C} + \frac{Bb}{C}\right)A_m\left(\frac{\sin kAX}{kAX}\right)\left(\frac{\sin kBY}{kBY}\right) \tag{23}$$

where A_m= 4XY, is the surface area of the scatterer.

Figure 95 plots the ratio of edge power to the total power against measurement angle for a range of incident angles, for a 15 cm X 15 cm smooth surface, obtained from the equation (22) and (23). These measurements were evaluated for θ_3=0; i.e., in the x-z plane, see Figure 94. For measurements in the x-z plane, θ_1 is the incident angle and θ_2 is the measurement angle.

From Figure 95, we see that the edge contribution is less than 10% for measurement angles less than 45^o for all incident angles.

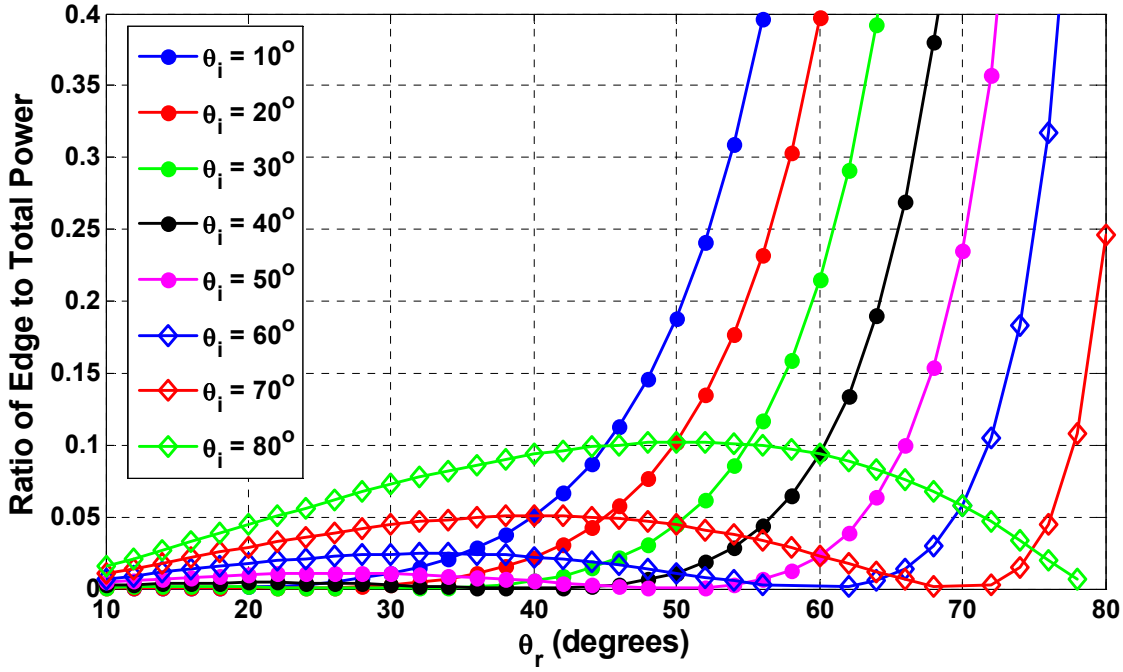

Figure 95. Ratio of the edge power to total power plotted against measurement angle for multiple incident angles.

Next we present the results from a numerical simulation for scattering from a rough surface. First, 200 rough surface realization, such as shown in Figure 96, are

generated from flame edges obtained from flame images, as discussed in chapter 4. Then the two components of the scattered field, the edge component and the surface component, are evaluated for *Ro*=1 condition for each surface by numerically integrating equations (20) and (21). Then the ratio of the edge contribution to the surface contribution is ensemble averaged over the 200 realizations.

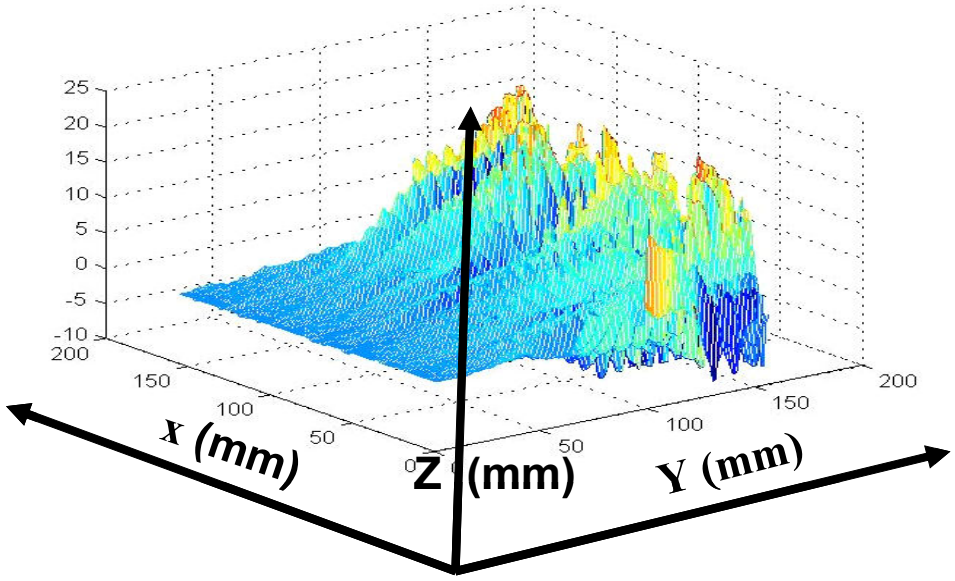

Figure 96. Typical rough surface generated from the flame edges.

Figure 97 plots the ratio of edge power to the total power against measurement angle for the smooth surface case, from the analytical solution, and the rough surface, from numerical integration of equations (20) and (21). Results were plotted for 4 incident angles. For small measurement angles, see that the behavior of the rough surface is similar to that of the smooth surface. The contribution from the edge scattering is less than 10% for measurement angles less than 45^{o}.

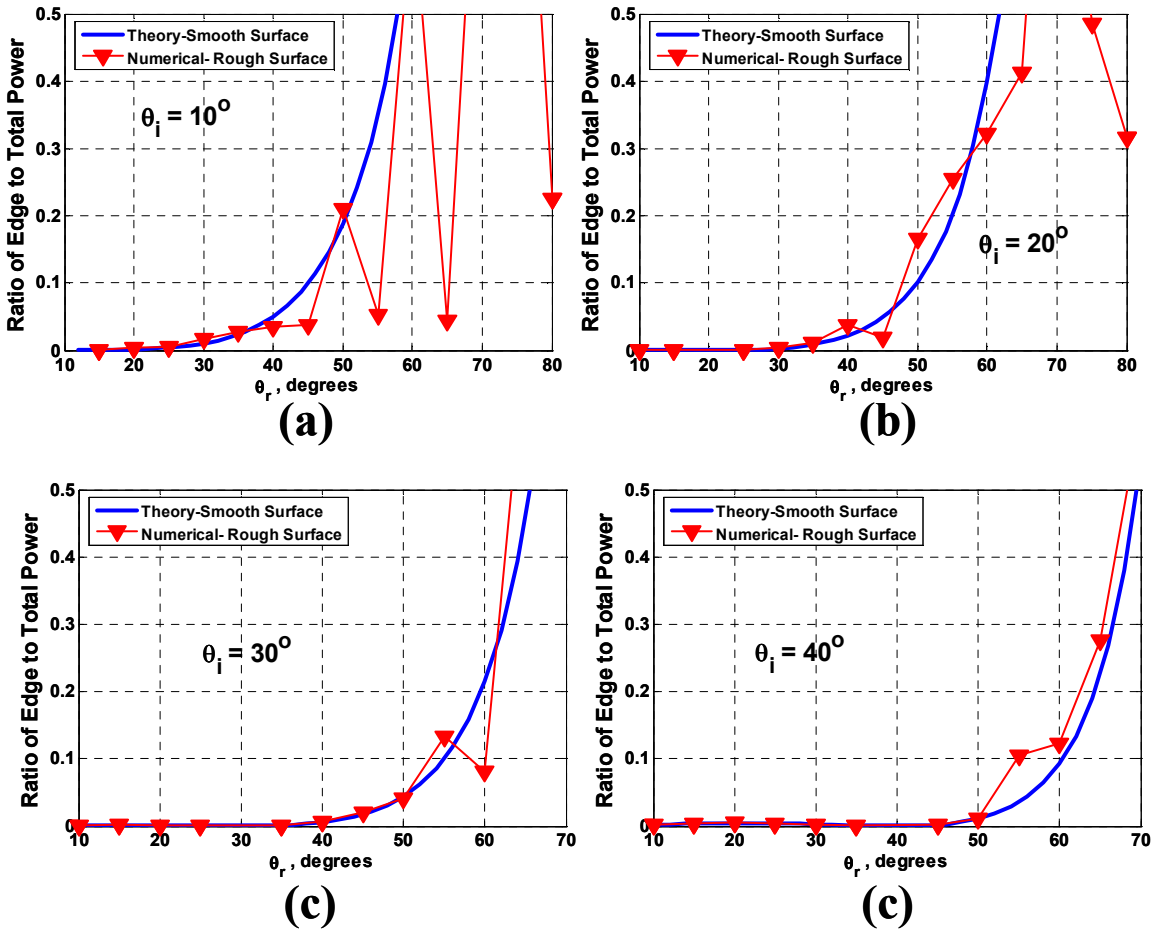

Figure 97. Ratio of the edge power to total power plotted against measurement angle for smooth surface and the rough surface for (a) $\theta_i = 10^o$ (b) $\theta_i = 20^o$ (c) $\theta_i = 30^o$ and (d) $\theta_i = 40^o$.

Appendix D

Further Description of Acoustic Measurement Techniques

D.1 Far Field Estimation

Experiments were performed to determine the far field location for the scattered acoustic field from the flame. In the acoustic far field, the acoustic power follows the inverse square law with distance. Experiments were performed to evaluate this distance. The source was fixed at 61 cm from the midpoint of the flame. The microphone was traversed from 56 cm to 102 cm in steps of approximately 5 cm. Figure 98 plots the spectra measured at five locations. The spectra are displaced vertically for clarity and for this reason only qualitatively described. Notice that the shape of the spectra changes from 55 cm to 66 cm and again to 76 cm while it remains the same for 76 cm, 86 cm and 96 cm locations indicating convergence toward a "final" spectrum. The variation in the scattered incoherent SPL with distance is quantified in Figure 99.

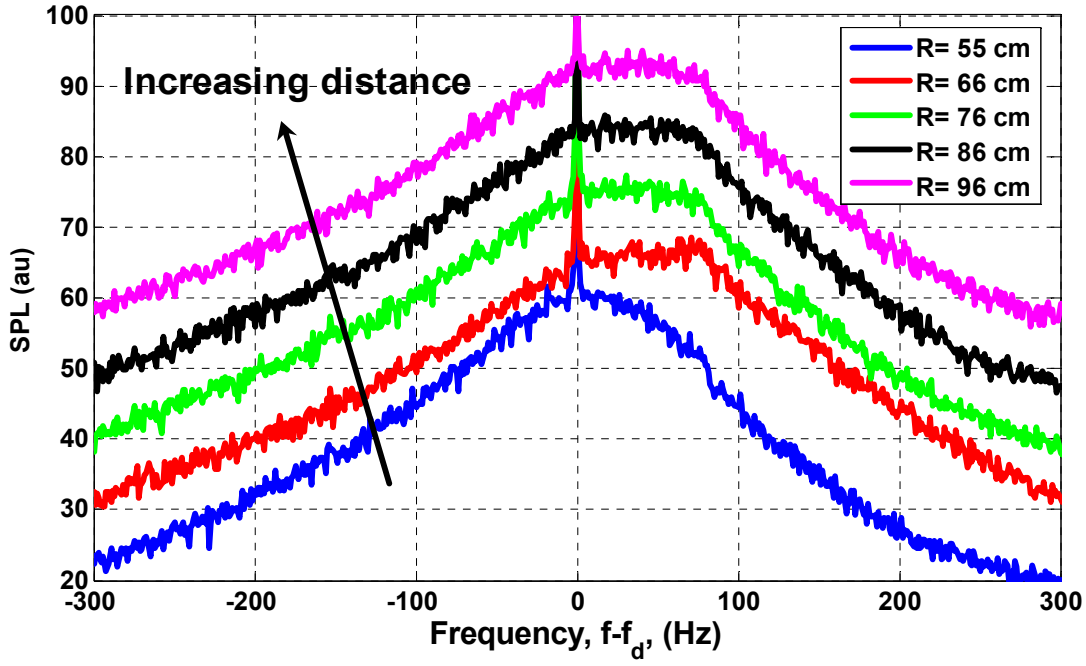

Figure 98. Scattered field spectra measured for 20 kHz driving frequency case at 5 locations away from the flame (56 cm to 96 cm in steps of approximately 10 cm).

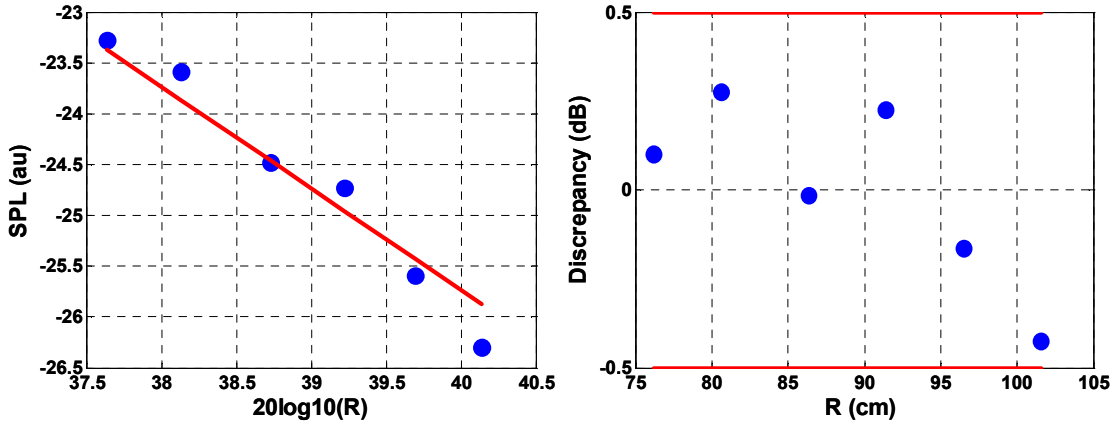

Figure 99. (a) Measured SPL plotted against distance. The solid line corresponds the expected behavior from the $1/R^2$ law. (b) Deviation from $1/R^2$ plotted against distance.

Figure 99 (a) plots the SPL against the distance on a log-log scale for 20 kHz driving frequency. It is compared with the expected variation according to the $1/R^2$ law, which is valid in the far field. Figure 99(b) plots the deviation of measured SPL against the distance from the burner. Only data points from 76 cm to 100 cm were considered because measurements closer to the flame do not follow the $1/R^2$ law and for this reason the deviation appears larger than it actually is. The deviation from the $1/R^2$ law is with in 0.5 dB, which is in accordance with ISO 3745 standard[65].

Analysis was made for 4 to 40 kHz in steps of 4 kHz and they show trends similar to that of 20 kHz. These results suggest that the locations beyond 76 cm from the flame front can be considered as far field with respect to the scattered field.

D.2 Source Response at Various Driving Voltages

Figure 100 plots the response of the source against frequency for four driving voltages. The measurements were performed using the set up shown in Figure 9. The measured amplitude increases with driving voltage. Figure 100(b) plots the measured amplitude divide by the driving voltage. The four response curves collapse, suggesting that the source response is linear over the 100 mV to 1000 mV range. The variation between the responses after correcting for driving voltage was found to be less than 0.1%.

Figure 101 plots the measured response against the driving voltage for multiple driving frequencies. As already shown in Figure 100(b), the response is linear. The scattering experiments reported in this study were performed for a driving voltage corresponding to 700 mV, indicated by the vertical line in Figure 101.

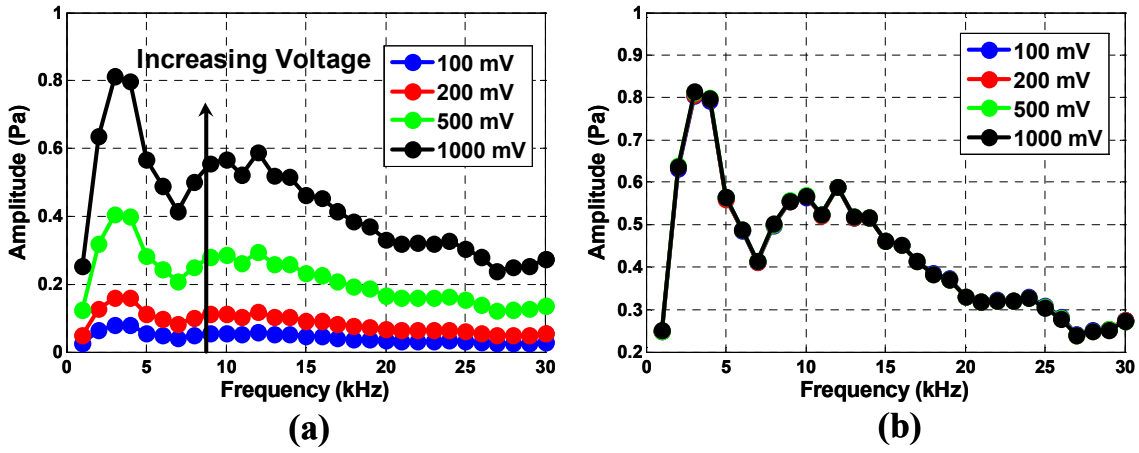

Figure 100. (a) Response of the acoustic source at four driving voltages (b) Response of the source divided by the driving voltage.

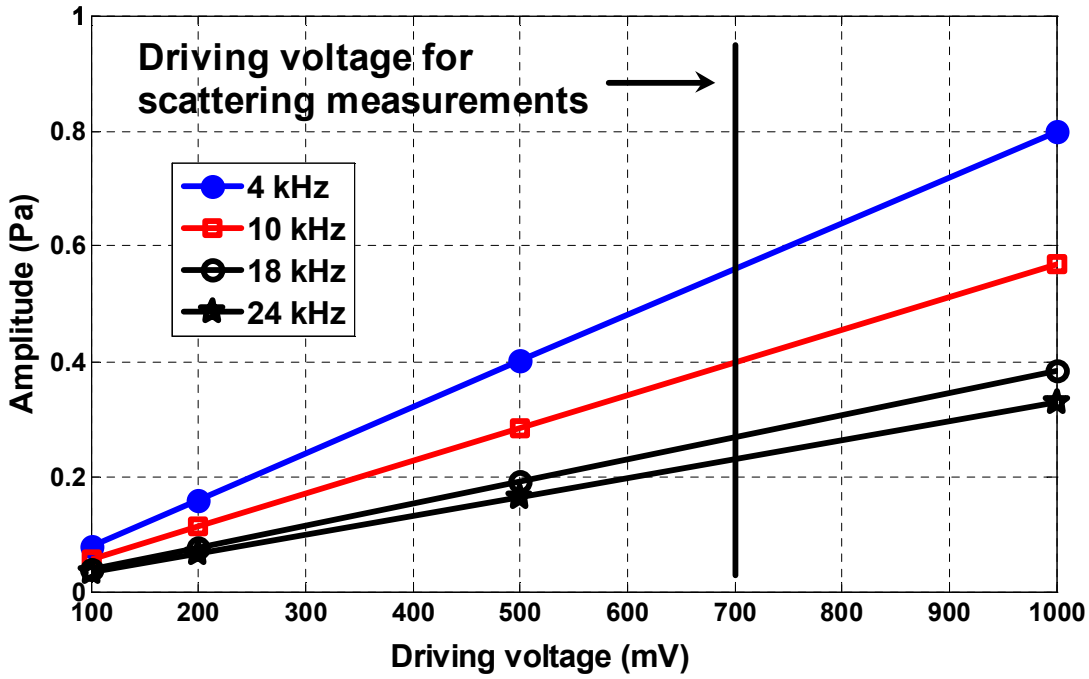

Figure 101. Response of the source plotted against driving voltage for four frequencies. The Vertical line corresponds to the voltage used to drive the source during the scattering experiments.

Appendix E

Scatter Field from Cold Jet and Other Experimental Configurations

In this appendix, first the scattered field from a cold jet of reactants, pilot flame and the turbulent flame are compared. The purpose of this exercise is to show that the contribution from the cold flow and pilot flame are negligible compared to the turbulent flame.

Then, measurements with the acoustic instrumentation placed on the products side are presented. These measurements were used to ascertain the origin of the 20 Hz peak observed in the incoherent sidebands.

E.1 Scattering from Cold jet, Pilot Flame and Turbulent Flame

Figure 102 plots the measured acoustic field spectra for 28 kHz driving frequency case for the following conditions:

(i) Transducer only on

(ii) Only Flame on

(iii) Cold flow jet and Transducer on

(iv) Pilot flame and Transducer on

(v) Turbulent flame and Transducer on

From Figure 102(a), we see that the turbulent flame case has approximately two orders of magnitude more power compared to the rest of the cases. Figure 102(b) shows a

close up of the spectra near the driving frequency. As expected the scattered field from the cold flow is weak compared to the pilot only on case.

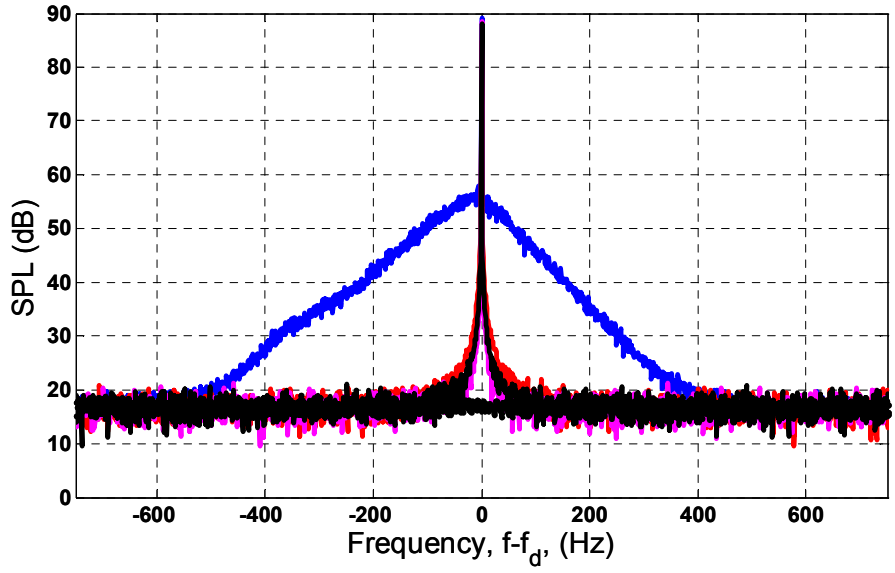

(a)

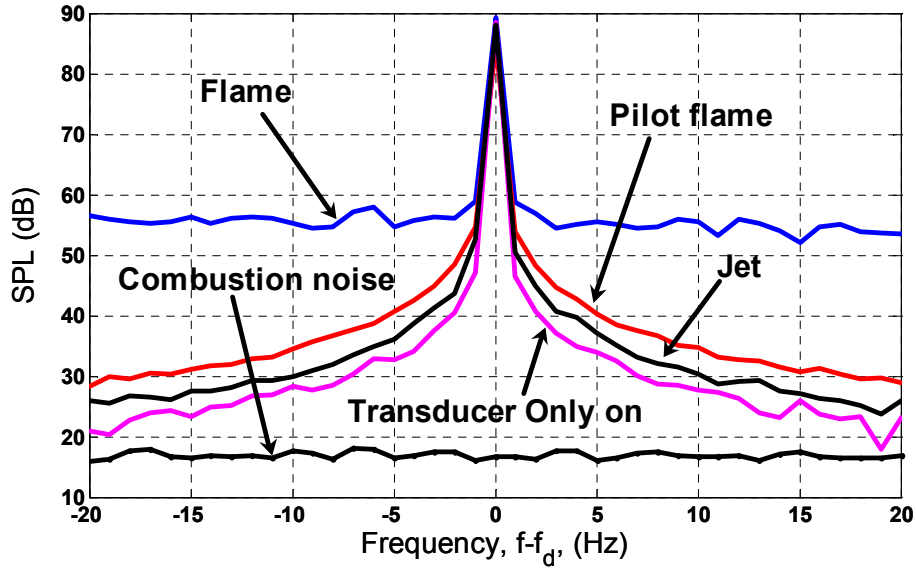

(b)

Figure 102. Scattered acoustic field for f_d = 28 kHz from (i) jet (ii) pilot flame and (iii) turbulent flame. For comparison, transducer only on case and combustion background noise are also included. Part (b) is a close up of (a). [Δ, U_m, S_L, TI, θ_i, θ_r] =[1 Hz, 4.7 m/s, 0.19 m/s, 5.6 %, 30^o and 10^o].

E.2 Scattering Measurements from the Products Side of the Flame

Scattered field spectra for two conditions are discussed in this section:

Case 1: Source and the microphones on the reactants side

Case 2: Source and the microphones on the products side, see Figure 103

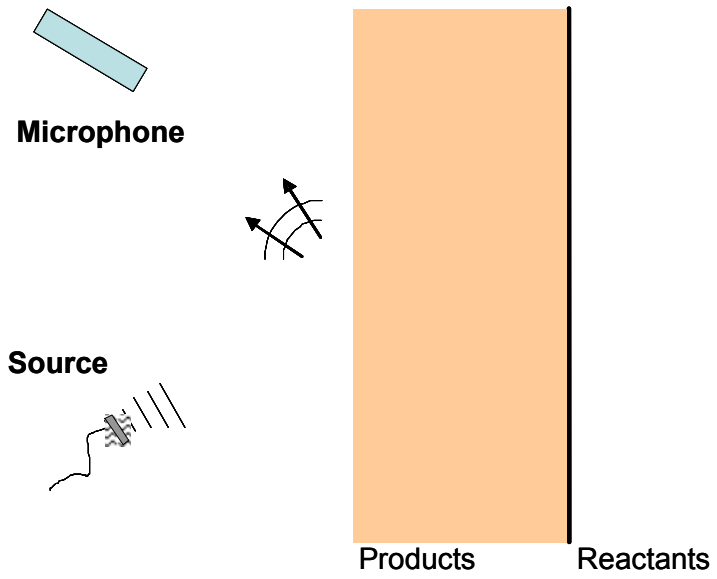

Figure 103. Illustration of the experimental configuration for case 2, where the acoustic instrumentation is located on the products side.

In the case where the source and the microphones were located on the products side, we would expect the hot product shear layer to influence the scattering process.

Figure 104 plots the spectra for f_d = 30 kHz case for the two cases listed above. For case 1, where the source and the microphone are located on the reactant side, there is a 20 Hz peak in the high frequency sideband. For case 2, we see that there are three distinct peaks: 20 Hz and 40 Hz on the high frequency sideband and 20 Hz on the low frequency side band. The contribution of these peaks tot eh total incoherent SPL for case

1 is approximately 1% and 40% for case 2. The observation that these oscillations are considerably stronger on the products side compared to the reactant side suggests that they have their origin from the products.

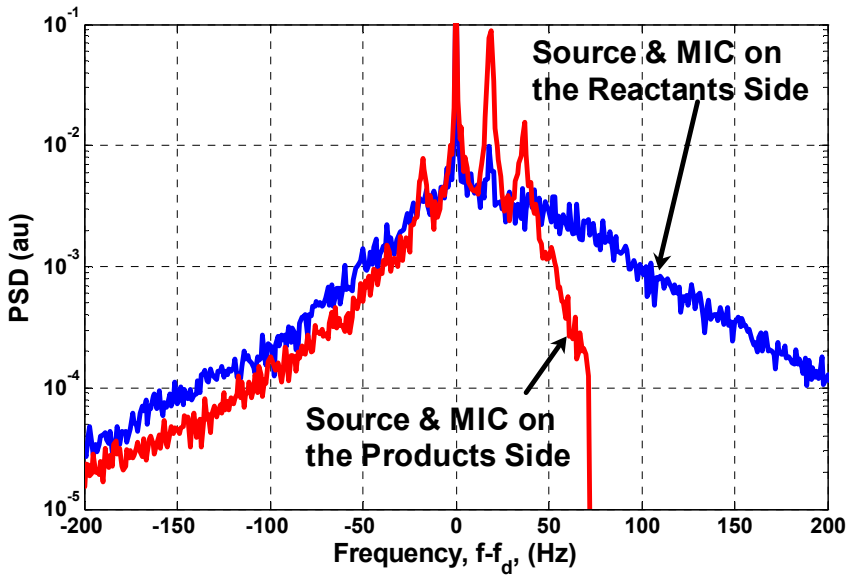

Figure 104. Scattered field spectra for f_d=30 kHz for the cases where the acoustic instrumentation is placed on the reactants side and the products side. [U_m, S_L, TI, θ_i, θ_r] =[3.7 m/s, 0.27 m/s, 5.6%, 30^o and 30^o].

Pinton *et al.*[37] have reported acoustic wave scattering measurements from a heated wake that was forced at a discrete frequency. They have reported that the scattered spectrum had discrete peaks, shifted from the incoming frequency by the multiple of the forcing frequency.

Appendix F

Additional Flame Front Statistics

In this appendix, the statistics for the combination of two mean velocities and two flame speeds, as listed in Table 2, are presented. These statistics were evaluated in the vertical plane and correspond to the single valued edges case.

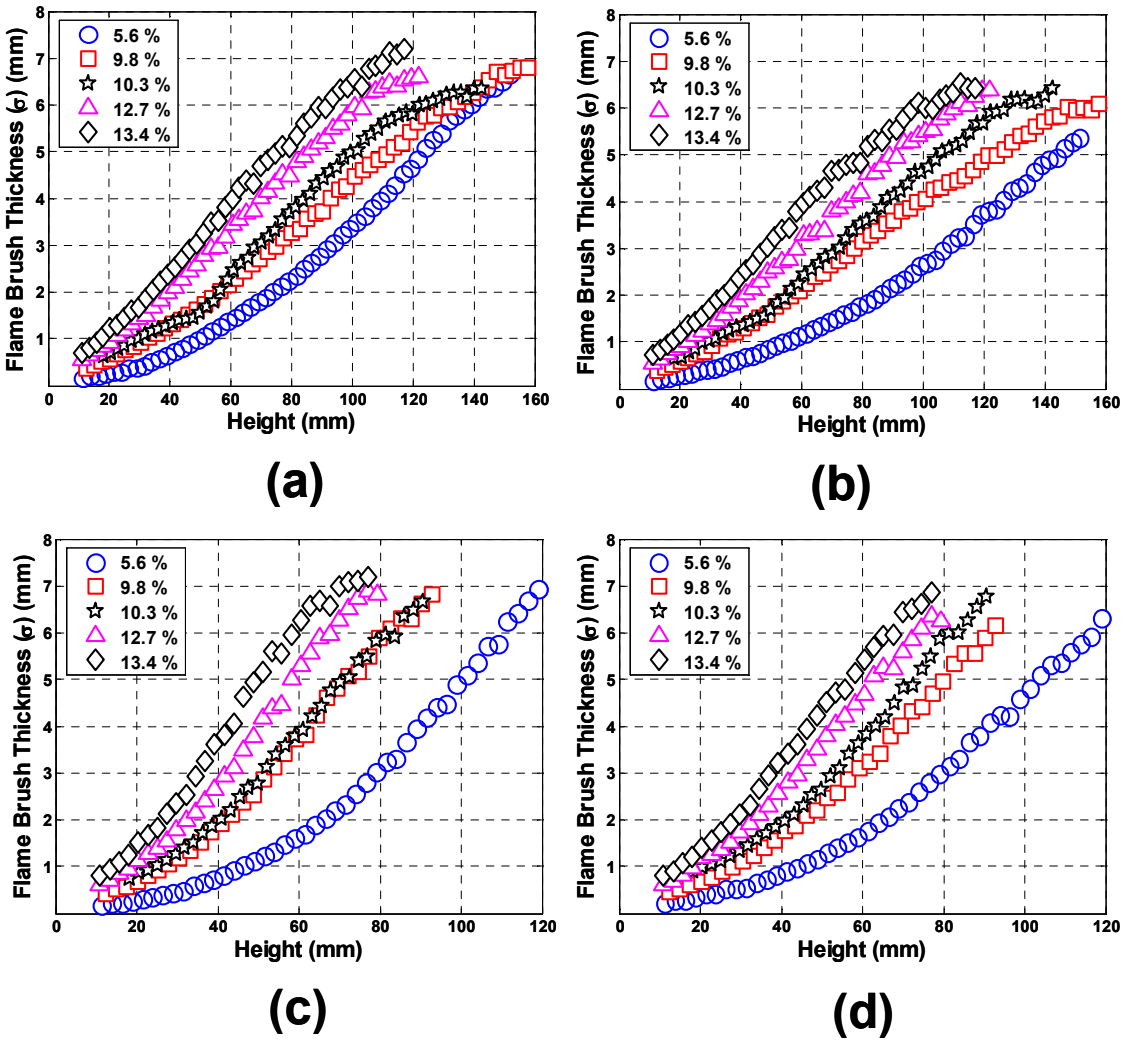

Figure 105. Flame brush thickness plotted against height for 5 turbulence intensities for (a) U_m=3.7 m/s and S_L=0.17 m/s (b) U_m=4.7 m/s and S_L=0.17 m/s (c) U_m=3.7 m/s and S_L=0.23 m/s (d) U_m=4.7 m/s and S_L=0.23 m/s.

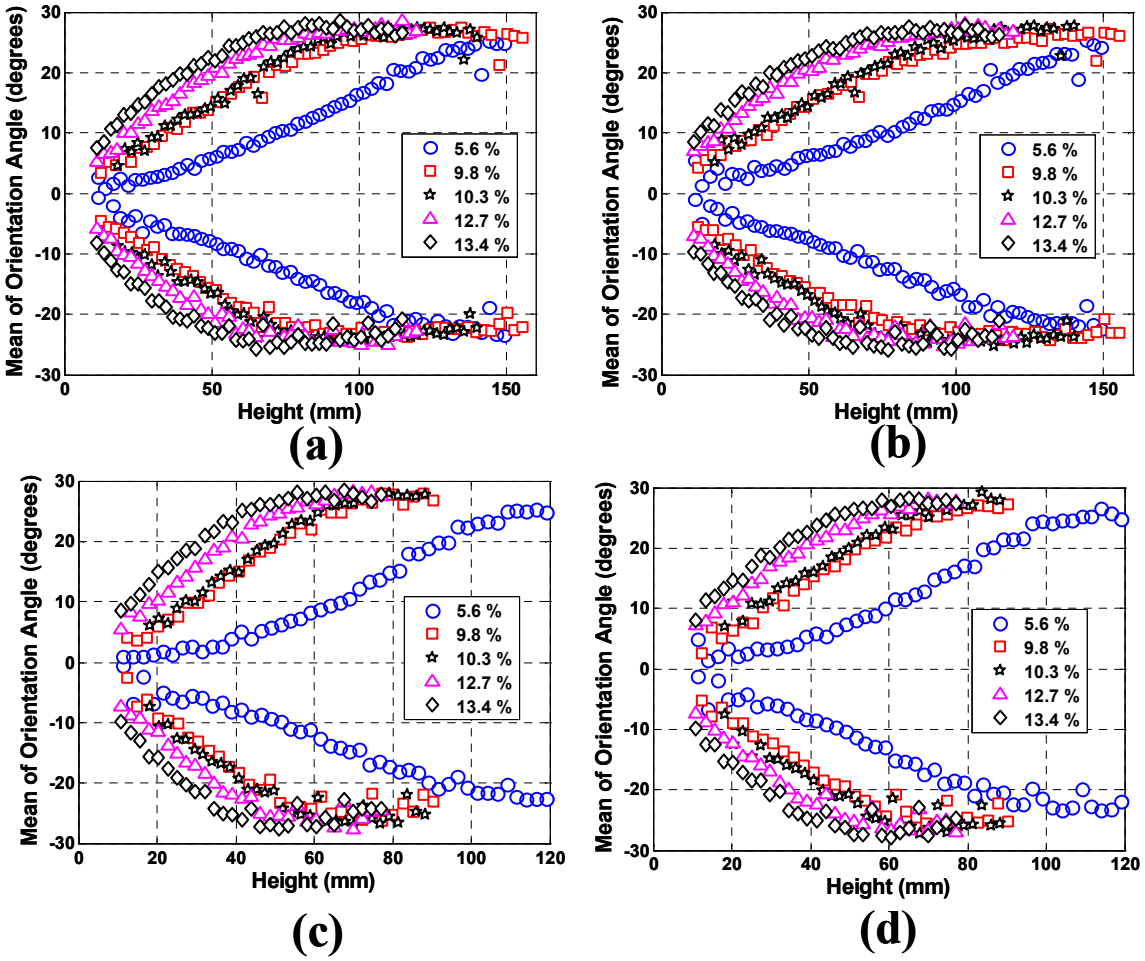

Figure 106. Mean of positive and negative flame orientation angle distribution (θ_v), plotted against height for 5 turbulence intensities for (a) U_m=3.7 m/s and S_L=0.17 m/s (b) U_m=4.7 m/s and S_L=0.17 m/s (c) U_m=3.7 m/s and S_L=0.23 m/s (d) U_m=4.7 m/s and S_L=0.23 m/s.

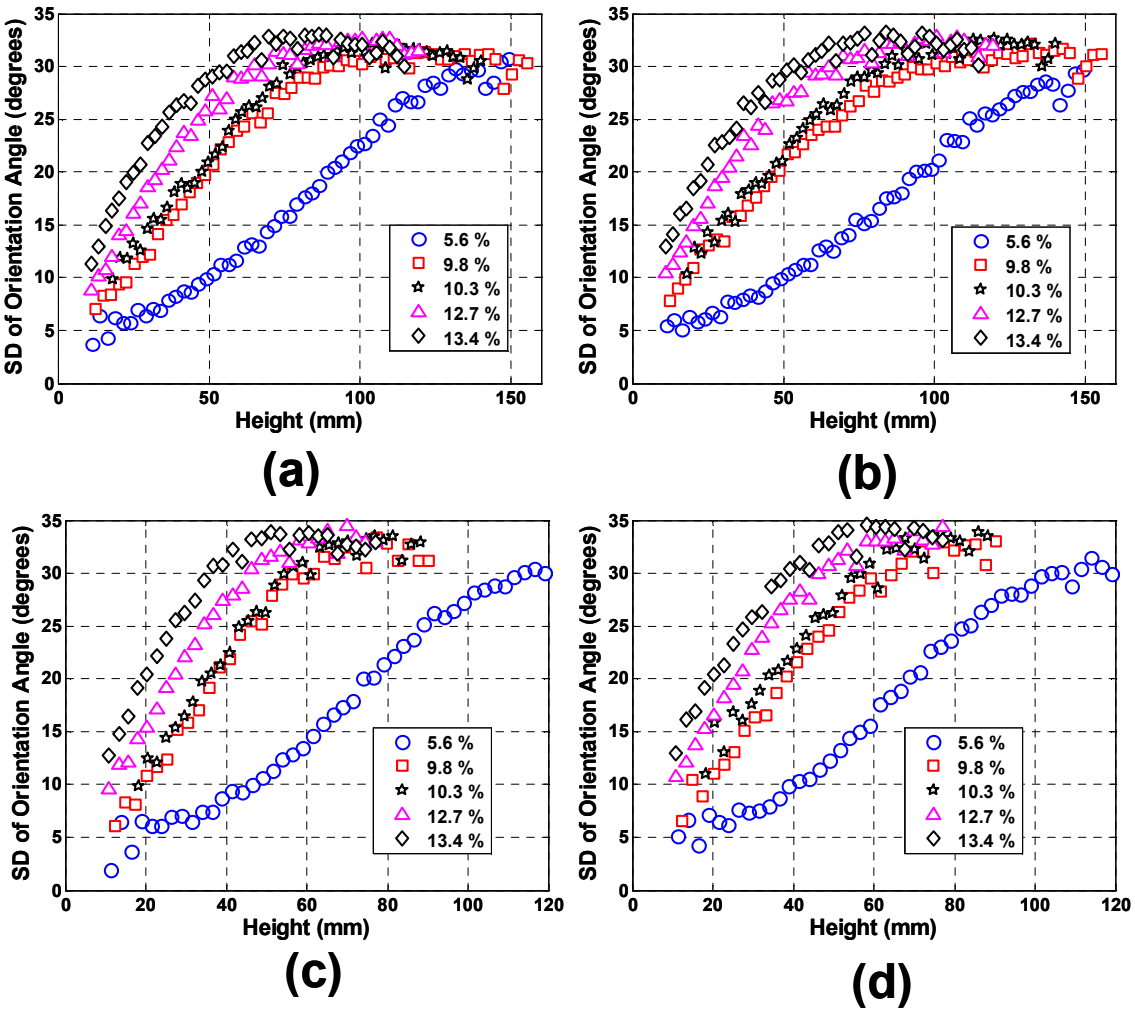

Figure 107 Standard deviation of flame orientation angle distribution (θ_v), plotted against height for 5 turbulence intensities for (a) U_m=3.7 m/s and S_L=0.17 m/s (b) U_m=4.7 m/s and S_L=0.17 m/s (c) U_m=3.7 m/s and S_L=0.23 m/s (d) U_m=4.7 m/s and S_L=0.23 m/s.

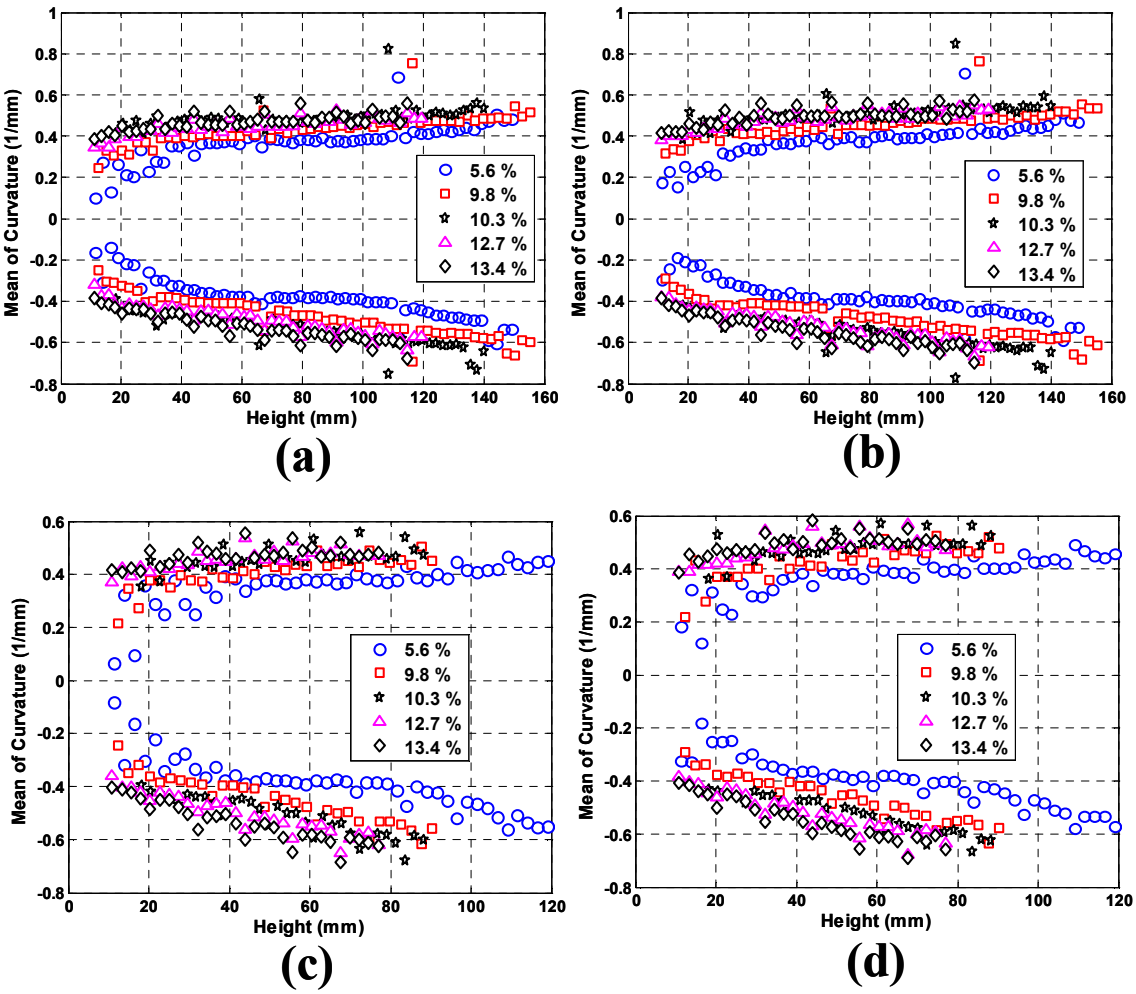

Figure 108. Means of curvature distribution, measured in the vertical plane, plotted against height for 5 turbulence intensities for (a) U_m=3.7 m/s and S_L=0.17 m/s (b) U_m=4.7 m/s and S_L=0.17 m/s (c) U_m=3.7 m/s and S_L=0.23 m/s (d) U_m=4.7 m/s and S_L=0.23 m/s.

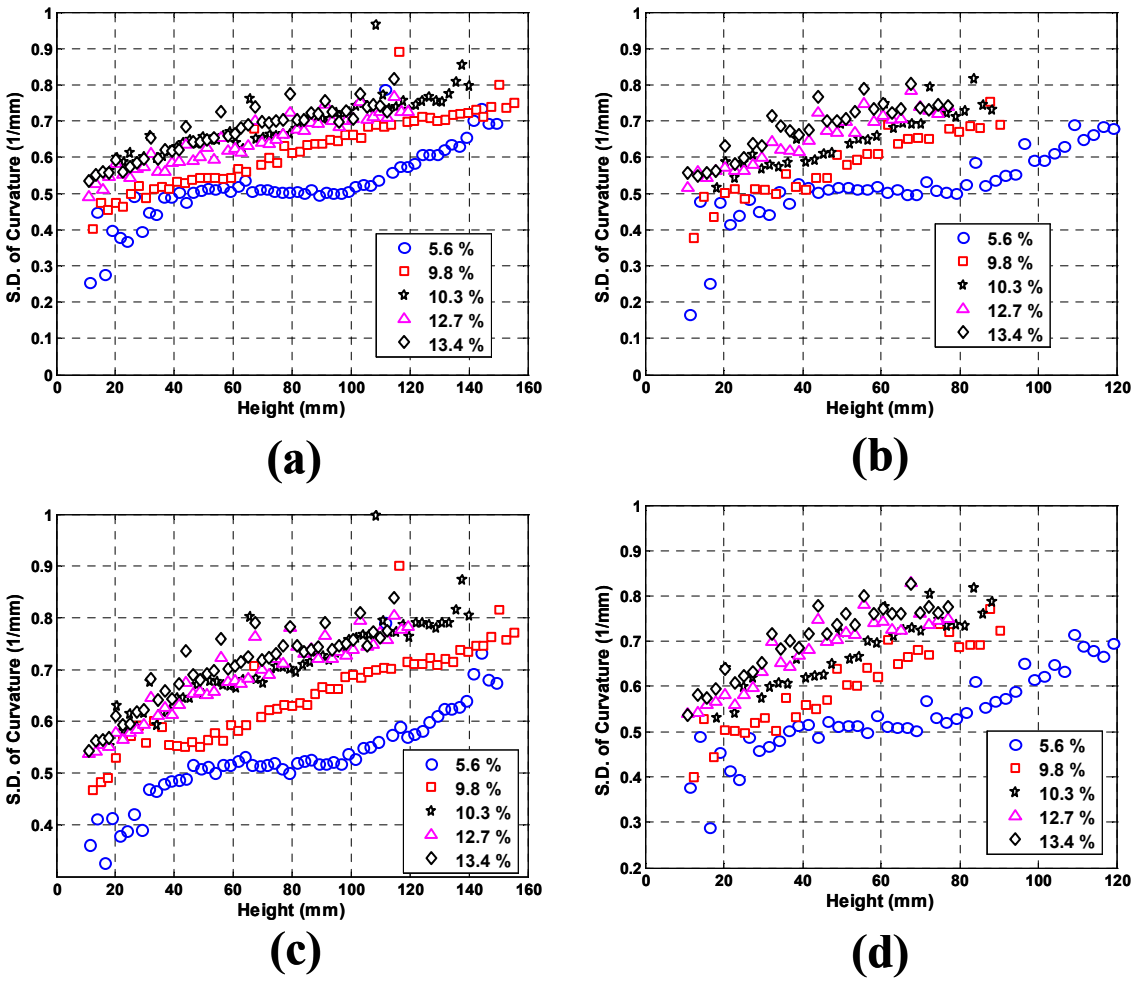

Figure 109. Standard deviation of curvature distribution, measured in the vertical plane, plotted against height for 5 turbulence intensities for (a) U_m=3.7 m/s and S_L=0.17 m/s (b) U_m=4.7 m/s and S_L=0.17 m/s (c) U_m=3.7 m/s and S_L=0.23 m/s (d) U_m=4.7 m/s and S_L=0.23 m/s.

Appendix G

Scattered Field Measurements for Extended Range of Conditions

Figure 110 plots the SPL against frequency for U_m=3.7 m/s and S_L = 0.23 m/s. We see no appreciable change in the incoherent SPL for frequencies greater than 20 kHz. However, at large measurement angles, the edge effects are expected to be dominant, see Appendix D. Figure 111 plots the bandwidth against frequency for same conditions.

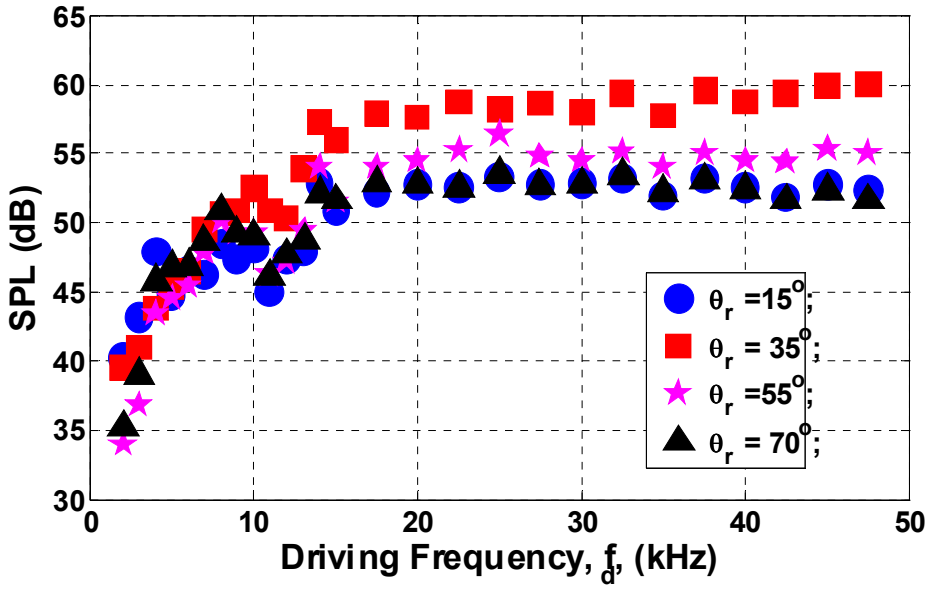

Figure 110. SPL plotted against frequency for two measurement angles. [TI, U_m, S_L, θ_i]=[5.6%, 3.6 m/s, 0.23 m/s, 60°].

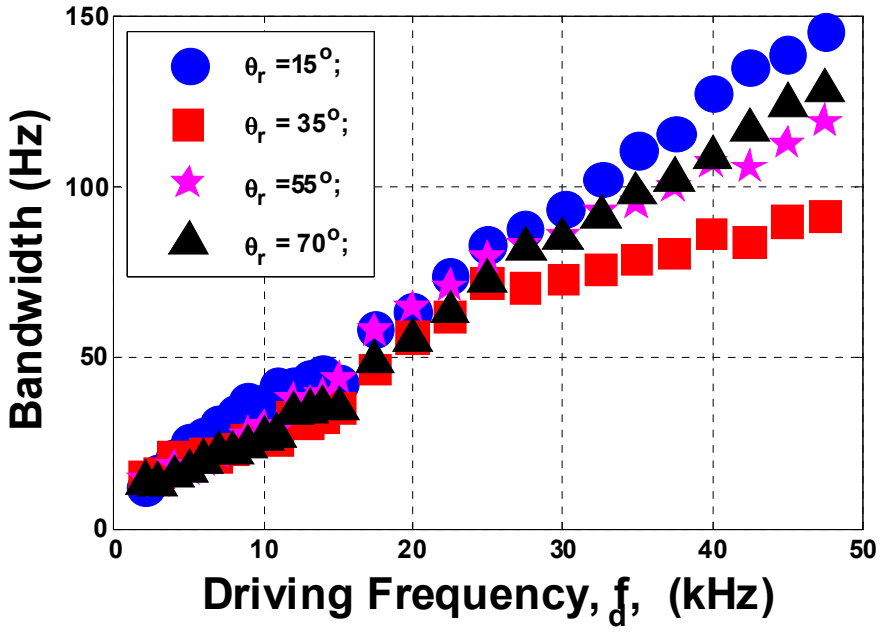

Figure 111. Bandwidth plotted against frequency for multiple measurement angles. [TI, U_m, S_L, θ_i]=[5.6%, 3.6 m/s, 0.23 m/s, 60°].

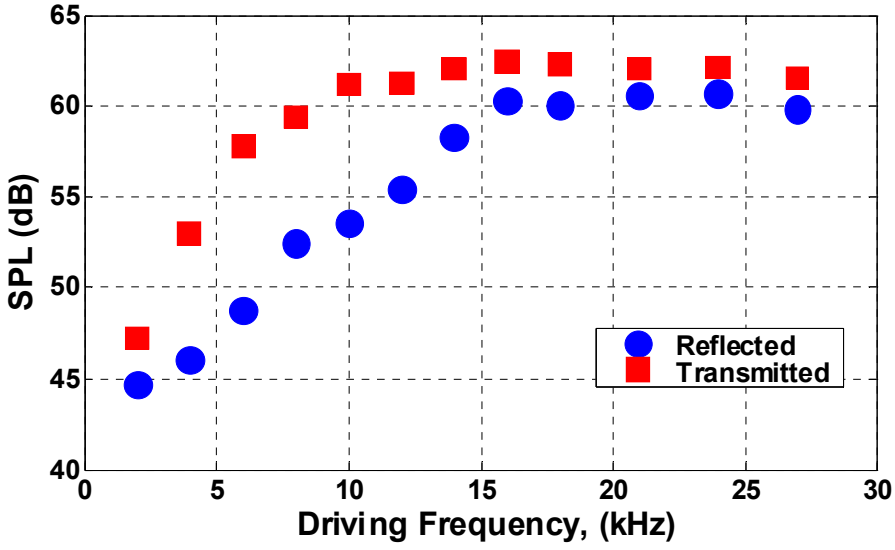

Figure 112. SPL plotted against frequency two measurement locations corresponding to reflected and transmitted fields. The microphone measuring the transmitted field is facing the source. [TI, U_m, S_L, θ_i, θ_r]=[5.6%, 3.8 m/s, 0.26 m/s, 30°, 30°].

Figure 112 plots the SPL corresponding to the reflected field and transmitted field for 30° incident angle case. The reflected field is measured at 30° angle to the mean flame front. The transmitted field is measured at 60° to the mean flame normal; i.e., the microphone is facing the source. Notice that the impedance changes across the flame front and thus SPL is not a direct measure of the sound power. Figure 113 plots the bandwidth corresponding to the reflected and transmitted field against the frequency for the same case.

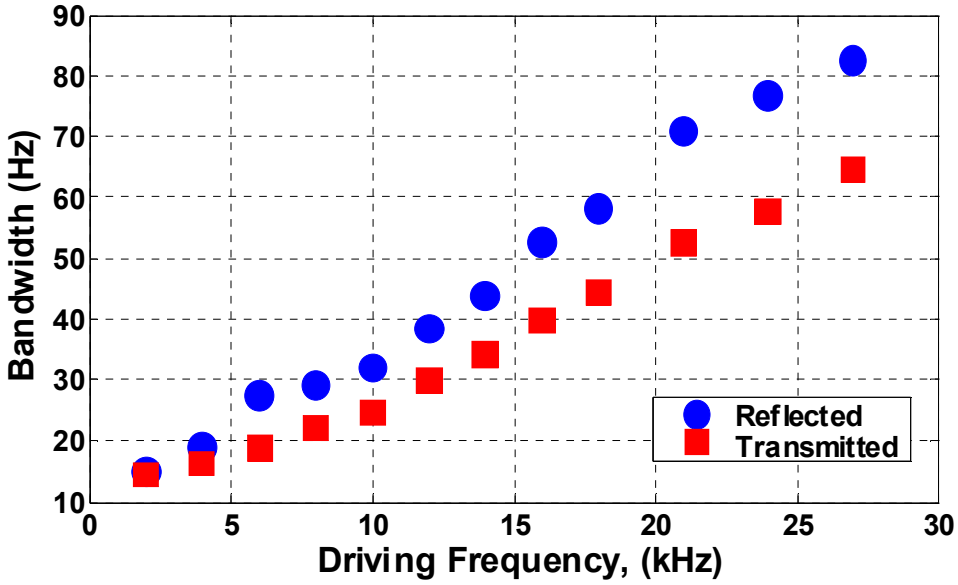

Figure 113. Bandwidth plotted against frequency for the scattered and the transmitted field. [TI, U_m, S_L, θ_i, θ_r] = [5.6%, 3.8 m/s, 0.26 m/s, 30°, 30°].

References

1 Shih, W. P., Lee, J. and Santavicca, D., Stability and Emissions Characteristics of a Lean Premixed Gas Turbine Combustor, *Proc. Comb. Inst*., Vol. 26, pp. 2771-2778, 1996.

2 Putnam, A.A., *Combustion Driven Oscillations in Industry*, American Elsevier, New York, 1971.

3 Rea, S., James, S., Goy, C. and Colechin, M.J.F., On-line Combustion Monitoring on dry low NOx Industrial Gas Turbines, *Measurement Science and Technology*, Vol. 14, pp. 1123–1130, 2003.

4 Hsiao, G.C., Pandalai, R.P., Hura, H.S. and Mongia, H.C., Combustion Dynamic Modeling for Gas Turbine Engines, *AIAA paper #98-3380,* 1998.

5 Dowling, A.P., Nonlinear Self-Excited Oscillations of a Ducted Flame, *J. Fluid Mech.*, Vol. 346, pp 271-290, 1997.

6 Peracchio, A.A. and Proscia, W.M., Nonlinear Heat Release/Acoustic Model for Thermo-Acoustic Instability in Lean Premixed Combustors, *Journal of Engineering for Gas Turbines and Power*, Vol. 121, 1999.

7 Poinsot, T., Veynante, D., Bourienne, F., Candel, S., Esposito, E. and Surget, J., Initiation and Suppression of Combustion Instabilities by Active Control, *Proc. Comb. Inst.,* Vol. 22, 1988.

8 Cohen, J. and Anderson, T., Experimental Investigation of Instabilities in a Lean, Premixed Step Combustor, *AIAA Paper #96-0819,* 1996.

9 Stow, S.R. and Dowling, A.P., Low-Order Modeling of Thermoacoustic Limit Cycles, *ASME paper #GT2004-54245*, 2004.

10 Lieuwen, T., Theory of High Frequency Acoustic Wave Scattering by Turbulent Flames, *Combustion and Flame*, Vol. 126, pp. 1489-1505, 2001.

11 Lieuwen, T., Analysis of Acoustic Wave Interactions with Turbulent Premixed Flames, *Proc. Comb. Inst.*, Vol. 29, pp. 1817-1824, 2002.

12 Chu, B.T., On the Generation of Pressure Waves at a Plane Flame Front, *Proc. Comb. Inst.* 4, pp. 603-612, 1952.

13 Markstein, G.H., *Nonsteady Flame Propagation*, Pergamon Press, Oxford, 1964.

14 McIntosh, A.C., Pressure Disturbances of Different Length Scales Interacting with Conventional Flames, *Combustion Science and Technology*, Vol. 75, pp. 287-309, 1991.

15 McIntosh, A.C. and Wilce, S.A., High Frequency Pressure Wave Interaction with Premixed Flames, *Combustion Science and Technology*, Vol. 79, pp. 141-155, 1991.

16 Peters, N. and Ludford, G.S.S., The Effect of Pressure Variations on Premixed Flames, *Combustion Science and Technology*, Vol. 76, pp. 21-44, 1991.

17 Van Harten, A., Kapila, A. and Matkowsky, B.J., Acoustic Coupling of Flames, *SIAM J. Appl. Math*., Vol. 44 (5), pp. 982-995, 1984.

18 Ledder, G. and Kapila, A.K., The Response of Premixed Flames to Pressure Perturbations, *Combustion Science and Technology*, Vol. 34, pp. 331-344, 1983.

19 Lieuwen, T., Theoretical Investigation of Unsteady Flow Interactions with a Premixed Planar Flame, *J. Fluid Mech.*, Vol. 435, pp. 289-303, 2001.

20 Clavin, P., Pelce, P. and He., L., One Dimensional Vibratory Instability of Planar Flames propagating in tubes, *J. Fluid Mech.*, Vol. 216, pp. 299-322, 1990.

21 Poinsot., T. and Candel., S., M., A Nonlinear Model for Ducted Flame Combustion Instabilities, *Combustion Science and Technology*, Vol. 61, pp.121-153, 1988.

22 Searby, G. and Rochwerger, D., A Parametric Acoustic Instability in Premixed Flames, *J. Fluid Mech.*, Vol. 231, pp. 529-543, 1991.

23 Vaezi, V. and Aldredge, R., Laminar Flame Instabilities in a Taylor-Couette Combustor, *Combustion and Flame*, Vol. 121, pp. 356-366, 2000.

24 Searby, G., Acoustic Instability in Premixed Flames, *Combustion Science and Technology*, Vol. 81, pp. 221-231, 1992.

25 Lieuwen., T., Coherent Acoustic Wave Scattering by Turbulent Flames, 2nd Joint Meeting of the U.S. Sections of the Combustion Institute, Paper #171, Oakland, CA, 2001.

26 Lieuwen, T. and J.H. Cho, Coherent acoustic wave amplification/damping by wrinkled flames, *J. Sound and Vibration*., Vol. 279, pp. 669 – 686, 2004.

27 Lieuwen., T. and Wu., L., Coherent Acoustic Wave Amplification/Damping by Wrinkled Flames, AIAA # 2003-114, 2003

28 Kinsler., L., E. and Frey., A., R., *Fundamentals of Acoustics*, Wiley Eastern Limited , 1962.

29 Chew., T., C., Bray., K., N., C. and Britter., R., E., Spatially Resolved Flamelet Statistics for Reaction Rate Modeling, *Combustion and Flame*, Vol. 80, 65-82, 1990.

30 Lee., T., W., North., G., L. and Santavicca., D., A., Curvature and Orientation Statistics of Turbulent Premixed Flame Fronts, *Combustion Science and Technology*, Vol. 84, pp121-132, 1992.

31 Lee., T., W., North., G., L. and Santavicca., D., A., Surface Properties of Turbulent Premixed Propane Flames at Various Lewis Numbers, *Combustion and Flame*, Vol. 93, 445-456, 1993.

32 Laverdant, A. and Thevenin, D., Interaction of a Gaussian Acoustic Wave with a Turbulent Premixed Flame, *Combustion and Flame*, Vol. 134, pp 11-19, 2003.

33 Laverdant,A., Gouarin, L. and Thevenin, D., Interaction of a Gaussian Acoustic Wave with a Turbulent Non-Premixed Flame, *Combustion Theory and Modeling*, Vol. 11 (4), pp 585-602, 2007.

34 Lieuwen, T., Rajaram, R., Neumeier, Y. and Nair, S., Measurements of Incoherent Acoustic Wave Scattering from Turbulent Premixed Flames, *Proc. Comb. Inst.*, Vol. 29, pp 1809-1815, 2002.

35 Lund., F. and Rojas., C., Ultrasound as a Probe of Turbulence, *Physica D 37*, pp508-514, 1989.

36 Contreras., H. and Lund., F., Ultrasound as a Probe of Turbulence II. Temperature Inhomogeneities., *Physics Letters A*, 149(2), pp127-130, 1990.

37 Pinton., J., F., Laroche., C., Fauve., S. and Baudet., C., Ultrasonic Scattering by Buoyancy Driven Flows, *J. Physique II France,* Vol. 767- 773, 1993.

38 Petrossian., A. and Pinton., J., F., Sound Scattering on a Turbulent, Weakly Heated Jet, *J. Physique II France* 7, pp801- 812, 1997.

39 Elicer-Cortes., J., C., Contreras., R., Boyer., D., Pavageau., M. and Hernandez R., H., Temperature Spectra From a Turbulent Thermal Plume by Ultrasound Scattering, *Exp.Therm.Fluid Sci.* Vo. 28 pp803-813, 2004.

40 Elicer-Cortes., J., C. and Baudet., C., Ultrasound Scattering from a Turbulent Round Thermal Pure Plume, *Exp.Therm.FluidSci.,* Vol. 18, pp271-281, 1999.

41 Elicer-Cortes., J., C., Fuentes., J., Valencia., A. and Baudet., C., Experimental Study of Transition to Turbulence of a Round Plume by Ultrasound Scattering, *Exp.Therm.FluidSci.*, Vol. 20, pp137-149, 2000.

42 Elicer-Cortes., J., C., Navia., A., Boyer., D., Pavageau., M. and Hernandaz., R., H., Experimental Determination of Preferred Instability Modes in a Mechanically Excited Thermal Plume by Ultrasound Scattering, *Exp.Therm.FluidSci.*, Vol. 30, pp355-365, 2006.

43 Samaniego, J.M., Yip, B. and Poinsot., T., Low Frequency Combustion Instability Mechanisms in a Side-Dump Combustor, T., Candel, S., *Combustion and Flame*, Vol. 94, pp. 363-380, 1993.

44 Broda, J.C., Seo, S., Santoro, R.J., Shirhattikar, G. and Yang, V., An Experimental Study of Combustion Dynamics of a Premixed Swirl Injector, *Proc. Comb. Inst*., Vol. 27, 1998.

45 Videto., B., D. and Santavicca., D., A., *Combustion Science and Technology*, Vol. 76, pp159-164, 1991.

46 Blackstock., D., T., *Fundamentals of Physical Acoustics*, Wiley-Interscience, 2000.

47 Lee., T., W., Shankland., R. and Fenton., M., Flame front curvature statistics in axisymmetric turbulent jet flames., *Combustion Science and Technology*, Vo. 108, pp31-46, 1995.

48 Namaziam., M., Shepherd., I., G. and Talbot., L., Characterization of Density Fluctuations in Turbulent V-Shaped Premixed Flames, *Combustion and Flame*, Vol. 64, pp299-308, 1986.

49 Goix., P., Paranthoen., P. and Trinite., M., A Tomographic Study of Measurements in a V-Shaped H2-air Flame and a Lagrangian Interpretation of the Turbulent Falme Brush Evolution, *Combustion and Flame*, Vol. 81, pp229-241, 1990.

50 Goulding., F., C. and Miles., F., C., *Combustion and Flame*., Vol. 100, 202, 1995.

51 Pope, S.B., *Turbulent Flows*, Cambridge university press, 2000.

52 Karlovitz., B., Open Turbulent Flames, *Fourth Combustion Symposium*, Vol. 4, p60-67, 1953.

53 Hinze., J., O., *Turbulence*, NewYork:McGraw-Hill, 1975.

54 Scurlok, A.C., Grover, J.H., Propagation of Turbulent Flames, *Proc. Comb. Inst.* 4 (1953), pp. 645-658

55 Lipatnikov., A., N., Chomiak., J., Turbulent Flame Speed and Thickness: Phenomenology, Evaluation and Application in Multi-Dimensional Simulation, *Progress in Energy and Combustion Science*, Vol 28, pp1-74, 2002.

56 Haq., M., Z., Sheppard., C., G., W., Wolley., R., Greenhalgh., D., A. and Lockett., R., D., Wrinkling and Curvature of Laminar and Turbulent Premixed Flames, *Combustion and Flame*, Vol. 131, pp1-15, 2002.

57 Bingham., D., C., Gouldin., F., C. and Knaus., D., A., Cross-Plane Laser Tomography: Direct Measurement of the Flamelet Surface Normal, *27th Combustion Symposium*, pp77-84, 1998.

58 Andrews, G. E. and Bradley, D., "Burning Velocity Of Methane-Air Mixtures," *Combustion and Flame,* Vol. 19, 1972, pp. 275-288.

59 Pierce, A.D., Acoustics*: An Introduction to Its Physical Principles and Applications*, The Acoustical Society of America, 1991.

60 Narra., V., Lieuwen., T., Acoustic Wave Scattering from Turbulent Premixed flames, AIAA-2003-3183.

61 Bendat, J., Piersol, A., Random data: Analysis and measurement procedures, John Wiley: New York, 1986.

62 Rajesh., R., PhD Thesis, Characteristics of Sound Radiation from Turbulent Premixed Flames, Georgia Institute of Technology, 2007.

63 Beckmann., P. and Spizzichino., A., *Scattering of electromagnetic waves from rough surfaces*, Oxford:Pergamon, 1963.

64 Ogilvy., J., A., *Theory of wave scattering from random rough surfaces*, IOP Pulishing Limited, 1991.

65 Acoustics – Determination of Sound Power Levels of Noise Sources – Precision Methods for Anechoic and semi-anechoic Rooms, *International Standard ISO 3745*, 2003.